Aerosol Filtration Performance of Novel 3-Dimensional Nonwoven Composites

by

Amogh Nandakishor Karwa

A dissertation submitted to the Graduate Faculty of
Auburn University
in partial fulfillment of the
requirements for the Degree of
Doctor of Philosophy

Auburn, Alabama
May 6, 2012

Keywords: wet-laid nonwoven, depth filtration, filter efficiency, carbon nanofibers, carbon nanotubes, catalyst support

Approved by

Bruce J. Tatarchuk, Chair, Professor of Chemical Engineering
Ram B. Gupta, Professor of Chemical Engineering
Virginia A. Davis, Associate Professor of Chemical Engineering
Bart C. Prorok, Associate Professor of Chemical Engineering

Executive Summary

The studies described in this dissertation focus on the design and aerosol filtration performance of novel filter media with homogeneous 3-dimensional distribution of all its components. Air purification by removal of aerosol and molecular contaminants is very important for improving breathing air quality and protecting expensive equipment and processes. Aerosol contaminants such as dust, pollen, airborne bacteria and fumes can significantly impair the quality of air. Other contaminants such as volatile organic compounds, sulfur dioxide, nitrogen oxides and carbon monoxide which are molecular in nature have to be removed using adsorbents or catalysts. A variety of filters, with different filtration efficiencies for aerosol and molecular contaminants, are used for air purification as per the requirements of their intended application. There are two main aspects of filters: (a) filter media and (b) filter media pleating and packaging. The filter media is the most basic component of filters which does the filtration. Depending on how the filter media is packaged, the filters can be made to have different performances even when using the same filter media.

Carbon nanofibers/nanotubes are an important class of nanomaterials which have been intensively researched in the last two decades for a variety of applications such as polymer composites, microelectronics and batteries. Carbon nanofibers have not been studied for applications in aerosol filtration due to the lack of understanding in making carbon nanofiber composite filter media. The studies in this dissertation explain two novel methodologies of incorporating carbon nanofibers within the filter media, and demonstrate the enhancement in aerosol filtration performance due to nanofibers. Also, a predictive semi-empirical model was

developed for aerosol filtration performance of a molecular filter media known as microfibrous materials.

Filter media are made from fibers with diameters between 0.5 μm and 80 μm. Two different methods were used to obtain uniform 3-dimensional distribution of carbon nanofibers within the traditional fibrous filter media. One of these methods is described in Chapter 2, where carbon nanofibers were synthesized on the fibers of filter media. Sintered metal fiber filter media were made with 4-12 μm (dia.) nickel fibers. Nickel metal acted as the catalyst for synthesis of carbon nanofibers by the decomposition of acetylene at high temperatures. These filter media with nanofibers coated on the microfibers showed enhancements in filtration performance. However, it was found that the pores of the filter media closed with the nanofiber synthesis which led to limitations in enhancement of filtration performance. Another limitation was that these filter media could not be scaled up in a cost effective manner. The knowledge of carbon nanofiber synthesis required to make these filter media was gained by synthesis studies on nickel foil as described in Chapter 3.

Process scalability of is an important factor to be considered for any applications involving nanomaterials. Chapter 4 describes a novel scalable process to incorporate pre-manufactured carbon nanofibers within filter media during their wet-lay formation. This methodology leads to uniform 3-distribution of nanofibers within the filter media. The resulting significant increase in filtration efficiency, even with small volume fractions of nanofibers, indicated that nanofibers acted as individual fibers within the filter media. The scalability of this process was shown by making more than 700 ft^2 of the novel filter media using a continuous Fourdrinier pilot papermaking machine.

A class of molecular filter media known as microfibrous materials is made of sorbent/catalyst particles immobilized within sinter-locked 3-dimensional matrices of microfibers. The sorbent/catalyst particles remove the molecular contaminants and the microfibers remove majority of the aerosol contaminants. Chapter 5 describes the formulation of semi-empirical models for estimating the aerosol filtration performance of these materials. Empirical factors were added to the existing models in literature to take into account the heterogeneity created by the relatively large particles within the matrices of microfibers. These semi-empirical models are powerful tools that can be used to design full scale filtration systems from microscopic scale after inclusions for pleating and packaging of filter media.

Acknowledgements

I would like to express my sincerest gratitude to Dr. Bruce J. Tatarchuk for all his support and guidance during this research. Learning from his tremendous knowledge and experience has been a thrilling experience. The vast width and depth of his knowledge have been the cornerstones of my technical and non-technical learning. I would also like to express my sincerest appreciation to Dr. Christopher B. Roberts for all his efforts in improving the department and making it a great place for graduate students. His genuine concern for all students of the department has resulted in a significant positive impact on the culture of the department experienced by the graduate students. The financial support from the US Army (TARDEC) for this research is gratefully acknowledged.

I would like to thank Dr. Virginia A. Davis, Dr. Ram B. Gupta and Dr. Bart C. Prorok for all their time and effort in serving on the committee and for their guidance during my research. I am thankful to Dr. Virginia A. Davis for her guidance during the beginning of my graduate studies. I am grateful to Dr. Maria L. Auad for her suggestions as the outside reader for this dissertation. I am thankful to Mr. Troy Barron for his time and effort during scale-up demonstration and for helpful discussions. I would like to thank all current and past members of the Center for Microfibrous Materials Manufacturing (CM^3); especially, the filtration group for helpful discussions and ideas. I would like to express my earnest appreciation to Mr. Ron Putt and Dr. Ryan Sothen for their encouragement and helpful ideas.

I am thankful to the following members of the Staff who have helped me to a great extent during my graduate studies: Dr. Donald Cahela, Mr. Dwight Cahela, Ms. Megan Schumacher,

Ms. Kimberly Dennis, Ms. Sue Ellen Abner, Ms. Karen Cochran and Mr. Brian Scweiker. I would like to thank the Graduate School and the Office of International Programs for the opportunity to pursue a PhD at Auburn University and for all their efforts to ensure the well-being of international students.

I am thankful to my friends in Auburn for making my stay very interesting and eventful. Special thanks go to my family and my uncle (Mr. Sunil Bajaj) for their love and support during my graduate studies.

Table of Contents

List of Tables

List of Figures

Chapter I Introduction and Background

I.1 Indoor air quality

Purification of indoor air is very important to provide healthy breathing air and to protect equipment and processes. There are two distinct types of contaminants in air: (a) particulate/aerosol and (b) molecular. Aerosol contaminants encompass any material that can be seen under a microscope such as pollen, human hair, bacteria, etc. Fig. I-1 lists the relative sizes of various materials including common aerosol contaminants. The other type of contaminants that is gaseous in nature is called molecular contaminants. These include volatile organic compounds, carbon monoxide, sulfur dioxide and nitrogen oxides.

A report from the United States Environmental Protection Agency (EPA) suggests that people spend approximately 90% of their time indoors [I.1]. Prolonged exposure to indoor air pollutants can be dangerous. Based on these concerns, guidelines have been suggested for the design of buildings for acceptable indoor air quality (IAQ). An example of such a guideline is Standard 62.2 [I.2] from the American Society of Heating, Refrigerating and Air-Conditioning Engineers (ASHRAE). In the manufacturing industry, particle free air is desired in many high technology sectors such as the semiconductor, biotechnology and pharmaceutical industries. In these industries, small quantities of aerosol contaminants have the potential to significantly reduce the efficiency of manufacturing. Consequently, those contaminants may lead to millions of dollars in losses. Other examples of businesses that are very cautious about air purification are food packaging, healthcare and automobile manufacturing industries.

Heating, ventilating and air conditioning (HVAC) systems installed within the buildings maintain the IAQ. Air purification by aerosol filtration is an important part of the HVAC designs. Three methods are generally used to minimize the molecular contaminants within buildings: (a) eliminating their source in building materials such as carpets, wood products, paints and printers/copiers, (b) using a high ratio of outside fresh air to minimize the recycle of indoor pollutants, and (c) design of HVAC systems to exhaust (and prevent recycle) the areas known as the sources of molecular pollutants such as volatile organic compounds, carbon monoxide, etc. [I.1]. However, for some buildings (such as museums) that demand the removal of even the trace levels of molecular contaminants, it is a common practice to use molecular filters with activated carbon and/or other chemically active materials. The primary focus of this dissertation was to design novel filter media and study their aerosol filtration characteristics.

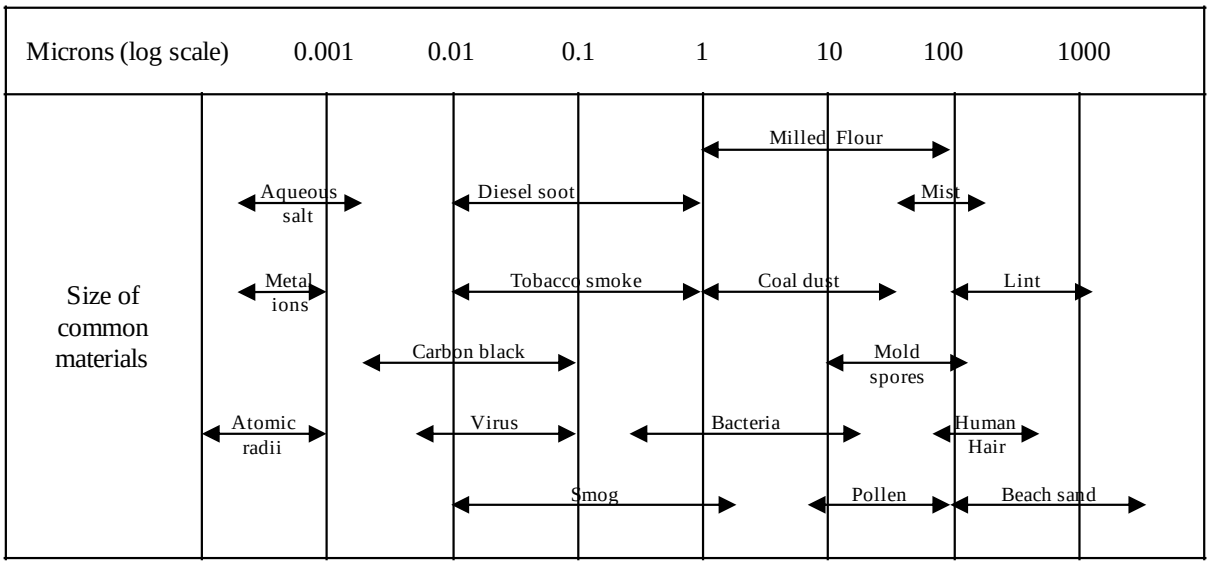

Fig. I-1. Sizes of common materials.

I.2 History of aerosol filtration

The importance of aerosol filtration can be understood through its long standing history which dates back to the Roman times. The mention of "industrial dust" as a problem is mentioned in the Natural History of Pliny the Elder (in A.D. 50), and mine dust was described as a problem in Egypt by Julius Pollux (in A.D. 150). Leonardo da Vinci (1452-1519) mentions wet cloth being used as protection from fumes during warfare. After that, there were many contributions to the field of aerosol filtration. There were significant developments in the 19th century with the designing of apparatus for aerosol filtration. In 1814, Brise Faden designed a respirator for protection against dust. In 1860, Louis Pasteur demonstrated the removal of airborne micro-organisms which led to the development of medical respirators. Smoke masks made of wires were used for the protection of firefighters in England, France and Austria. Filtering masks named "smoke caps" were invented and produced by Sir Eyre Massey Shaw and a well known physicist, Prof. John Tyndall for use in mines [I.3, 4].

The most important developments in aerosol filtration took place in the 20th century. With some qualitative understanding in early 20th century, the modeling of filters, understanding of filtration mechanisms and filter design development went through a number of stages. World War I and World War II created a desperate need for better filters for chemical warfare and aerosol filtration. During that time, aerosol filtration understanding took a giant leap forward. By the 1970s, aerosol filtration theories were well developed and simple empirical correlations were used to design the filters. These empirical correlations are still in use today. Current commercial filters are designed with the basic understanding of filtration as well as some empirical data.

I.3 Aerosol filtration

In industries handling large quantities of dust materials, cyclones are by far the most popular equipment for the removal of dust particles >5 μm (dia.). After cyclones, a series of filters are used to further purify the process air if required. Other types of equipment used for the removal of particles are wet/dry scrubbers, centrifugal separators and electrical precipitators [I.5]. Aerosol filters are primarily used in applications with a relatively low concentration of challenge aerosol. The five main types of aerosol filters (based on their structure) are:

a) Fibrous filters: These filters use woven or non-woven fabrics as filter elements. The woven fabrics are made by weaving or felting textile fibers. Non-woven fabrics do not use weaving or felting. Due to their high voidage, these filters have very high air permeability which implies less loss of energy in the form of pressure drop across filters. These filters are most popular because of their low-cost and ease of manufacturing on large scale. Non-woven fabric filters are commonly used as panel filters in residential and commercial buildings.
b) Screen filters: These filters use a polymer or metal screen for filtration. These filters are typically used for low-efficiency filtration and cake filtration.
c) Granular filters: These filters consist of packed beds of large particles. These have higher pressure drops when compared to the fibrous filters because of their low voidage. One of the popular applications of granular filters is in high temperature filtration (eg. at 850 °C) for chemical processes [I.5]. These filters are used only for applications where other types of filters are inadequate.
d) Sintered metal filters: These filters are made by sintering metal spheres together. They are very robust and can withstand a variety of process conditions. These filters are periodically cleaned and reused because of their high initial cost.

e) Membrane/Pore filters: These filters are usually only a few microns thick and are made from perforated materials such as porous plastics like polyethylene or polyurethane foams. They are used when very high filtration efficiency is required and the energy cost of filtration is not very important; such as aerosol filtration in semiconductor industries [I.3].

If >95% removal efficiency is required for aerosol in the range of 0.1 to 1 μm (dia.) at low pressure drop penalty, fibrous filters are the only option [I.3]. All the filter media studied in this dissertation fall under the category of 'Fibrous filters'. Therefore, fibrous filters will be discussed in further detail taking into consideration the intent of research.

I.4 Fibrous filter design considerations

The three parameters that are optimized during designing filters are: (a) aerosol filtration efficiency, (b) pressure drop/resistance, and (c) lifetime of the filter. Depending on the quality of air required for the application, different filters with varying properties can be obtained from various manufacturers.

I.4.1 Aerosol filtration efficiency

Aerosol filtration efficiency is the most important property of filters, and it is primarily dependent on the type of filter media used within the filters. The filtration efficiency changes significantly with the aerosol particle size. All HVAC filters are rated by the ASHRAE 52.2 standard in the United States [I.6] and the EN 779 standard in Europe [I.7]. The ASHRAE 52.2 standard uses a minimum efficiency reporting value (MERV) rating to classify the filters. The MERV rating specifies the minimum filtration efficiency for three particle ranges (0.3-1 μm, 1-3 μm and 3-10 μm). Following the procedure outlined in the ASHRAE 52.2 standard, the filters can be categorized between MERV 1 and MERV 16. Table I-1 summaries the efficiency

requirements for MERV rating classification. The procedure of MERV rating involves initial filtration testing and then loading the filter with synthetic dust to simulate the minimum filtration efficiency during the lifetime of filter. For most mechanical (non-electrostatic) filters, the filtration efficiency increases with dust loading; however, the efficiency decreases with dust loading for filters relying on electrostatics. The standard is not intended to indicate the lifetime of filters.

Table I-1. Minimum Efficiency Reporting Value (MERV) rating chart for filters.

Minimum Efficiency Reporting Value (MERV)	Composite Average Particle Size Efficiency,% in Size Range, μm			Average Arrestance,%, by Standard 52.1 Method	Minimum Final Resistance	
	Range 1 0.30 - 1.0	Range 2 1.0 - 3.0	Range 3 3.0 - 10.0		Pa	in. of water
1	n/a	n/a	$E_3 < 20$	$A_{avg} < 65$	75	0.3
2	n/a	n/a	$E_3 < 20$	$65 \leq A_{avg} < 70$	75	0.3
3	n/a	n/a	$E_3 < 20$	$70 \leq A_{avg} < 75$	75	0.3
4	n/a	n/a	$20 \leq E_3 < 35$	$75 \leq$ Aavg	75	0.3
5	n/a	n/a	$35 \leq E_3 < 50$	n/a	150	0.6
6	n/a	n/a	$50 \leq E_3 < 70$	n/a	150	0.6
7	n/a	n/a	$70 \leq E_3$	n/a	150	0.6
8	n/a	n/a	$85 \leq E_3$	n/a	150	0.6
9	n/a	$E_2 < 20$	$85 \leq E_3$	n/a	250	1.0
10	n/a	$20 \leq E_2 < 35$	$85 \leq E_3$	n/a	250	1.0
11	n/a	$35 \leq E_2 < 50$	$90 \leq E_3$	n/a	250	1.0
12	n/a	$80 \leq E_2$	$90 \leq E_3$	n/a	250	1.0
13	$E_1 < 75$	$90 \leq E_2$	$90 \leq E_3$	n/a	350	1.4
14	$75 \leq E_1 < 85$	$90 \leq E_2$	$90 \leq E_3$	n/a	350	1.4
15	$85 \leq E_1 < 95$	$90 \leq E_2$	$90 \leq E_3$	n/a	350	1.4
16	$95 \leq E_1$	$95 \leq E_2$	$95 \leq E_3$	n/a	350	1.4

The MERV rating is for filters up to 95% efficiency. A different standard is followed for very high efficiency filters such as HEPA (high efficiency particulate air) filters and ULPA (ultra low penetration air) filters. The HEPA filters are generally defined as filters with ≥99.97% efficiency for 0.3 μm aerosol particles and the ULPA filters are defined as filters with ≥99.999% efficiency for 0.1-0.2 μm aerosol particles. The Institute of Environmental Science and

Technology (IEST) issues recommended procedures (RPs) for testing HEPA filters and ULPA filters. Table I-2 summarizes the IEST recommended classification for HEPA and ULPA filters [I.8]. A more popular European standard for rating HEPA and ULPA filters is shown in Table I-3 [I.9]. The European standard is based on the minimum penetration particle size (MPPS). Further discussion of MPPS is given in Section I.5.3. Typical applications of filters have been suggested in Appendix E of ASHRAE 52.2 standard [I.6] based on MERV and IEST rating, type of filter media used and typical controlled contaminants (summarized in Table I-4).

Table I-2. IEST recommended classification of HEPA and ULPA filters.

	RP type	Efficiency (%)	At size (μm)	Local Pene. (%)
HEPA	Type A	99.97	0.3	-
	Type C	99.99	0.3	0.01
	Type D	99.999	0.3	0.01
ULPA	Type F	99.999	0.1-0.2	0.005
	Type F	99.9995	0.1-0.2	0.0025
	Type F	99.9999	0.1-0.2	0.001
Super ULPA	Type G	>99.9999	MPPS	0.001

Table I-3. CEN classification for HEPA and ULPA filters. EN 1822-1:1998 standard.

Filter class	Overall Value (%)		Local value (%)	
	Efficiency	Penetration	Efficiency	Penetration
H10	85	15	-	-
H11	95	5	-	-
H12	99.5	0.5	-	-
H13	99.95	0.05	99.75	0.25
H14	99.995	0.005	99.75	0.025
U15	99.9995	0.0005	99.9975	0.0025
U16	99.99995	0.00005	99.99975	0.00025
U17	99.999995	0.000005	99.999975	0.000025

Table I-4. Summary of application guidelines suggested in ASHRAE 52.2 standard.

Std. 52.2 Minimum Efficiency Report-ing Value	Application Guidelines		
	Typical Controlled Contaminant	Typical Applications and Limitations	Typical Air Filter/Cleaner Type
>16	**≤ 0.30 µm Particle Size** Virus (unattached), Carbon dust, Sea salt, All combustion smoke, Radon progeny	Cleanrooms, Radioactive materials, Pharmaceutical manufacturing, Carcinogenic materials, Orthopedic surgery	**HEPA/ULPA Filters**
13-16	**0.30-1.0 µm Particle Size** All bacteria, Most tobacco smoke, Droplet nuclei (sneeze), Cooking oil, Most smoke, Insecticide dust, Copier toner, Most face powder, Most paint pigments	Hospital inpatient care, General surgery, Smoking lounges Superior commercial, buildings	**Bag Filters** Nonsupported (flexible) microfine fiberglass or synthetic media. 300 to 900 mm (12 to 36 in.) deep, 6 to 12 pockets. **Box Filters** Rigid style cartridge filters 150 to 300 mm (6 to 12 in.) deep may use lofted (air laid) or paper (wet laid) media.
9-12	**1.0-3.0 µm Particle Size** Legionella, Humidifier dust, Lead dust, Milled flour, Coal dust, Auto emissions, Nebulizer drops, Welding fumes	Superior residential, Better commercial buildings, Hospital laboratories	**Bag Filters** Nonsupported (flexible) microfine fiberglass or synthetic media. 300 to 900 mm (12 to 36 in.) deep, 6 to 12 pockets. **Box Filters** Rigid style cartridge filters 150 to 300 mm (6 to 12 in.) deep may use lofted (air laid) or paper (wet laid) media.
5-8	**3.0-10.0 µm Particle Size** Mold Spores, Hair spray, Fabric protector, Dusting aids, Cement dust, Pudding mix, Snuff, Powdered milk	Commercial buildings Better residential, Industrial workplaces Paint booth inlet air	**Pleated Filters** Disposable, extended surface, 25 to 125 mm (1 to 5 in.) thick with cotton-polyes-ter blend media. **Cartridge Filters** Graded density viscous coated cube or pocket filters, synthetic media **Throwaway** Disposable synthetic media panel filters
1-4	**>10.0 µm Particle Size** Pollen, Spanish moss, Dust mites, Sanding dust Spray paint dust, Textile fibers Carpet fibers	Minimum filtration, Residential, Window air conditioners	**Throwaway** Disposable fiberglass or synthetic panel filters **Washable** Aluminum mesh, latex coated animal hair, or foam rubber panel filters **Electrostatic** Self charging (passive) woven polycarbonate panel filter

I.4.2 Pressure drop

Typically, filtration efficiency is proportional to the pressure drop when comparing well designed filters. The pressure drop across filter corresponds directly to the energy consumption as it is indicative of the work done by the blower to 'push' air through the filter. This shows that there is a trade-off between the filtration efficiency and the energy consumption which must be optimized based on the application. The pressure drop across filters typically varies linearly with the face velocity of air as per Darcy's law [I.10], as shown in Fig. I-2. However, quadratic and

third order dependence of pressure drop with high face velocities may be seen due to the compression of filter media or due to filter design. The filtration efficiency and pressure drop performance of a clean filter is called the "initial" performance of the filter. The performance of filter at the end of its service life is called "final" performance of the filter. The typical acceptable initial pressure drop for HEPA filters is around 1" of water (249 Pa) and for ULPA it is around 1.1" of water (274 Pa) at 500 ft/min. The residential and commercial filters have a MERV rating of 7 or 8 and the initial pressure drop is typically around 0.11" of water (27 Pa) to 0.15" of water (37 Pa) at 500 ft/min. The studies performed in this dissertation concentrate on the initial performance of the filter.

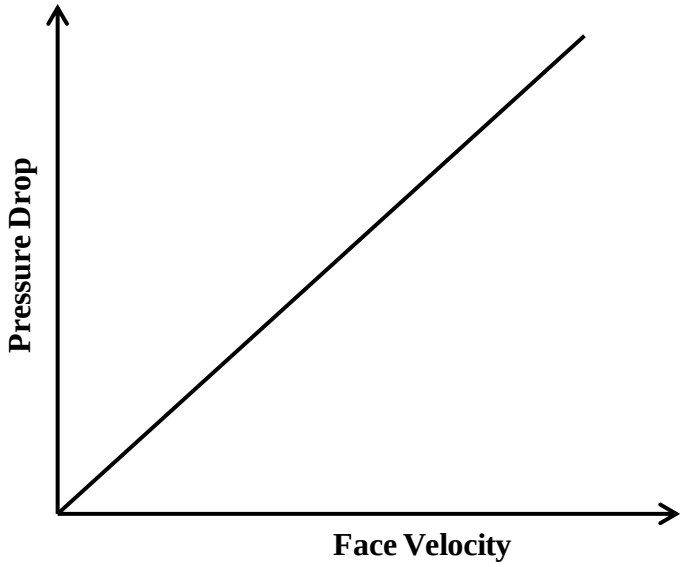

Fig. I-2. Typical profile of pressure drop across filter following Darcy's law.

I.4.3 Dirt holding capacity

The third property of filters considered during filter design is the lifetime of the filter, also known as the dirt holding capacity of the filter. During the lifespan of filter, it filters out aerosol which causes 'dirt loading' on the filter (with aerosol contaminants). This dirt loading

causes an increase in pressure drop across the filter. When the pressure drop exceeds a certain limit, the filters need to be replaced to limit the energy consumption and maintain the air flow rate required for HVAC. A typical aging curve of a filter for a constant dirt loading rate is shown in Fig. I-3. There are two distinct parts of the aging curve. The pressure drop initially increases slowly and then transitions into a phase with rapidly increasing pressure drop. The slow initial rise in pressure drop is caused by the depth loading, where the entire filter is not clogged by the dirt. The sudden increase in pressure drop is due to clogging and cake formation on the filter which results in higher pressure drop than depth loading. The cake formed on the surface of filter acts as a surface filter, also known as cake filter.

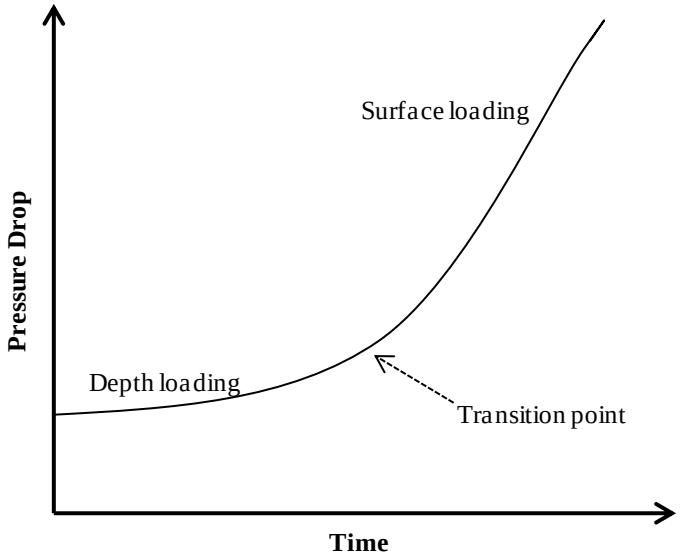

Fig. I-3. Typical filter ageing curve. Ageing caused by the deposition of aerosol particles (at constant dirt loading rate).

The dirt holding capacity of the filter is significantly impacted by the filter media pleating and the design of filter. For general HVAC applications, filters should be used until the point of transition from surface to cake filtration (or until a pre-decided pressure drop) because changing

the filter sooner or later may cause financial losses in the form of unnecessary filter changes or excess energy consumption, respectively. The current market trend is towards building Smart HVAC systems which provide a system feedback directing the replacement of the filters. However, the practice of scheduled replacement of filters is widespread and will take significant time to change given the current high cost of transition to Smart HVAC.

I.5 Fibrous filter media

The two major parts of filters are: (a) the filter media and (b) the pleating and packaging of the filter media. A typical pleated panel air filter is shown in Fig. I-4. To reduce the pressure drop across the filter, the filter media is pleated to include more media with the same cross-section of the filter. Additional area of the filter media reduces the actual face velocity through the media resulting in less pressure drop across the filter. It is important to understand that the filtration efficiency is primarily determined by the filter media and does not increase significantly with the pleating and packaging of the filter media, whereas, the media pleating and packaging significantly changes the pressure drop and lifetime characteristics of the filter.

The filter cross-section is defined by the cross-section of the duct or the HVAC design, and the depth of the filter can be customized based on the depth of pleats. Also, there is an optimum pleat count above which the pressure drop across filter starts to rise due to the tip blocking effects of the pleats [I.11]. HEPA and ULPA filters can have a filter depth (after pleating) from 6” up to 12” to keep initial pressure drop across filter at ~1” of water. Previous studies in our laboratory have extensively investigated the factors of filter media pleating and filter packaging for panel filters [I.11, 12]. The studies in this dissertation concentrate on filter media and not the packaging of media.

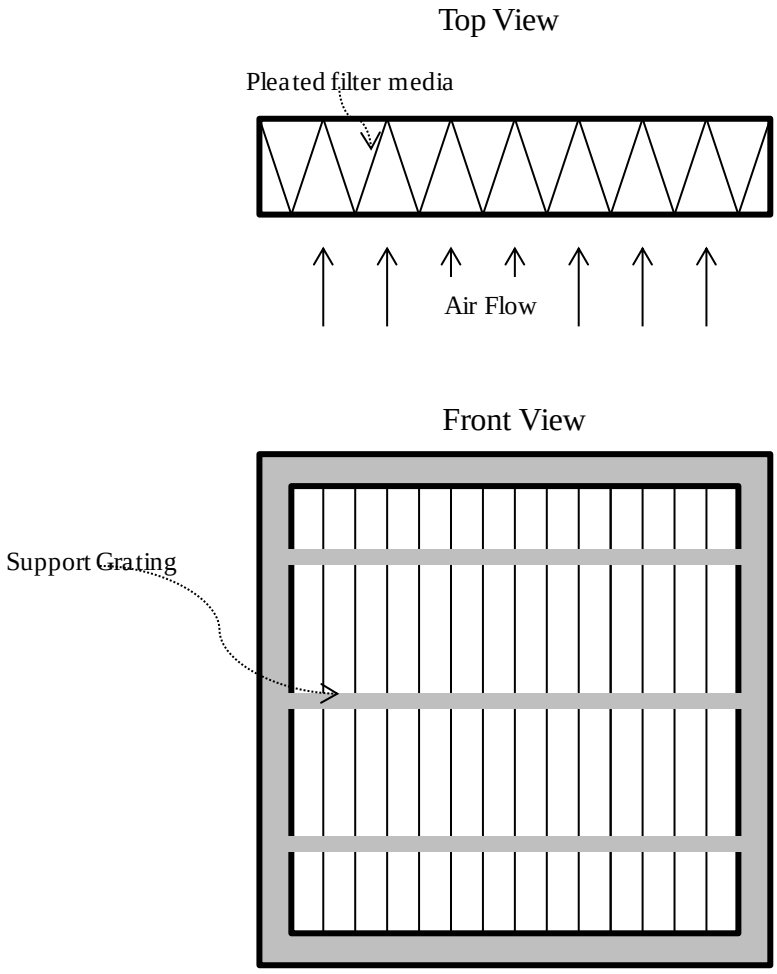

Fig. I-4. Typical panel filter with pleated filter media.

I.5.1 Important parameters of fibrous filter media

Typical filter media are made with fibers of diameter 0.5-80 μm, and fiber material can be Kraft cellulose, cotton, polymer, glass, ceramic or metal. To understand the important parameters of filter media, it is easiest to understand the variables of a very widely accepted model called the 'Single Fiber Efficiency' model. This model defines how the filtration efficiency of the media can be predicted if the filtration characteristics of a single fiber (used within the media) are known. This is a widely accepted model and further modeling developments concentrate on modeling the 'single fiber collision efficiency' (η) of the fiber

within the filter. There are a few popular semi-empirical models for single fiber collision efficiency.

The result of single fiber efficiency model gives us [I.4, 13]:

$$E = (1 - P) = (1 - \exp(-\gamma h)) \quad \text{(I.1)}$$

where, $\gamma = \frac{2\eta c}{\pi R(1-c)}$,

E: fractional aerosol filtration efficiency of the filter media

P: fractional penetration of aerosol

η: single fiber collision efficiency - defined as the efficiency of particle capture by a filter fiber(-)

h: filter media depth (m)

R: radius of filter media fibers (m)

c: solid fraction (vol.) of fibers within the filter media (related to void volume) (-)

This shows that the important parameters of filter media are solid fraction of fibers, radius of fibers, filter thickness and single fiber collision efficiency. One very important parameter which is the result of the combination of some of the above parameters is the pore size of filter media. Smaller mean pore size of filter media gives better filtration efficiency. Pore size decreases with reduction in fiber radius and/or increase in solid fraction of the fibers. HEPA and ULPA media are made of fibers with diameter of 0.6-2 μm (~1 μm average), which gives small enough mean pore size for high filtration efficiency. Although the increase in solid fraction of fibers increases the filtration efficiency, it is not the preferred route for increasing filtration efficiency because the pressure drop rises significantly faster than the filtration efficiency.

Experimental values of single fiber efficiency are typically smaller than those calculated by an accurate theory of deposition of particles on fiber. This is because the fibers are not perfectly distributed within the media and/or because of microscopic manufacturing defects within the filter media such as pin-holes. Therefore, a filter media cannot be designed only on the basis of a theoretical model, but is designed by empirical correlations which are trade secrets of the filter media manufacturers. Basic understanding of filtration mechanisms along with few semi-empirical correlations are the best guidance available for designing filter media. In order to understand aerosol filtration, various mechanisms of filtration will be discussed in the next section.

I.5.2 Filtration mechanisms for fibrous filter media

A common misunderstanding is that filter media work as a sieves – removing only the particles larger than the pore diameter of the filter media. However, there are many mechanisms of filtration and sieving is just one of the mechanisms. These mechanisms of filtration remove small as well as large diameter aerosol particles. The mechanisms of filtration by fibrous media are described below. Consider a cylindrical fiber immersed within a fluid stream (with aerosol) flowing exactly perpendicular to the length of the cylindrical fiber as shown in Fig. I-5.

The various mechanisms of filtration are diffusion, interception, inertial impaction, electrostatic deposition, gravitational settling and sieving. The diffusion mechanism is based on the Brownian motion of the particles. Brownian motion is the random movement of particles in gas or liquid. Due to Brownian motion, small particles do not strictly follow the fluid streamline and have a random path. This random path is longer than the streamline path; therefore, the probability of these small particles getting captured is very high. This mechanism of removing particles is called diffusion because the particles get “diffused” to the fibers without following

the fluid streamline, as shown in Fig. I-5. When aerosol particle size is comparable to the mean free path of gas molecule (0.06 µm in air) the particle has Brownian motion [I.4]. This diffusion mechanism is considered to be the primary mechanism of particle capture for particles less than 0.1 µm (dia.). Particles greater than 0.3 µm (dia.) do not have significant Brownian motion in air; therefore, their removal is not attributed to the diffusion mechanism.

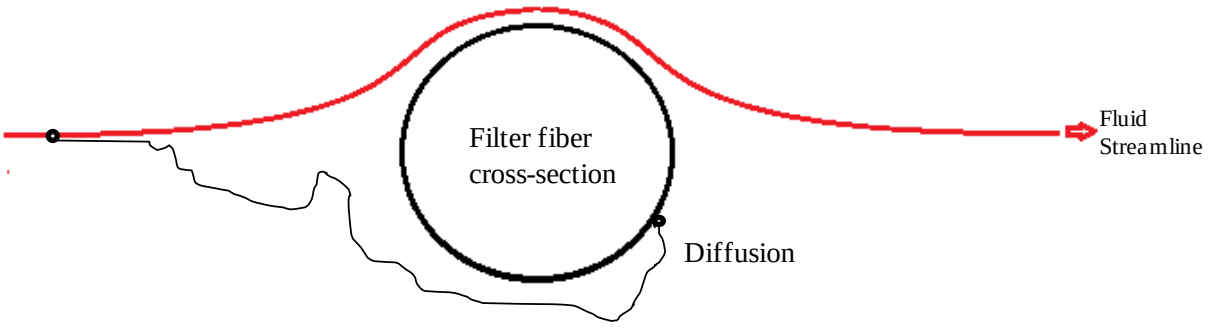

Fig. I-5. Diffusion mechanism of particle capture.

A particle following the fluid streamline gets captured by a filter fiber when it comes within one particle radius of the filter fiber, as shown in Fig. I-6. This mechanism of aerosol filtration is called interception. This mechanism is applicable only for streamlines that come close enough to the filter fiber. Interception is one of the main mechanisms of filtration for particles between 0.1 and 1 µm (dia.).

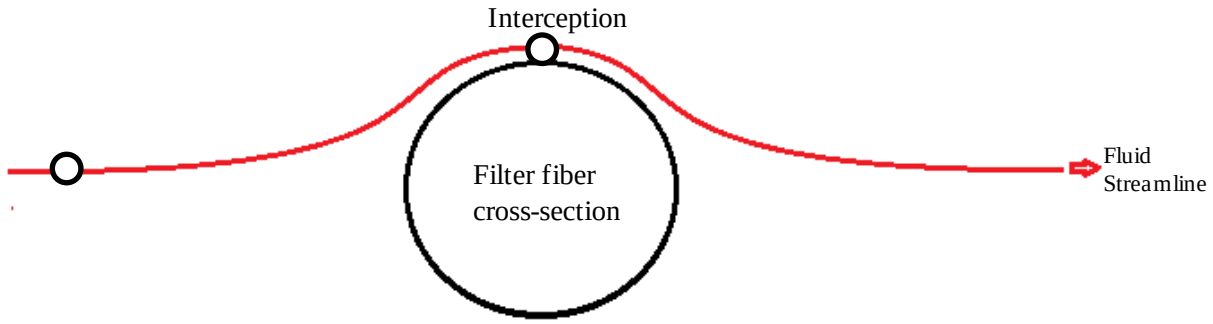

Fig. I-6. Interception mechanism of particle capture.

The inertial impaction mechanism of filtration is the capture of a particle when it has a high inertia/momentum that diverts it from the streamline and collides with the fiber, as shown in Fig. I-7. The inertial impaction mechanism is the primary mechanism of particle capture for particles greater than ~1 μm (dia.). The electrostatic deposition mechanism is based on the charge of the filter fiber and the particles, as shown in Fig. I-8. A charged fiber attracts a counter charged particle. Also, a charged fiber can attract an uncharged particle due to the image effect of charge [I.4]. A charged fiber induces an electric field which charges the particle with an opposite charge. This attracts the particle towards the fiber. This mechanism has the advantage of increasing the filtration efficiency without increasing the pressure drop. Electrostatic filters have a high initial filtration efficiency; but, they are less reliable because the efficiency of these filters decreases over a period of time due to slow loss of charge caused by neutralization and/or dirt coverage on fibers. Also, there are problems with the large scale manufacturing of filter media with consistent charge. Due to these reasons, electrostatic filters are not a very popular category of filters but they do have a market in low demanding applications.

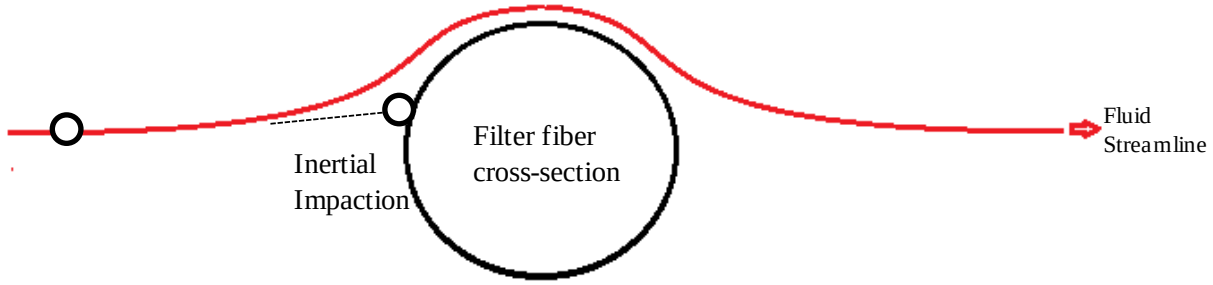

Fig. I-7. Inertial impaction mechanism of particle capture.

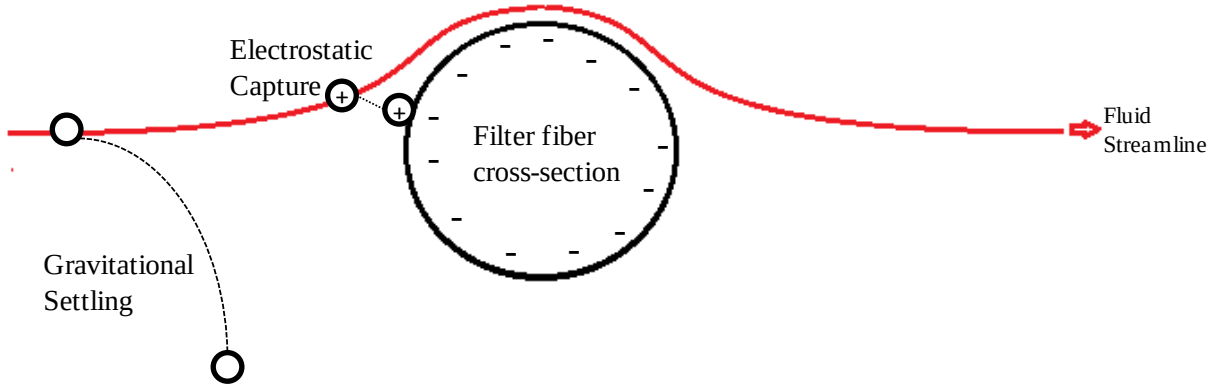

Fig. I-8. Electrostatic and gravitational settling mechanisms of particle capture.

The gravitational settling mechanism for the removal of particles is effective for particles >10 µm (dia.). The gravitational force overcomes the drag forces of the fluid which causes the particle to divert from the fluid streamline and settle down within the filter or duct, as shown in Fig. I-8. In the sieving mechanism, particles larger than the pore size of the filter do not penetrate the first layer of the filter media and are captured on the inlet side of the filter.

The three most important filtration mechanisms are diffusion, interception and inertial impaction. These three mechanisms are called ‘mechanical’ filtration mechanisms because they do not rely on any electrostatic charge for aerosol filtration. These three mechanisms have been studied in this dissertation for all filter media.

All the “filtered” particles are held to the fibers by van der Waals forces. When these forces are overcome by the drag force of air, the deposited particles can be re-entrained into the gas stream [I.4]. However, under the normal working conditions of filters, the face velocity within the filter media is typically not high enough to re-entrain the deposited particles.

I.5.3 Filtration efficiency curve

The three important mechanisms of particle capture are: diffusion, interception and inertial impaction. The dominant filtration mechanism is related to the aerosol particle size. As described above, very small particles are captured by diffusion mechanism because of their Brownian motion and big particles are captured by inertial impaction because of their high momentum. Fig. I-9 describes the various mechanisms and their impact on filtration efficiency varying with particle size. There exists a range of 0.04 to 0.4 μm (dia.) where no mechanism is strong enough to remove the particles [I.8]. In this range there is a dip in the efficiency of particle capture, as shown in Fig. I-9. The particle size which has the least filtration efficiency is called most penetrating particle size (MPPS).

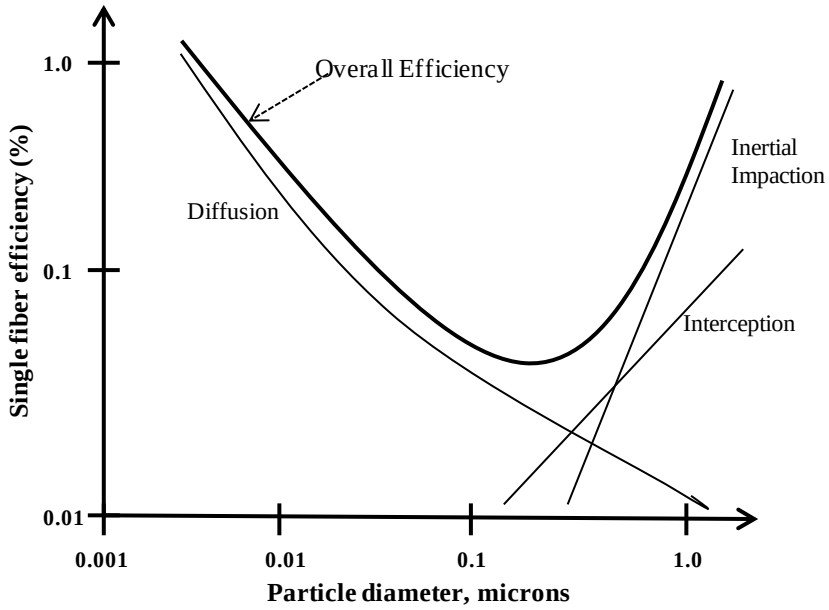

Fig. I-9. Typical filtration efficiency curve of a filter/filter media.

I.6 Fibrous filter media manufacturing

I.6.1 Fibrous media manufacturing

Fibrous filter media can be divided into two categories: a) woven and b) non-woven. Woven filter media have limitations of manufacturability, maximum filtration efficiency and high pressure drop due to relatively low voidage. Non-woven filters have captured the market because of their ease of large scale production, low cost of media and flexibility in media properties. There are different methods of manufacturing non-woven filter media which can be segregated into two major categories: 1) dry formed process - the filter media are formed without liquid and 2) wet-laid process - the filter media are formed with water as the medium.

Dry formed processes are:

1. Air-laid: The fibers are hammer milled to separate and then air conveyed to a forming wire. Very fluffy structures are formed using this process.

2. Carded: This process is used to manufacture many types of felts and carded fabrics. The process uses saw-tooth points in cards and garnets to essentially ‘comb’ the fibers into a fabric. Carding is used to manufacture low MERV rating filter media.
3. Melt-blown: This process involves the extrusion of molten polymer to a polymer flow control assembly and a metal spinneret. The spinneret has many holes through which the molten polymer is passed and quenched by air to form fibers. These fibers are then entangled to give the filter media. An air jet is used in the spinneret assembly to attenuate the fiber diameter. The fibers from melt-blown process are typically in the order of 1-4 μm (dia.). The melt-blown webs require a porous support substrate because they have limited mechanical strength.
4. Spunbonded: Spunbonded filter media are made using a process similar to the melt blown process without the use of an air jet in the spinneret assembly. Therefore, fibers of larger diameter (7-40 μm) are obtained using this process.
5. Electrospun: This process involves applying a high voltage to the polymer solution/melt and using this voltage difference to draw the fibers. These fibers can be of the order of <100 nm to 1 μm (dia.). The electrospun webs require a porous support substrate because they have very limited mechanical strength. This process is currently being developed by many manufacturers for filtration and other applications.

The wet-laid process is essentially the wet-end of the paper making process. A simplified diagram of the wet-laid process is shown in Fig. I-10. It involves mechanically dispersing fibers into aqueous slurry (stock) and then feeding it into a headbox of the filter web former. The headbox, same as a papermaking headbox, dilutes the stock and feeds it to the sheet former. Water is drained from the sheet former and the web is formed. This web is then pressed to

remove excessive water and bound by binding agents or heat. This process can handle fibers from submicron to ~20 μm (dia.). The manufacturing speed can be as high as 300 m/min for a of 5 m wide roll. Almost all the high filtration efficiency micro-glass filter media is manufactured by wet-laid process. In addition to micro-glass, different fibers such as polyester, nylon, rayon, carbon fibers or any other fibers that can be dispersed in water, can be used to make non-woven filter media using wet-laid process.

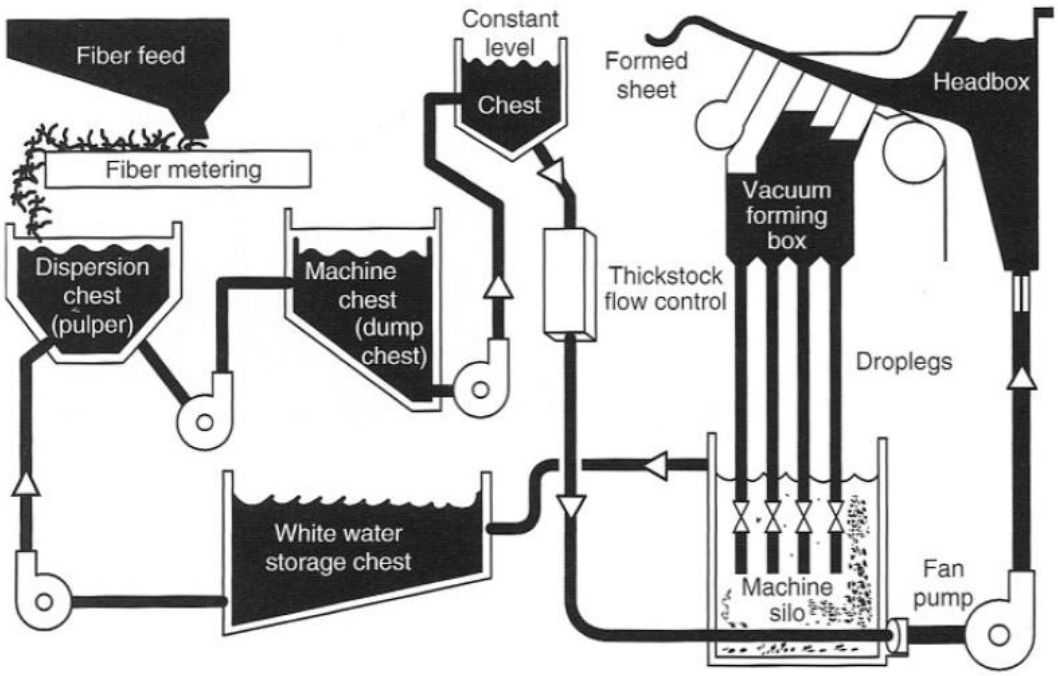

Fig. I-10. Schematic diagram of an inclined wire wet-laid process [I.8].

I.6.2 Fibrous media binding

After the web structures of the filter media are formed, some form of binding between the fibers is required to give physical strength to the filter media. For filter media made of cellulose fibers, the hydrogen bonding between the fibers is strong enough for some applications. Other forms of binding are:

1. Mechanical
    a. Needle punching – barbed needles are used to entangle and mechanically lock the fibers to give strength to the filter media.
    b. Hydroentanglement – Jets of water instead of needles are used to entangle and mechanically lock the fibers of the filter media.
    c. Stitch bonding – Knitting elements with or without sewing threads are used to interlock fibers and give strength to the filter media.
2. Chemical: Chemical binders are homogeneous or colloidal solutions of resin (polymers) in water or an organic solvent. After the application of resin solution on the filter media, the solvent is removed by heating. The resins cover the fibers within the filter media giving the desired properties to fibers. Also, these resins act as microscopic glue within the filter media and give strength to the filter media.
    a. Aqueous: Water is used as a solvent to apply the resin to the filter media. These types of filter media are typically used for organic fluid filtration such as engine oil, hydraulic oil and transmission oil. This is a preferred method of manufacturing because of no emissions of organic solvents.
    b. Solvent: Organic solvents are used to apply the resin to the filter media. These types of filter media are used for various aerosol and liquid filtration applications.

Good manufacturing practices have to be used to minimize the emissions of organic solvent during manufacturing.

3. Thermal

    a. Calendering/sintering: The fibers of the media are bonded to each other by melting the surface of the fibers at high temperatures. The high temperature for calendering is typically achieved using oil/steam heated rollers. The high temperature can also be achieved using a belt furnace.
    b. Ultrasonic bonding: This is a relatively newer method of bonding fibers using ultrasonic machines. The ultrasonic machines melt the surface of polymer fibers and bind them together.
    c. Hot melt bonding: Molten polymer is infused within the media and then cooled to bind the filter fibers together.
    d. Through air bonding: Hot air is passed through the filter media to melt the surface of polymer fibers and bind them together.

I.7 Motivation of research

There are two main aspects of air purification: (a) aerosol filtration and (b) molecular filtration. The studies in this dissertation concentrate on developing and studying novel aerosol/molecular filter media with the intention of using them as depth filters and not surface filters. The subsequent chapters describe the design of 3-dimensional depth filter media and their aerosol filtration characteristics. Wet-laid process of making non-woven filter media with thermal binding (sintering) of fibers was chosen as the preferred route of making filter media for these studies.

I.8 References

[I.1] U.S.E.P. Agency, The inside story: a guide to indoor air quality, Environmental Protection Agency, 1995.

[I.2] ASHRAE 62.2-2010, Ventilation and acceptable indoor air quality in low-rise residential buildings, American National Standard, Atlanta, GA, U.S.A., 2007.

[I.3] C.N. Davies, Air filtration, London, New York, Academic Press, 1973.

[I.4] K. Spurný, Advances in Aerosol Filtration, CRC Press, 1998.

[I.5] D.W. Green, Perry's Chemical Engineers' handbook, McGraw-Hill, 2008.

[I.6] ASHRAE 52.2, Method of testing general ventilation aircleaning devices for removal efficiency by particle size, American National Standard, Atlanta, GA, U.S.A., 1999.

[I.7] CEN EN779, Particulate air filters for general ventilation--determination of the filtration performance, European Standard, 2002.

[I.8] I.M. Hutten, Handbook of nonwoven filter media, first ed., Butterworth-Heinemann, Oxford, 2007.

[I.9] CEN EN1822-1, Most penetrating particle size, European Standard, 1998.

[I.10] P.C. Carman, Flow of gases through porous media, Butterworths Scientific Publications, 1956.

[I.11] R.A. Sothen, B.J. Tatarchuk, A semi-empirical pressure drop model: Part I--Pleated Filters, HVAC&R Res. 14 (2008) 841-860.

[I.12] R.A. Sothen, B.J. Tatarchuk, A semi-empirical pressure drop model: Part II--Multi-Element Pleated Filter Banks, HVAC&R Res. 15 (2009) 269-286.

[I.13] R.C. Brown, Air Filtration: An Integrated Approach to the Theory and Applications of Fibrous Filters, Pergamon, 1993.

Chapter II Aerosol filtration enhancement using carbon nanostructures synthesized within a sintered nickel microfibrous matrix

II.1 Abstract

Enhancement in aerosol filtration by synthesizing carbon nanostructures including nanofibers within nickel sintered metal microfibrous matrices/filter media was studied. An improvement in filtration performance observed in the quality factor ($-\ln(1-E)/\Delta P$) analysis was attributed to wall slip flow over nanofibers. The wall slip flow contributed to high filtration efficiency and a low rise in pressure drop. The effects of varying quantities of carbon nanostructures and their effects on matrices of various pore sizes were also studied. Three different diameters of nickel microfibers (4 μm, 8 μm and 12 μm) were used to prepare filter media in order to study the effects of carbon nanofiber synthesis on filter media of different pore sizes. The synthesis condition was chosen for uniform synthesis in the 3-dimensional structure of the matrix and to prevent only 2-dimensional surface deposition. The quantity of nanostructures was changed by varying the synthesis time. Two competing effects were seen as the quantity of nanostructures increased: an increase in filtration efficiency due to nanostructures and an increase in pressure drop due to the decrease in the mean pore diameter of the filter media. For 4 μm matrices, which had a small initial mean pore diameter, the benefit of an increase in filtration efficiency was outweighed by the decrease in the mean pore diameter. This study shows that carbon nanostructure synthesis leads to significant improvement in the performance of filter media with large initial pore size because the pore diameters do not reduce significantly with synthesis.

II.2 Introduction

In the last decade, there has been significant interest in the use of nanofibers for aerosol filtration. Nanofibers for use in aerosol filtration are defined here as fibers less than 500 nm in diameter. Polymer nanofibers used in filters are predominantly produced using an electro-spinning process [II.1-3]. Also, melt blown processes have the potential to produce nanofibers as they are beginning to break the 250 nm fiber production barrier [II.4, 5]. However, polymer nanofibers lack the strength required for filter manufacturing processes such as pleating [II.1]. For this reason, most polymer nanofiber media manufacturing techniques use a traditional non-woven filter media over which the polymer nanofibers are layered. The use of a traditional non-woven filter media provides the processability of a typical filter media and a nanofiber layer enhances aerosol filtration [II.1]. The nanofibers increase aerosol filtration efficiency without substantially increasing pressure drop due to wall slip flow over nanofibers. However, there is one disadvantage of nanofibers layered on filter media: the nanofiber-layered media has low dirt holding capacity [II.6] because it acts as a surface filter compared to traditional filter media, which are depth filters. For this reason, the life of polymer nanofiber filters is short because they clog easily. These types of filters can be used in applications such as filter masks for personnel protection which require excellent initial filtration without substantial initial pressure drop and have low requirements for dirt holding capacity.

The aim of this work was to understand how aerosol filtration can be made more efficient due to wall slip over nanofibers when the nanofibers are used in depth filtration rather than surface filtration. The approach taken for this research was to synthesize carbon nanofibers (CNF) throughout the depth of the sintered metal microfibrous (SMM) matrix. Fig. II-1 shows the expected difference between the filter structure of the electrospun/meltblown polymer

nanofiber layer deposition process (Fig. II-1 (A)) and the carbon nanofiber synthesis process (Fig. II-1 (B)). The nanofiber synthesis filter will inherently have a high dirt holding capacity because nanofibers are distributed uniformly throughout the depth of the filter. There are very few reports of the use of CNF and carbon nanotubes for aerosol filtration [II.7-9]. However, a detailed study of the effects of uniform carbon nanofiber synthesis on depth filtration for different pore size filter media has not been reported and was the focus of this work.

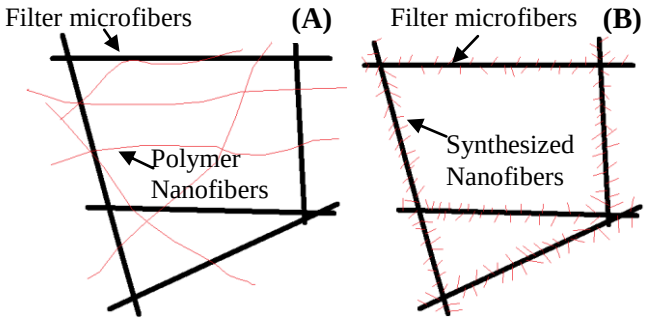

Fig. II-1. Schematics of (A) electrospun/meltblown polymer nanofibers layered on filter media, and (B) carbon nanofibers synthesized on fibers of filter media.

II.3 Experimental

II.3.1 Materials

Ribbon-shaped nickel microfibers (alloy Ni-200) of metal purity >99% with nominal diameters of 4, 8 and 12 µm, and lengths of 3-6 mm were obtained from Intramicron Inc. (Auburn, AL). High purity nitrogen (99.999%), hydrogen (99.999%) and acetylene (99.6%) supplied from Airgas Inc., were used in experiments without further treatment.

II.3.2 Methods

II.3.2.1 Sintered metal microfibrous (SMM) matrix/filter media preparation

Nickel microfibers were dispersed in water with high viscosity. The viscosity of water was increased by the addition of 0.75% (w/w) hydroxyethyl cellulose (HEC), which helped to disperse nickel microfibers without excessive reduction in their aspect ratio. The nickel microfiber dispersion was used to create preforms of SMM filter media using a 16 cm diameter TAPPI hand-sheet former. These preforms were sintered at 950 ˚C using 10-15% hydrogen in nitrogen for 40 min to form the SMM filter media. The samples were punched out from the SMM filter media using a steel punch. Each circular sample of 54 mm diameter weighed 1.74 g (±0.05 g). The SMM filter media samples were compressed by a hydraulic press with the sample placed between two 3.2 mm thick tight-tolerance steel plates with 0.30 mm thick washers used as spacers around the sample for specifying the final thickness of the sample. Due to the malleable nature of the metal fibers, SMM matrices can be significantly compressed without breaking them. After the compression under load of 10,000 lb on the top 15.2 cm × 15.2 cm steel plate, the SMM filter media samples' average thickness was ~0.39 mm as compared to ~4 mm before compression. SMM matrices were compressed in this manner to reduce the voidage of matrices in order to measure the aerosol filtration efficiencies of 12 μm SMM matrix with good accuracy. The difference in the thickness of spacer and filter media was due to the spring back of the SMM filter media after removal of the compression load.

II.3.2.2 Synthesis of carbon nanostructures (CNS)

The carbon nanofibers and the byproduct of amorphous carbon are together termed as carbon nanostructures (CNS). CNS were synthesized using a thermal catalytic chemical vapor deposition (thermal CCVD) process at atmospheric pressure. The laboratory setup of the thermal

CCVD is shown in Fig. II-2 (A). The thermal CCVD process involves a quartz reactor containing catalyst inserted in a furnace. The compressed nickel SMM matrices were used as catalysts for CNS synthesis. The flow rates of hydrogen, nitrogen and acetylene gases in the reactor were controlled by rotameters. The direction of gas flow during CNS synthesis was perpendicular to the face of the filter media.

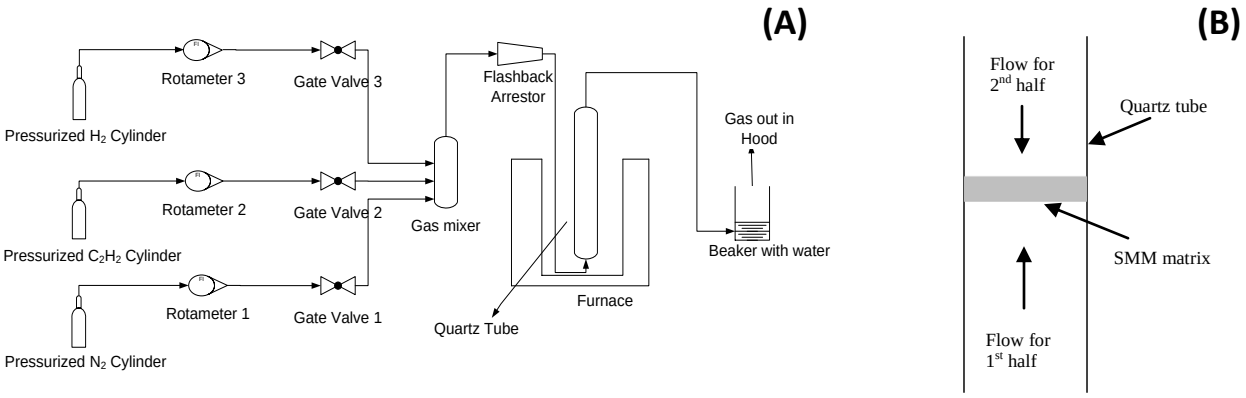

Fig. II-2. CNS synthesis: (A) experimental setup and (B) schematic of sample position in quartz tube and flow of gases through the filter media for the 1st half and 2nd half of the total synthesis time.

The filter media, inserted in the quartz tube with no leaks from the media edges, acted as catalyst bed with gas flowing through the media. For uniform synthesis of CNS, the synthesis gas mixture was passed through both faces of the matrix for an equal time, as shown in the Fig. II-2 (B). The sample was supported by quartz wool on both sides (not shown in figure). Two different total synthesis times of 5.5 min and 11 min were used to change the quantity of CNS synthesized on SMM matrices. The synthesis conditions were optimized to a temperature of 450 ˚C to reduce the reaction kinetics of the acetylene decomposition for CNS synthesis to produce a uniform 3-dimensional growth of CNS. A gas mixture with 20 cc/min acetylene, 100 cc/min hydrogen and 950 cc/min nitrogen (STP) was used during CNS synthesis. Prior to synthesis, the

SMM matrix was inserted in the furnace at 450 ˚C with a flow of 10% hydrogen in nitrogen for 20 min to allow the sample to equilibrate at 450 ˚C. After synthesis at 450 ˚C, the reactor was removed from the furnace and cooled to ambient temperature with nitrogen flow. The increase in weight of samples after 5.5 min and 11 min synthesis was 0.105 g (±5%) and 0.210 g (±5%), respectively. To make the text more readable, abbreviations of samples with CNS synthesis time of 0 min (CNS-0), 5.5 min (CNS-5.5) and 11 min (CNS-11) have been used in text.

II.3.3 Characterization

II.3.3.1 Physical structure characterization

Physical characteristics of the filter media were determined using scanning electron microscopy (SEM), capillary porometry and Raman spectroscopy. The sample thickness used for determining voidage was measured using a digital thickness gauge under a pressure of 1 kPa. The effect of CNS synthesis on the surface of filter fibers was observed using a JOEL 7000-F SEM. A capillary porometer (model# CFP-1200-AEXM) from Porous Materials Inc., was used to measure the bubble point pore diameter and mean pore diameter of filter media samples. Galwick^{TM} was used as the wetting liquid for porometry measurements. It has a surface tension of 15.9 mJ/m^2 at 20 ˚C. A Renishaw InVia Raman spectrometer was used to characterize the ratio of sp^3 to sp^2 carbon content of synthesized CNS.

II.3.3.2 Filtration efficiency and pressure drop testing

The SMM filter media were tested for aerosol filtration efficiency and pressure drop in the setup shown in Fig. II-3. The setup used compressed house air for the testing. House air was dehumidified using silica gel desiccators and then, HEPA filtered to remove any background aerosol contaminants. One portion of dry air went to the nebulizer, and the other section was

used as the drying air. The air flow was controlled by mass flow controllers (MFC). Air at a flow rate of ~1.3 L/min was passed through the nebulizer, and the drying air flow rate was 30 L/min. The nebulizer chosen for the continuous production of low concentration poly-dispersed aerosol was a DeVilbiss nebulizer (product # 4650D-621) after testing six different types of nebulizers for consistency of performance. A potassium chloride solution (10% (w/w)) was used in the nebulizer to generate aerosol particles. The drying air was passed through a SIMCO neutralizer (product # AN-6), which ionized the air to neutralize the static charge created on particles due to aerosolizing. After mixing with the drying air, the concentration of particles was between 160,000 and 300,000 particles per 100 cc of air. Most of the aerosol stream went to the exhaust and approximately 10% of the air was forced through the sample holder using a Venturi vacuum pump.

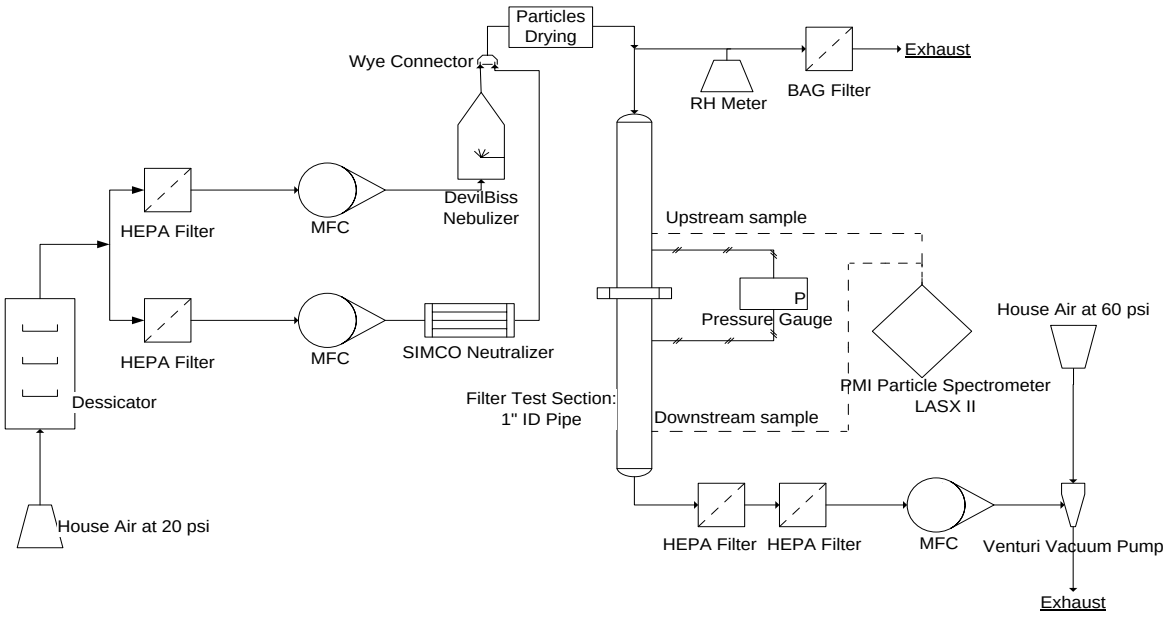

Fig. II-3. Experimental setup for filtration efficiency and pressure drop testing.

The sample holder was made from stainless steel 2.54 cm (ID) pipes and flanges because stainless steel tubes/pipes are known to have low transport losses of particles. A 5.4 cm diameter

sample was used to provide a seal around the edges of the 2.54 cm diameter area. The L/D ratio of pipe was greater than 15 upstream and downstream to make sure that the aerosol was uniformly distributed before sampling. The SMM matrix sample was held between the two flanges with closed-cell foam gaskets to form an air-tight seal. The face velocity of air for filtration tests was controlled by MFC before the Venturi vacuum pump. The MFC was protected by two inline HEPA filters. The laser particle counter used for efficiency tests was LAS-X II from Particle Measuring Systems (Boulder, CO). It is a laser particle counter with a range of 90-7500 nm with over 100 selectable channel sizes. The sample size of the particle counter can be varied from 10 cc/min to 100 cc/min, which was well suited for small-scale laboratory testing. The sample size was 50 cc/min for all tests, which was 1.7% of the total flow through the filter media at 10 cm/s face velocity. The filtration tests were carried out at a face velocity of 10 cm/s unless noted otherwise. The filtration efficiency was calculated as per the ASHRAE 52.2 standard [II.10], with 7-10 samples of 1 min each. Error bars for 95% confidence interval are reported in the filtration efficiency data as per the ASHRAE 52.2 standard. The relative humidity of the air with potassium chloride particles was always less than 5%. Potassium chloride droplets form solid particles for relative humidity of less than ~70% [II.10]. The pressure drop across the filter media was measured at different face velocities using an Omega (Product # PX154-010DI) pressure transducer. To measure pressure drop across the filter media using the same setup, the exhaust and air flow through the nebulizer were closed, and the vacuum line to the pipe was opened for ambient pressure exhaust. In all tests, 2-4 samples were analyzed to check for the repeatability of data and to determine the experimental error.

II.4 Results and Discussion

II.4.1 Sintered metal microfibrous (SMM) matrix/filter media

The measured thicknesses of the SMM matrices, the voidage and packing fraction calculated based on their thicknesses are shown in Table II-1. The SMM filter media of different fiber diameters had a different thickness after compression due to the spring back action of the filter media after the removal of the compression load. The various thickness measurements of a particular fiber diameter filter media did not vary significantly. Therefore, the pressure drop and filtration efficiencies of the filter media were consistent. These compressed SMM filter media were used as substrates for CNS synthesis.

Table II-1. Thickness, voidage and packing fraction of fibers of SMM matrices.

	12 µm SMM matrix	**8 µm SMM matrix**	**4 µm SMM matrix**
Thickness (mm)	0.41 ±0.02	0.36 ±0.01	0.43 ±0.01
Voidage (%, cal.)	79.0 ±1.0	76.1 ±0.5	80.0 ±0.5
Packing fraction (%, cal.)	21.0 ±1.0	23.9 ±0.5	20.0 ±0.5

II.4.2 Synthesis of carbon nanostructures (CNS)

The intention of this study was to synthesize carbon nanofibers (CNF) uniformly within the SMM matrices. However, amorphous carbon was the byproduct of CNF synthesis. CNF and amorphous carbon are together termed as carbon nanostructures (CNS) for this study. The CNF synthesis requires energy, a catalyst and a carbon source. Hydrocarbon gases are typically used as the carbon source for the synthesis of CNF [II.11]. In this study, acetylene (C_2H_2) decomposition provided the carbon for CNF synthesis on SMM matrices. Iron (Fe), nickel (Ni) and cobalt (Co) are known to be active catalysts for carbon nanotubes and CNF synthesis [II.12, 13]. Therefore, nickel metal fibers act as a catalyst for synthesis of CNF by decomposition of

hydrocarbon gas. There exists a temperature range from ~400 ˚C to ~700 ˚C where the nickel metal is an active catalyst for CNF synthesis [II.14, 15]. Beyond this temperature range, no CNF were observed on the bulk nickel metal catalyst due to catalyst poisoning or deviation from equilibrium required for CNF synthesis [II.14]. Hydrogen gas is required to keep the catalyst active during CNF synthesis [II.16], and a high fraction of hydrogen gas increases the reaction kinetics of CNF formation [II.14, 17]. Nitrogen was used as an inert gas in this study. Optimization of synthesis conditions involved reducing the reaction kinetics of CNF synthesis by lowering the synthesis temperature while limiting the fraction of hydrogen in the synthesis gas. Without this optimization, CNF were not deposited throughout the depth of the matrices because acetylene decomposed near the first few layers of the highly active SMM nickel catalyst. Uniform synthesis of CNS in 3-dimensional SMM matrices was the result of the optimized synthesis conditions and flow directions chosen for synthesis.

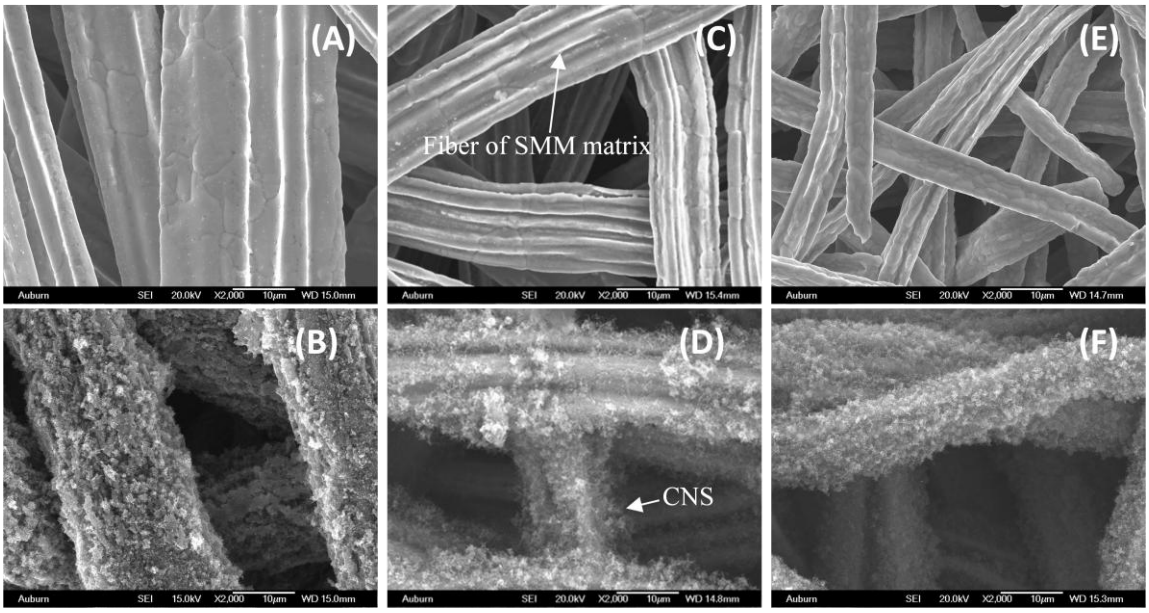

Fig. II-4. SEM images: (A) 12 µm SMM matrix before synthesis, (B) 12 µm SMM matrix after 11 min synthesis, (C) 8 µm SMM matrix before synthesis, (D) 8 µm SMM matrix after 11 min synthesis, (E) 4 µm SMM matrix before synthesis, (F) 4 µm SMM matrix after 11 min synthesis.

Fig. II-4 (A) and (B) shows the SEM images of 12 μm nickel SMM matrix before and after an 11 min synthesis. It is evident that the morphology of the nickel fiber surface changed significantly and the effective diameter of nickel fibers increased after the synthesis of CNS. A similar change in morphology of the fiber surface and the increase in effective diameter can also be seen for the 8 μm SMM matrix and 4 μm SMM matrix in Fig. II-4. Table II-2 shows the packing fraction of carbon synthesized within SMM matrices assuming a density of 1.9 g/cc for the carbon deposit. Fig. II-5 (A) shows the typical difference between the samples before and after synthesis. Fig. II-5 (B), (C) and (D) show various resolution SEM images of the carbon synthesized within 8 μm SMM at the locations on the sample shown in Fig. II-5 (A). The spatial uniformity of CNS synthesis along the face of the filter (direction perpendicular to flow) is evident from no significant variation in morphology of filter fiber surface at various locations on the sample as shown in the Fig. II-5 (B), (C) and (D). The uniformity of CNS synthesis in the direction perpendicular to flow is as expected because the SMM acts as a catalyst bed with no variation of acetylene concentration in the radial direction during synthesis.

Table II-2. CNS packing fraction in SMM matrices.

	CNS packing fraction (%, cal.)		
Synthesis time (min.)	**12 μm SMM matrix**	**8 μm SMM matrix**	**4 μm SMM matrix**
5.5	5.9	6.7	5.6
11	11.8	13.4	11.2

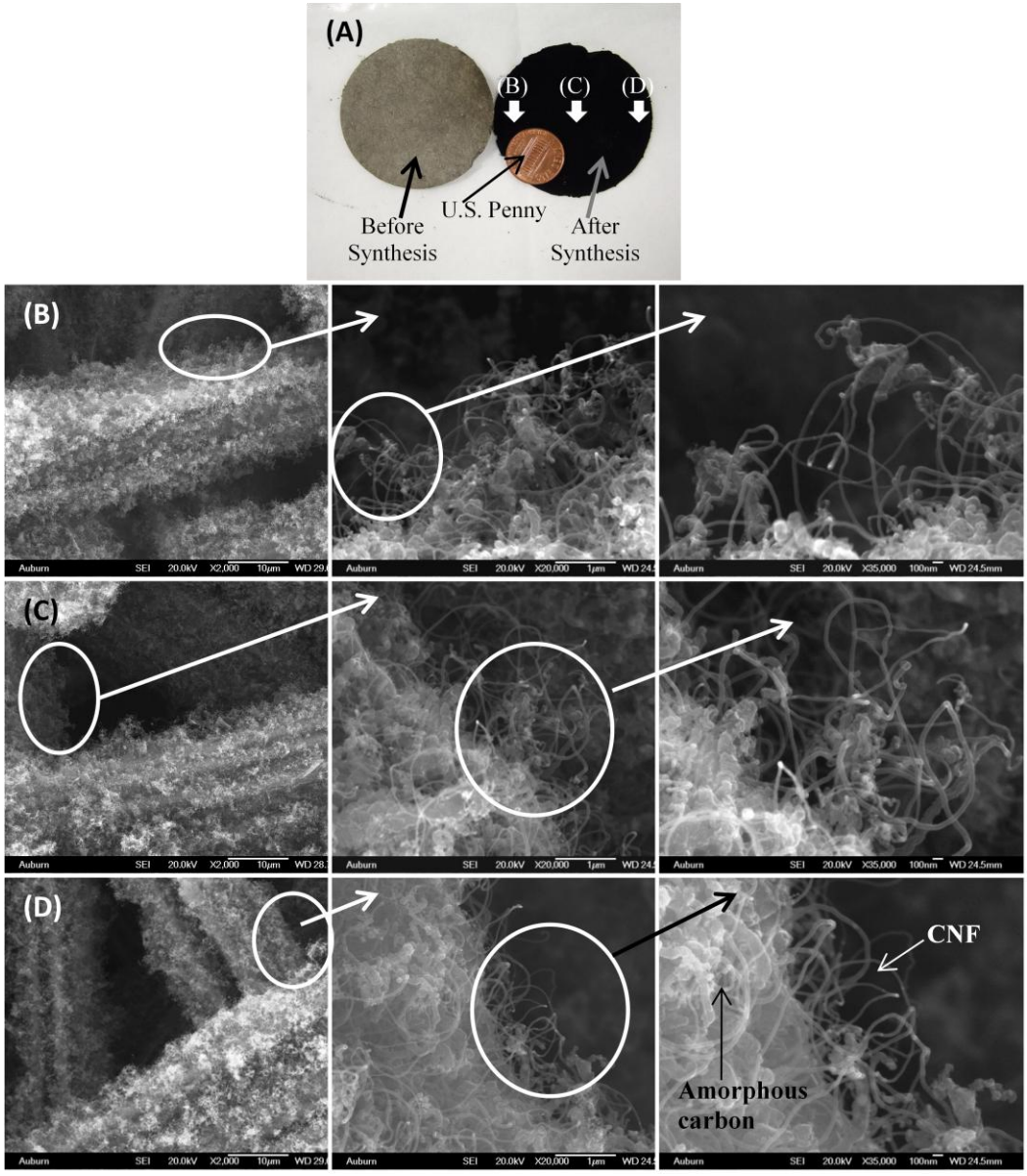

Fig. II-5. (A) Photograph of samples before and after synthesis, (B), (C) and (D) various resolution SEM images of synthesized CNS at different locations for 8 μm SMM matrix.

Amorphous carbon is a byproduct of the CNF synthesis process that cannot be avoided since the synthesis conditions were optimized for reducing reaction kinetics of CNF synthesis to obtain 3-dimensional deposition of carbon within the matrix. Most of the amorphous carbon is seen adhered to the surface of nickel fibers (Fig. II-5 (D)) and the CNF protrude away from the

nickel fiber surface due to their high aspect ratio. The enhancement in filtration performance by CNS synthesis is attributed to the CNF protruding out in the air flow field.

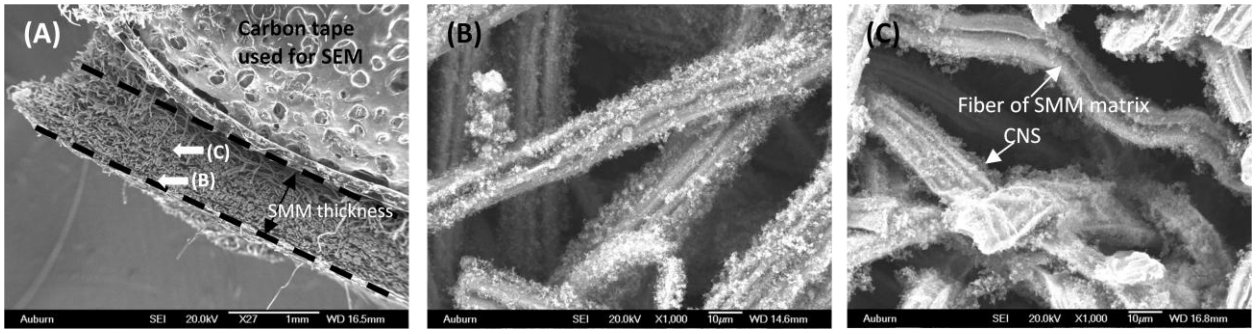

Fig. II-6. SEM images of cross-sectional view of 8 μm SMM matrix after 11 min synthesis: (A) low magnification (27X), (B) high magnification (1000X) of the spot shown on edge of the matrix thickness in low magnification image, and (C) high magnification (1000X) of the spot shown on centerline of the matrix thickness in low magnification image.

Fig. II-6 (A) shows the SEM image of the cross-section of an 8 μm SMM matrix with a total synthesis time of 11 min. The CNS were clearly deposited even on the centerline of the filter media thickness shown in Fig. II-6 (C). However, some gradient in CNS growth exists from the face of the filter media to the centerline of the filter media thickness due to the high catalytic activity of nickel towards the decomposition of acetylene, as seen in the small difference of CNS coverage between Fig. II-6 (B) and (C). This gradient of CNS growth from the edge to the centerline of SMM is very prominent if the synthesis is carried out in a higher reaction kinetic regime which was done as a part of optimization of synthesis conditions (not shown here). The gradient of CNS growth along the thickness of the matrices was minimized by the optimization of the synthesis conditions, but it cannot be completely eliminated. The increase in weight of SMM matrices after synthesis due to the deposited CNS accounted for ~95% of the carbon supplied in the form of acetylene gas. It can be concluded that very little or no acetylene was

leaving in the exit stream of the reactor. The Raman spectroscopy shown in Fig. II-7 gave the ratio of sp^3 to sp^2 (D/G ratio) carbon content of synthesized CNS to be 0.91, which is not abnormal for multi-walled carbon nanotubes and CNF with diameters more than 50 nm. The observed sp^2 hybridized carbon is from the graphene layers in CNF. The sp^3 hybridized carbon seen in Raman spectroscopy can be a part of the sp^3 carbon in CNF or the byproduct of amorphous carbon. There is no accurate method to distinguish between the two forms of sp^3 carbon deposits. SEM images with Raman spectroscopy give a qualitative understanding of the carbon deposit.

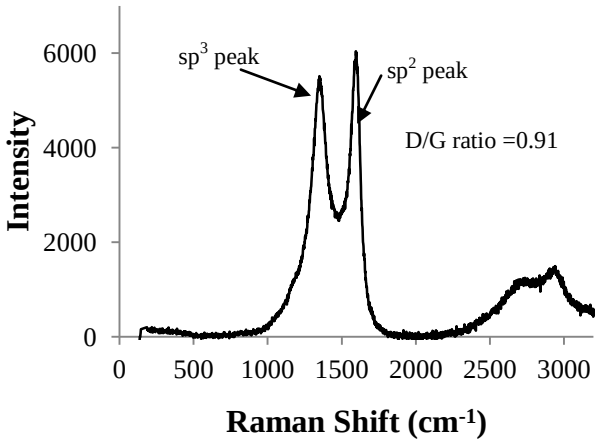

Fig. II-7. Raman spectroscopy of CNS synthesized on SMM matrices (514 nm laser)

The synthesized CNS adhered well to the SMM matrices because no shedding of CNS was observed by the particle counter when HEPA filtered particle free air was passed through the sample up to face velocities of 40 cm/s. Above 40 cm/s, the HEPA filtered air started getting contaminated by the particles dislodged from the walls of the test setup. The dislodged particles were of very low concentration at 10-200 particles per 100 cc, but it did not allow for discrimination between the dislodged potassium chloride particles and the shed CNS. Air was passed at a higher face velocity of 70 cm/s for more than 20 min to gravimetrically measure any

loss of CNS. No measurable difference was seen in the weights of the samples. This proves that the structure was very stable at least up to the face velocity of 40 cm/s.

II.4.3 Porometry

Capillary porometry was used to measure the variation in mean pore diameter and bubble point diameter of matrices due to synthesis of CNS. The formula used as the basis for the pore diameter calculations is shown in Eq. (II.1), where d is the pore diameter (m), σ is the surface tension of liquid (J/m^2), θ is contact angle between liquid and pore wall (^{o}) and p is the pressure (Pa) for displacing liquid from pore diameter (d) [II.18]. With low surface tension liquids, like the one used in this study, the contact angle can be assumed to be 0^o [II.19]. The measurements involving low surface tension liquids on various filters have shown that the measured pore diameters were independent of the materials used for the filter [II.19]. Because of these reasons, porometry can be used to accurately determine the pore diameters of the filters as the Galwick^{TM} liquid will have good wettability with metal and CNS. Also, the test results were exactly the same for samples tested with the wet first-dry second cycle and for samples tested with the dry first-wet second cycle in porometry. Wet first-dry second means that the wet curve was done first followed by the dry curve. The non-varying results for multiple samples imply that the structures were stable for both parts of the cycle during the porometry test.

$$d = \frac{2.86\sigma \cos\theta}{p} \qquad \text{(II.1)}$$

As shown in Fig. II-8, the mean pore diameter decreased with increasing synthesis time for all SMM matrices. For a 12 μm SMM filter media, the mean pore diameter did not decrease significantly from CNS-0 to CNS-5.5. However, it decreased significantly from CNS-5.5 to CNS-11. Similar results can be seen for the 8 μm SMM matrix. However, for the 4 μm SMM

matrix, the pore size decreased significantly from CNS-0 to CNS-5.5 and continued to decrease for CNS-11. As shown in Table II-3, there was a small decrease in the bubble point, which was overshadowed by the sample-to-sample error involved in the measurement of the bubble point.

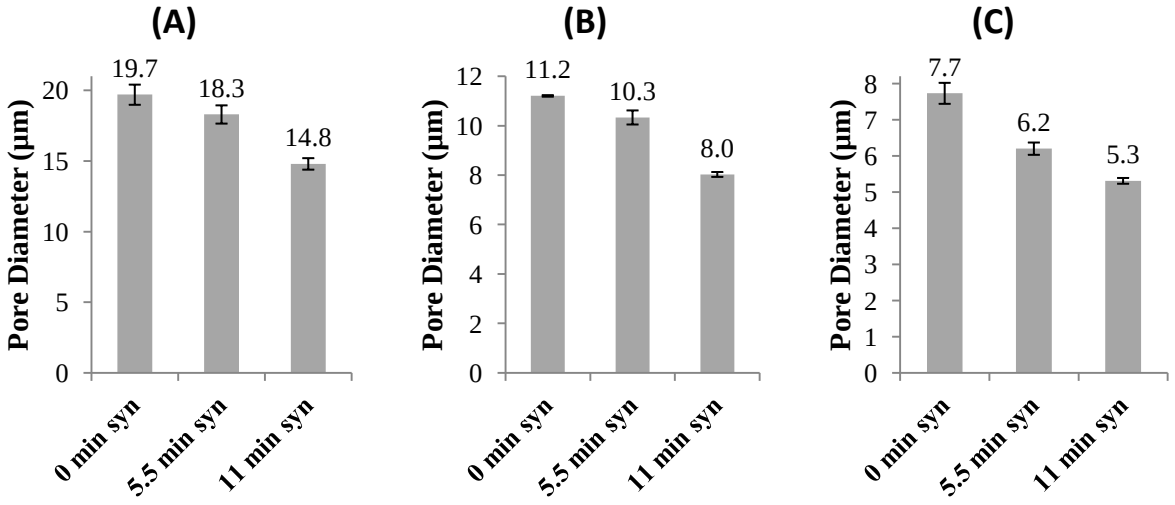

Fig. II-8. Mean pore diameter for SMM matrices with respect to the synthesis time of CNS: (A) 12 µm SMM matrix, (B) 8 µm SMM matrix and (C) 4 µm SMM matrix.

Table II-3. Bubble point diameter of SMM matrices with respect to CNS synthesis time (maximum error ±5%).

Synthesis time (min)	Bubble point diameter (µm)		
	12 µm SMM matrix	8 µm SMM matrix	4 µm SMM matrix
0	41.0	20.5	16.3
5.5	37.7	21.6	14.7
11	37.1	20.1	14.4

Table II-4. Maximum penetration particle size (MPPS) with respect to CNS synthesis time.

Synthesis time (min)	MPPS (nm)		
	12 µm SMM matrix	8 µm SMM matrix	4 µm SMM matrix
0	220	180	180
5.5	180	140	120
11	120	120	120

II.4.4 Filtration efficiency

The filtration efficiency increases with synthesis time for 12 µm, 8 µm and 4 µm SMM matrices as shown in Fig. II-9 (A), (B) and (C), respectively. The resolution in data allows us to see the change in maximum penetration particle size (MPPS) with respect to synthesis time. As shown in Table II-4, the MPPS shifted to a lower particle size with synthesis time for all SMM matrices. A decrease in MPPS with increasing filtration efficiencies has also been observed by other researchers [II.6, 20]. The Fig. II-9 (D) shows the increasing filtration efficiency with CNS synthesis time for aerosol particles from 90 nm to 2500 nm for 8 µm SMM matrix as an example of the quality of data collected. This increasing filtration efficiency with CNS synthesis time for all aerosol particles indicates that the filtration efficiency increased for diffusion, interception and inertial impaction mechanisms of particle capture. The limited sensitivity (90-7500 nm aerosol particles) of the laser particle counter used in this study did not allow for detailed study of the diffusion mechanism of particle capture (<100 nm aerosol particles). However, contemplating the extrapolation of filtration efficiency data below 90 nm for Fig. II-9 (A), (B) and (C), using the widely accepted trend of decreasing filtration efficiency with increasing aerosol particle size up to MPPS [II.21] indicates that the filtration efficiency will probably increase with CNS synthesis time for diffusion mechanism dominant regime. This filtration

efficiency trend below 90 nm could not be experimentally verified due to our limited capabilities in aerosol measurement.

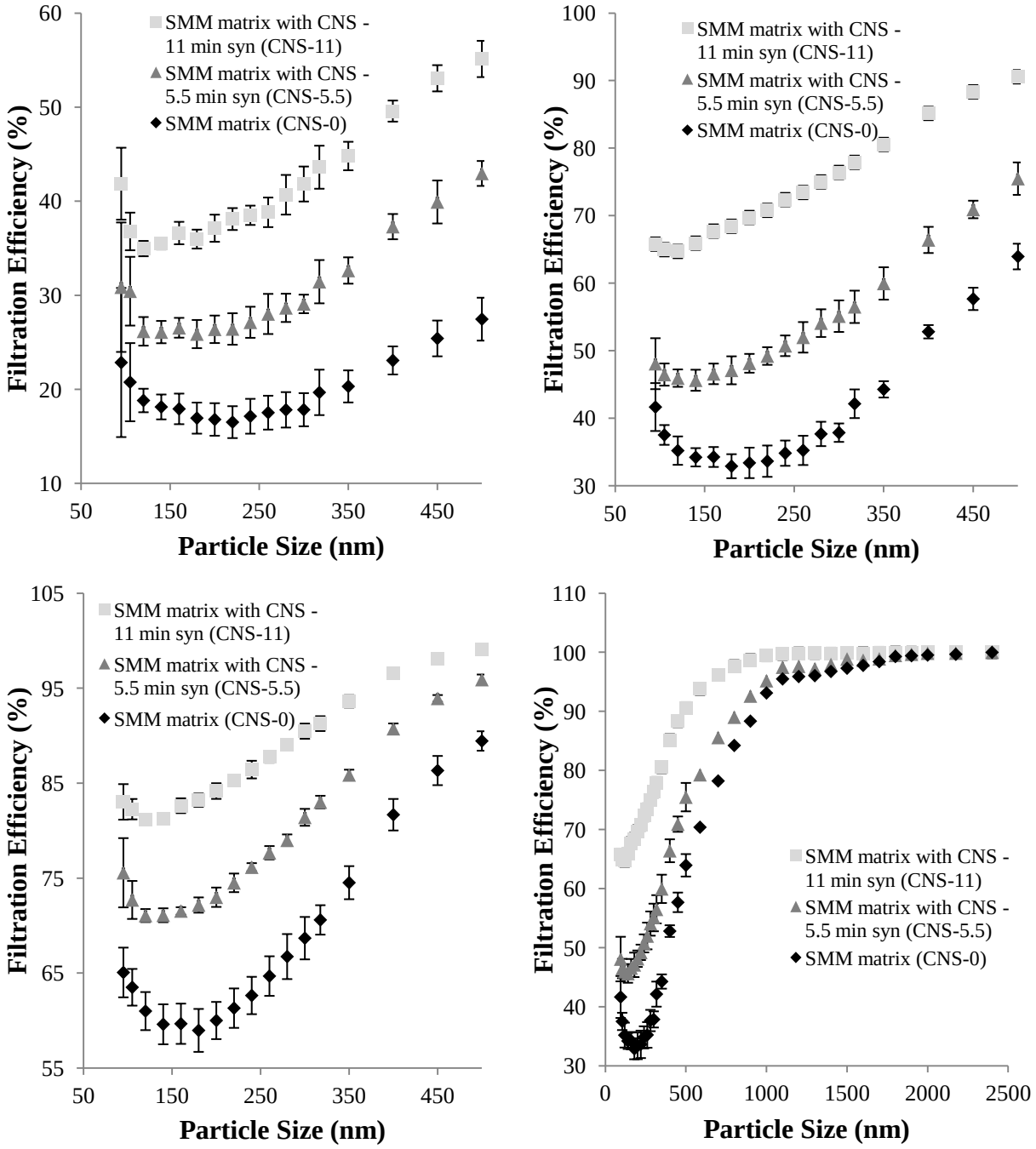

Fig. II-9. Aerosol filtration efficiency with respect to particle size: (A) 12 µm SMM matrix, (B) 8 µm SMM matrix, (C) 4 µm SMM matrix, (D) 8 µm SMM matrix for particle size range from 90 nm to 2500 nm. (Face velocity during test: 10 cm/s.)

The Fig. II-10 (A) and (B) show the change in filtration efficiency at different face velocities for the 8 µm SMM before and after an 11 min synthesis, respectively. As shown in Fig. II-10 (A) and (B), the filtration efficiency decreases with an increase in face velocity for smaller particles (less than ~200 nm). This is the same trend which is seen for the diffusion mechanism dominant regime under varying face velocities [II.21]. For aerosol particles above 400 nm, the filtration efficiency increased with an increase in face velocity which is seen for the inertial impaction dominant regime [II.21]. The interception mechanism is the only mechanism of filtration not dependant on the face velocity of filtration [II.21, 22]. The intersection of the filtration efficiency curves obtained at various face velocity gives the filtration efficiency independent of face velocity. This filtration efficiency, independent of face velocity, is termed here as interception filtration efficiency. The interception filtration efficiency before synthesis was ~40% (Fig. II-10 (A)) and was ~72% (Fig. II-10 (B)) after synthesis. This enhancement of filtration can be attributed to the CNF protruding away from the nickel fiber surface and into the flow field of air (detailed discussion in Section 3.7).

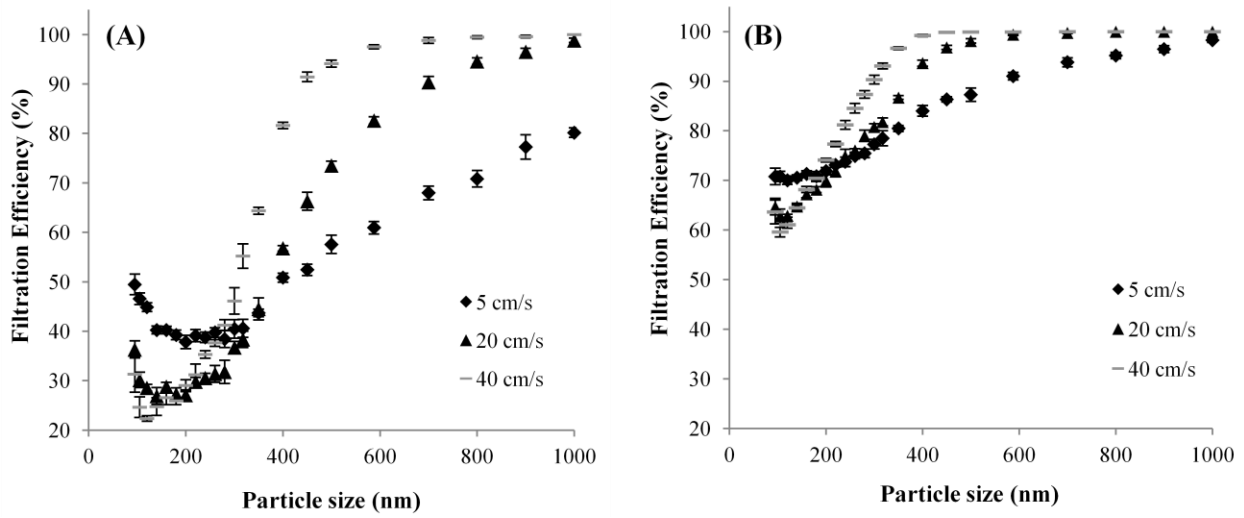

Fig. II-10. Aerosol filtration efficiency with respect to particle size at different face velocities for 8 µm SMM matrix (A) before synthesis and (B) after an 11 min synthesis.

II.4.5 Pressure drop across filter media

Pressure drop (ΔP) across filter media, following Darcy's law, is dependent on various factors as shown in Eq. (II.2), where "η" is viscosity of the gas, "Q" is the flow rate across filter media, "h" is the filter media thickness, "A" is the area of filter media , "R" is the mean radius of filter fiber, "c" is the packing density and "Q/A" gives the face velocity of air at the filter media [II.23].

$$\Delta P = \frac{\eta Q h\, f(c)}{A R^2} \qquad \text{(II.2)}$$

In this study, all the parameters for different SMM matrices were the same except for the mean radius of fibers (R) and the experimental variation of matrix thickness (h). The pressure drop across the matrix increases as the mean radius of the fiber (R) decreases. This can be observed in Fig. II-11 (A). However, the pressure drop observed for various matrices do not follow the classical pressure drop relationship (Eq. (II.2)) with the radius of the fiber. This is

because the mean radius of the fiber (R) used in the equation cannot be correlated with the nominal radius of fibers due to the ribbon shape of the fibers and the non-homogeneous growth of the CNS within the SMM matrices.

The pressure drop across the filter media is expected to increase with the synthesis of CNS as it changes the filter fiber surface morphology and decreases the effective pore diameter of the filter media. As shown in Fig. II-11 (B), the pressure drop of the 12 μm SMM matrix increased with an increase of CNS content. The pressure drop increased significantly from CNS-5.5 to CNS-11, but did not increase as much from CNS-0 to CNS-5.5. The pressure drop data for SMM matrices of all diameters closely follows the same trend as the mean pore diameter data observed by porometry. From the data we can deduce that the change in surface morphology of nickel fibers by CNS synthesis, which was the main contributor to filtration efficiency, may not be a significant contributor to pressure drop as compared to the decrease in mean pore diameter of the matrix.

As shown in Fig. II-11 (C), the pressure drop data for the 8 μm SMM matrix are similar to those for the 12 μm SMM matrix, with an incremental increase in pressure drop from CNS-0 to CNS-5.5 and then a significant increase from CNS-5.5 to CNS-11. The proposed hypothesis is further bolstered by the pressure drop data for the 4 μm SMM matrix, as shown in Fig. II-11 (D). For the 4 μm SMM matrix, the pressure drop of CNS-5.5 is significantly higher than that of CNS-0 and continues to rise until CNS-11 due to the significant decrease in effective pore diameter of the filter media as observed by porometry. Since the 4 μm SMM filter media has a smaller initial pore diameter, any synthesis of CNS decreased the effective pore diameter, which resulted in a significant increase in the pressure drop as compared to a SMM filter media of larger diameter. The pressure drop across the filter media is very sensitive to the pore diameter

because the interstitial velocity in the filter media is inversely proportional to the square of the pore diameter.

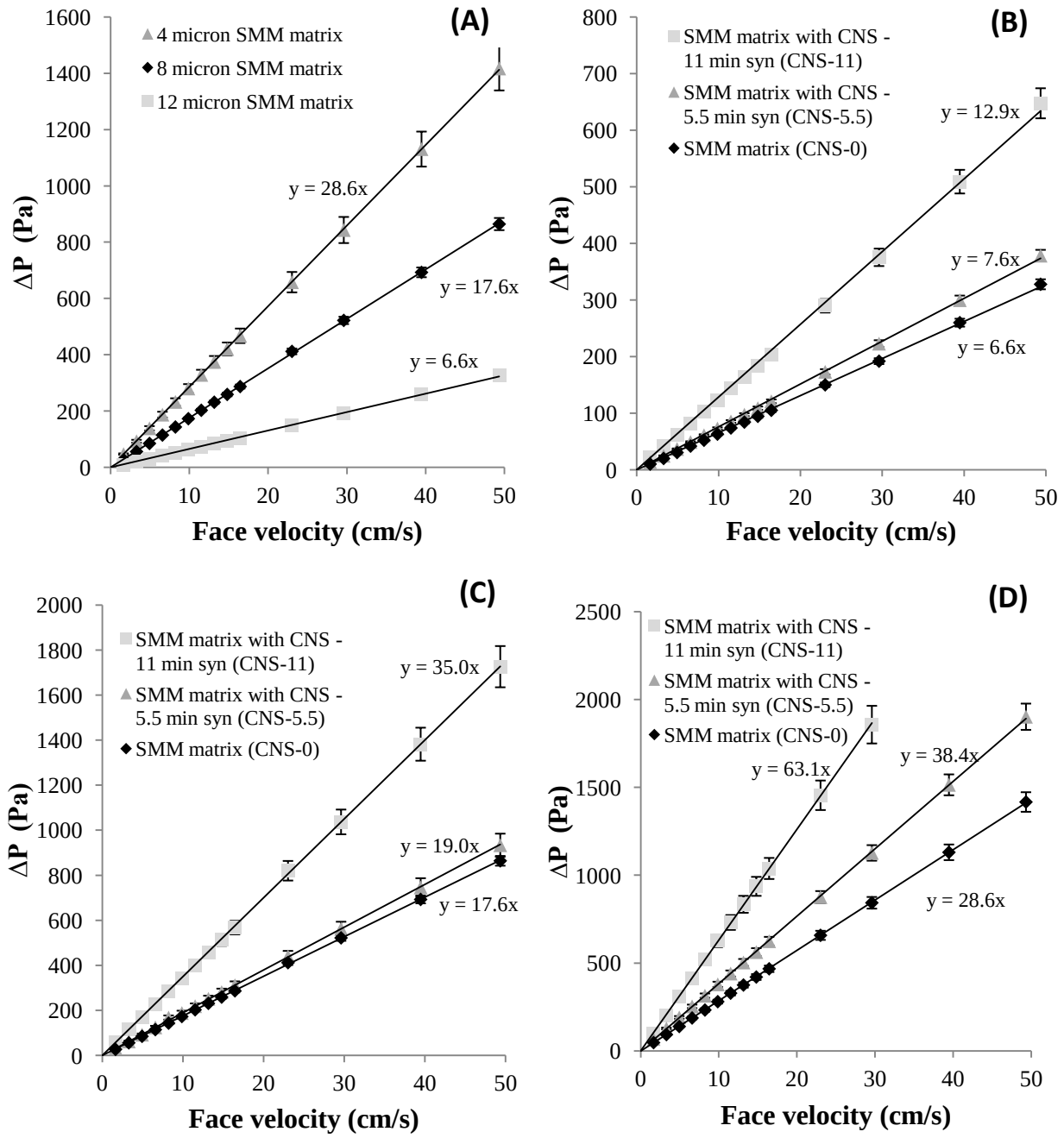

Fig. II-11. Pressure drop across matrices with respect to face velocity for (A) All SMM matrix, (B) 12 µm SMM matrix, (C) 8 µm SMM matrix and (D) 4 µm SMM matrix.

II.4.6 Quality factor calculations

The quality factor (QF) of a filter media can be a helpful measure of whether an increase in pressure drop is warranted by the increase in filtration efficiency. The QF [II.22, 24] is also known as filter quality [II.25] and index of filtration [II.26] and is defined by Eq. (II.3), where "E" is the filtration efficiency in fraction and "ΔP" is the pressure drop across the filter media. A higher QF indicates that the filtration is better per unit of pressure drop.

$$QF = \frac{-\ln(1-E)}{\Delta P} \tag{II.3}$$

The QF changes with dirt loading of the filter. The QF calculated for this study is based on initial (stationary) performance of a clean filter media with no dirt loading. As shown in Fig. II-12 (A), (B) and (C), the QF for 12 µm, 8 µm and 4 µm SMM matrices increased from CNS-0 to CNS-5.5. This indicates that there was an improvement in aerosol filtration performance due to synthesis of CNS for 5.5 min. However, for CNS-11, the QF was less than or equal to CNS-5.5 and greater than the QF of CNS-0 for 12 µm and 8 µm SMM matrices. This implies that the benefit of CNS synthesis decreased for CNS-11 due to the significant reduction in pore diameter of the matrix as observed by porometry. This decline in benefit was predominantly seen in the QF for the 4 µm SMM matrix. For the 4 µm SMM matrix, the QF of CNS-11 was even less than that of CNS-0 (Fig. II-12 (C)). This suggests that the increase in pressure drop negated the effect of the increase in filtration efficiency from CNS synthesis. The physical significance of the QF calculations, for 4 µm SMM matrix, is that a larger thickness of CNS-0 will have higher filtration efficiency than the CNS-11 for the same pressure drop penalty.

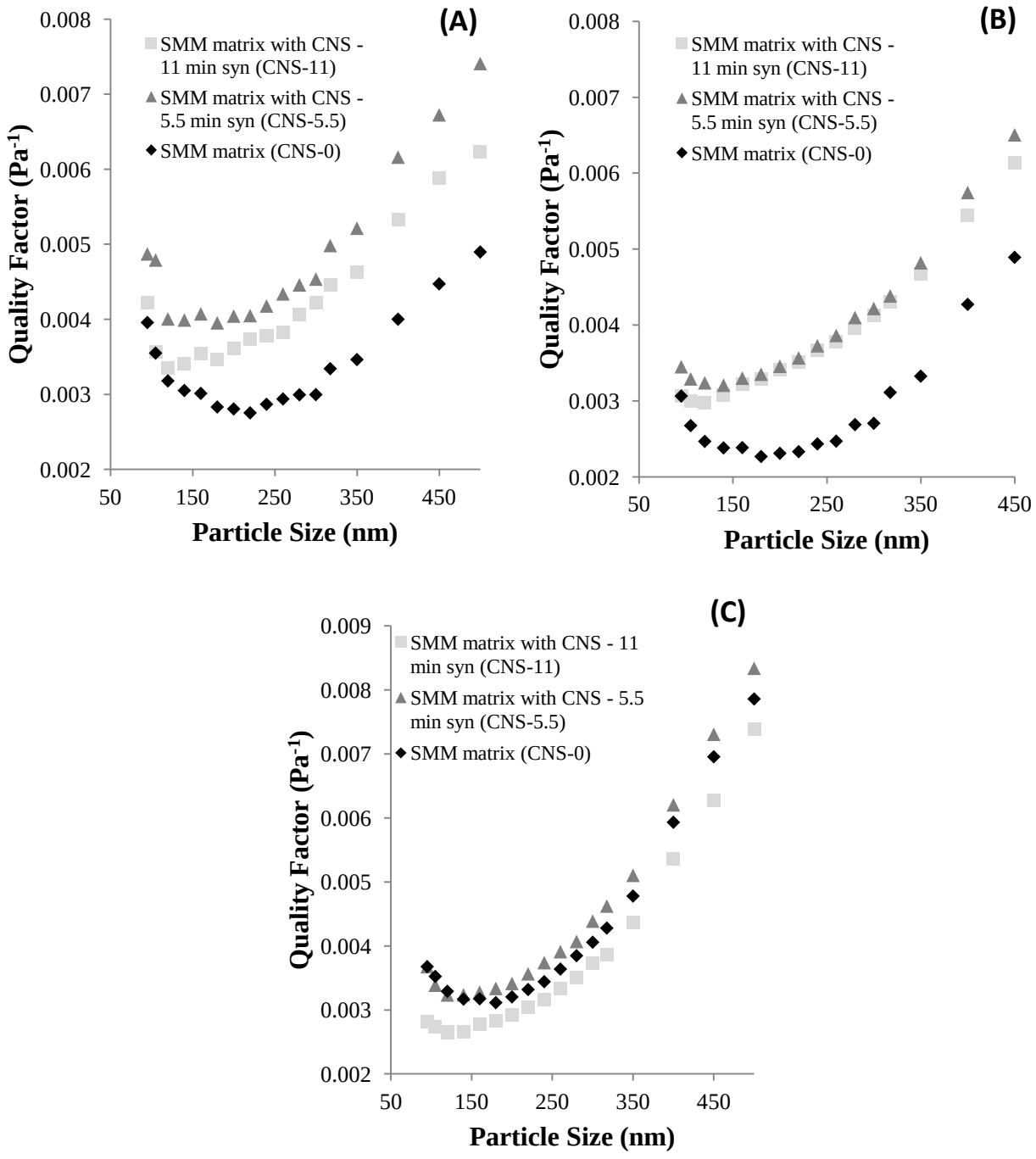

Fig. II-12. Quality factor (cal.) with respect to aerosol particle size for size range of 90 nm to 500 nm: (A) 12 µm SMM matrix, (B) 8 µm SMM matrix and (C) 4 µm SMM matrix.

II.4.7 Hypothesis: Effect of carbon nanostructure (CNS) synthesis

As the fiber diameter approaches the mean free path of air (65 nm at STP), air cannot be treated as a continuous fluid and modifications have to be made to the continuum mechanics boundary conditions to include the molecular movement of air. This modification is called the slip flow in which the drag force per unit filter fiber surface area is lower than that of non-slip flow. The velocity of air at the fiber surface is considered to be non-zero for slip flow, resulting in less resistance to flow for the same fiber surface area. Therefore, filtration efficiency can increase without a significant increase in pressure drop by adding nanofibers to the filter media [II.27]. The molecular movement of a fluid is described by the Knudsen number (Kn), as shown in the Eq. (II.4), where "λ" is the mean free path of air and "R" is the mean radius of the fiber [II.28]. For Kn>0.1, wall slip on fibers is generally taken into account [II.27]. Therefore, slip flow at the fiber surface is an important factor that has to be considered for nanofibers in filter media having diameters less than 500 nm where Kn>0.25 (at STP) [II.27, 28].

$$Kn = \frac{\lambda}{R} \tag{II.4}$$

The experimental data shows that there is a significant improvement in the performance of the filter because of the synthesized CNS on the filter fibers. The increase in filtration efficiency seen for CNS-5.5 (Fig. II-9) accompanied by lower than expected increase in the pressure drop (Fig. II-11) may be attributed to the wall slip flow over nanofibers. The mechanism of CNS synthesis dictates that the amorphous carbon part of the CNS typically adheres to the catalyst surface and the nanofibers extrude away from the catalyst surface due to their high aspect ratio [II.14, 29, 30]. We hypothesize that CNF, with diameters around 100 nm, protrude in the air flow field due to their high aspect ratio (Fig. II-5 (D)) and enhance the capture

of aerosol particles without significant increase in pressure drop because of wall slip flow over them. As shown in Fig. II-9 (D), the filtration efficiency increased with CNS synthesis time for interception and inertial impaction mechanisms of particle capture. As discussed in Section 3.4, we contemplated the extrapolation of data which indicates that there is probably an increase in filtration efficiency with CNF synthesis time for diffusion mechanism dominant regime (<100 nm). We hypothesize that the synthesized CNF provides additional surface area which enhances the filtration efficiency in the diffusion dominant regime because there is more surface area to which the smaller particles can 'diffuse'. Also, the CNF protruding in the air flow field act as additional fibers (nanofibers) around which the air has to flow, leading to enhanced capture of aerosol via interception mechanism due to increased aerosol-fiber contact. The increase in inertial impaction dominant regime may be because of the increased media interstitial air velocity caused by the decrease in pore diameters after CNS synthesis.

It was demonstrated that the filtration efficiency and the pressure drop increased with the quantity of CNS. The increase in filtration efficiency with CNS synthesis time implies that the increasing length of protruding CNF contributed to the increase in filtration efficiency. Also, the increase in pressure drop with CNS synthesis time was mainly caused by reduction in the pore size of the filter media. Therefore, there were two conflicting parameters of CNS synthesis, viz:, increase in the filtration efficiency attributed to protruding CNF, and decrease in pore size, which increased the pressure drop. These two conflicting parameters were seen clearly in QF calculations. The CNS-5.5 had the best QF for SMM matrices of all diameters because the pore size had not decreased significantly and CNF provided higher filtration efficiency. This proved that there were limited enhancements in aerosol filtration by CNS synthesis on SMM filter media

due to the reduction in mean pore size of filter media, which counteracted the advantage of filtration enhancement due to wall slip over nanofibers.

II.5 Conclusions

An enhancement in aerosol filtration due to slip flow over nanofibers was sought to create a depth nanofiber-filter media with high filtration efficiency, low pressure drop and high dirt holding capacity. Carbon nanofibers (CNF) along with byproduct of amorphous carbon were synthesized within the matrix/filter media to create a depth filter with uniform 3-dimensional deposition of carbon nanostructures (CNS) throughout the matrix. It was observed that the synthesized CNS adhered well to the sintered metal microfibrous (SMM) matrices and did not shed. The CNS synthesis on three different matrices with varying mean pore diameter showed that there was a significant improvement in aerosol filtration efficiency of SMM matrices after synthesis. This increase in filtration efficiency without a substantial increase in the pressure drop was attributed to the wall slip flow over the protruding CNF. Quality factor (QF) calculations revealed that this advantage of enhanced filtration efficiency by CNF was counteracted by the disadvantage of a decrease in mean pore diameter of the filter media due to synthesis. This decrease in mean pore diameter was the primary cause of an increase in the pressure drop across the filter media. Thus, it can be concluded that an optimization of CNS synthesis is required for increasing filtration efficiency without substantially increasing the pressure drop. This study also shows that the enhancement in aerosol filtration due to CNS synthesis is maximized for matrices with large pores as the pore diameters do not reduce significantly with CNS synthesis. Maximum penetration particle size (MPPS) was observed to decrease with an increase in CNS synthesis time. The optimization of CNF synthesis conditions for 3-dimensional growth within SMM matrices is discussed in the next chapter.

II.6 References

[II.1] F. Dotti, A. Varesano, A. Montarsolo, A. Aluigi, C. Tonin, G. Mazzuchetti, Electrospun porous mats for high efficiency filtration, J. Ind. Text. 37 (2007) 151-162.

[II.2] P. Heikkila, A. Taipale, M. Lehtimaki, A. Harlin, Electrospinning of polyamides with different chain compositions for filtration application, Polym. Eng. Sci. 48 (2008) 1168-1176.

[II.3] K. Kosmider, J. Scott, Polymeric nanofibres exhibit an enhanced air filtration performance, Filtr.+Sep. 39 (2002) 20-22.

[II.4] P. Madhavamoorthi, "Nanofibers and nanofiber web" : a new class of nonwovens, Synth. Fibres 34 (2005) 12-18.

[II.5] T. Grafe, K. Graham, Polymeric nanofibers and nanofiber webs: A new class of nonwovens, Int. Nonwovens J. 12 (2003) 51-55.

[II.6] W.W. Leung, C. Hung, Investigation on pressure drop evolution of fibrous filter operating in aerodynamic slip regime under continuous loading of sub-micron aerosols, Sep. Purif. Technol. 63 (2008) 691-700.

[II.7] G. Viswanathan, D.B. Kane, P.J. Lipowicz, High efficiency fine particulate filtration using carbon nanotube coatings, Adv. Mater. 16 (2004) 2045-2049.

[II.8] S.J. Park, D.G. Lee, Performance improvement of micron-sized fibrous metal filters by direct growth of carbon nanotubes, Carbon 44 (2006) 1930-1935.

[II.9] S.J. Park, D.G. Lee, Development of CNT-metal-filters by direct growth of carbon nanotubes, C. Appl. Phys. 6 (2006) e182-e186.

[II.10] ASHRAE 52.2, Method of testing general ventilation air-cleaning devices used for removal efficiency by particle size, American National Standard, Atlanta, GA, U.S.A., 1999.

[II.11] L.S. Lobo, D.L. Trimm, Carbon formation from light hydrocarbons on nickel, J. Catal. 29 (1973) 15-19.

[II.12] Z.P. Huang, D.Z. Wang, J.G. Wen, M. Sennett, H. Gibson, Z.F. Ren, Effect of nickel, iron and cobalt on growth of aligned carbon nanotubes, Appl. Phys. A: Mater. Sci. Process. 74 (2002) 387-391.

[II.13] T. Baird, J.R. Fryer, B. Grant, Carbon formation on iron and nickel foils by hydrocarbon pyrolysis: Reactions at 700^{o}C, Carbon 12 (1974) 591-602.

[II.14] C.A. Bernardo, L.S. Lobo, Kinetics of carbon formation from acetylene on nickel, J. Catal. 37 (1975) 267-278.

[II.15] Y. Nishiyama, Y. Tamai, Effect of hydrogen on carbon deposition catalyzed by copper-nickel alloys, J. Catal. 45 (1976) 1-5.

[II.16] M.S. Kim, N.M. Rodriguez, R.T.K. Baker, Interaction of hydrocarbons with copper-nickel and nickel in the formation of carbon filaments, J. Catal. 131 (1991) 60-73.

[II.17] R.T.K. Baker, M.A. Barber, P.S. Harris, F.S. Feates, R.J. Waite, Nucleation and growth of carbon deposits from the nickel catalyzed decomposition of acetylene, J. Catal. 26 (1972) 51-62.

[II.18] I.M. Hutten, Handbook of Nonwoven Filter Media, first ed., Butterworth-Heinemann, Oxford, 2007.

[II.19] V. Gupta, A.K. Jena, Substitution of alcohol in porometers for bubble point determination, Adv. Filtr. Sep. Technol. 13B (1999) 833-844.

[II.20] A. Podgorski, A. Balazy, L. Gradon, Application of nanofibers to improve the filtration efficiency of the most penetrating aerosol particles in fibrous filters, Chem. Eng. Sci. 61 (2006) 6804-6815.

[II.21] D. Boulard, A. Renoux, Stationary and Nonstationary Filtration of Liquid Aerosols by Fibrous Filters, K.R. Spurny (Ed.) Advances in aerosol filtration, Lewis, 1998, pp. 53-83.

[II.22] R.C. Brown, Air filtration: an integrated approach to the theory and applications of fibrous filters, Pergamon Press, 1993.

[II.23] C.N. Davies, Air Filtration, first ed., Academic Press, 1973.

[II.24] W. Moelter, H. Fissan, Quality assurance of glass fiber filter media, K.R. Spurny (Ed.) Advances in aerosol filtration, Lewis, 1998, pp. 259-282.

[II.25] W.C. Hinds, Aerosol technology : properties, behavior, and measurement of airborne particles, first ed., Wiley, New York, 1982.

[II.26] D.R. McFee, J. Sedlet, Plutonium-uranium-molybdenum fume characteristics and sand filtration, J. Nucl. Energy 22 (1968) 641-650.

[II.27] R.S. Barhate, S. Ramakrishna, Nanofibrous filtering media: Filtration problems and solutions from tiny materials, J. Membr. Sci. 296 (2007) 1-8.

[II.28] K. Graham, M. Ouyang, T. Raether, T. Grafe, B. McDonald, P. Knauf, Polymeric nanofibers in air filtration applications, Adv. Filtr. Sep. Technol. 15 (2002) 500-524.

[II.29] G.A. Jablonski, F.W.A.H. Geurts, A. Sacco Jr, Carbon deposition over Fe, Ni, and Co foils from CO-H_2-CH_4-CO_2-H_2O, CO-CO_2, CH_4-H_2, and CO-H_2-H_2O gas mixtures: II. Kinetics, Carbon 30 (1992) 99-106.

[II.30] P.A. Tesner, E.Y. Robinovich, I.S. Rafalkes, E.F. Arefieva, Formation of carbon fibers from acetylene, Carbon 8 (1970) 435-440, IN431-IN432, 441-442.

Chapter III Carbon nanofiber synthesis within 3-dimensional sintered nickel microfibrous matrices: Optimization of synthesis conditions

III.1 Abstract

Carbon nanofiber (CNF) synthesis conditions were optimized for growth at both the exterior and the interior of 3-dimensional sintered nickel microfibrous networks. Synthesis of CNF by catalytic decomposition of acetylene (ethyne) was conducted at atmospheric pressure and short reaction times (10 min). Two factors evaluated during their study were: (a) CNF quality (observed by SEM and Raman spectroscopy) and (b) rate of reaction (gravimetrically measured carbon yield). Independent optimization variables included redox faceting pretreatment of nickel, synthesis temperature, and gas composition. Faceting resulted in an 8-fold increase in the carbon yield compared to an untreated substrate. Synthesis with varying levels of hydrogen maximized the carbon yield (9.31 mg C/cm^2 catalyst). The quality of CNF was enhanced via a reduction in amorphous carbon that resulted from the addition of 20% ammonia. Optimized growth conditions that led to high rates of CNF deposition preferentially deposited this carbon at the exterior layer of the nickel microfibrous networks [570˚C, 78% H_2, 20% NH_3, 2% C_2H_2, faceted Ni.]. CNF growth within the 3-dimensional nickel networks was accomplished at conditions selected to lower the gravimetric reaction rate [470˚C, 10% H_2, 88% N_2, 2% C_2H_2 on non-faceted Ni].

III.2 Introduction

Dusting corrosion of metal components in the hydrocarbons processing industry (due to the formation of solid carbon at high temperatures) provided the early impetus for carbon deposition studies in the 1960s. In the 1970s, fibrous carbon structures were extensively investigated under the generic category of 'carbon filaments' using high resolution electron microscopes [III.1-6]. Even though carbon nanotubes (CNT) of 2 nm diameter were observed in 1976 [III.7], these observations did not attract significant attention at the time. The high level of interest in carbon nanofibers (CNF) and CNT in the 1990s resulted from the discovery of buckyballs (C_{60}) in 1985 [III.8] and a better appreciation of nanotubes in 1991 [III.9]. Since that time, extensive research is ongoing involving the synthesis and manipulation of these nanomaterials for a variety of applications including electron field emission [III.10-12], molecular electronics [III.13-19] and nanocomposites [III.20-22], etc.

Nickel, cobalt and iron have been used as active catalysts for CNF/CNT synthesis since the 1970s. It is often reported that the catalyst size determines the diameter of the CNT/CNF [III.23, 24]. In order to control the dimensions of the catalyst, CNT have been synthesized on nanoparticles dispersed on a flat support [III.24, 25] or using organometallic precursors in the gas phase at high pressures [III.26-29]. However, CNF/CNT synthesis on bulk metal substrates is challenging because the exact dimensions of the catalyst cannot be controlled, and as a result high levels of amorphous carbon may be formed. Several investigators have reported synthesis of CNF/CNT on bulk stainless steel substrates [III.30-35], however, there are relatively few reports of CNF synthesis on bulk nickel metal substrates such as foams [III.36-38], screens/grids [III.39], and foils [III.40-43]. Pretreatment of the bulk metal has been studied for its affects on CNF/CNT growth. Acid etching has been reported to be advantageous on stainless steel

substrates due to an increase in surface roughness [III.44, 45]. Kukovitsky et al. synthesized CNF using polyethylene on nickel foils after mechanical and chemical polishing pretreatments [III.42].

This study was undertaken to understand the effects of CNF/CNT synthesis conditions on 3-dimensional high surface area sintered nickel microfibrous substrates. Fig. III-1 shows a sintered nickel microfibrous matrix made with 4 μm (dia.) nickel fibers. The unique challenge for CNF synthesis on sintered metal microfibrous (SMM) matrices stems from their relatively high surface area. The aim of this study was to find whether CNF can be synthesized only on the surface of the SMM matrix, as shown in Fig. III-2 (A), or within the entire 3-dimensional SMM matrix as shown in Fig. III-2 (B). Surface deposition of CNF/CNT on SMM can create a membrane like structure with very small pores, whereas, 3-dimensional deposition within the SMM matrix can provide benefits for other process applications such as liquid or air filtration [III.46]. Variations in the growth layer morphology of CNF were thought to be possible by varying the rate of reaction for CNF deposition. For a SMM matrix acting as a catalyst bed, a high rate of reaction should result in CNF being formed only on the outer layers of the matrix. Whereas, a lower rate of reaction could lead to CNF synthesis within the interior of the SMM matrix. Parameters such as catalyst pretreatment, synthesis temperature and gas composition were selected to optimize these two growth morphologies.

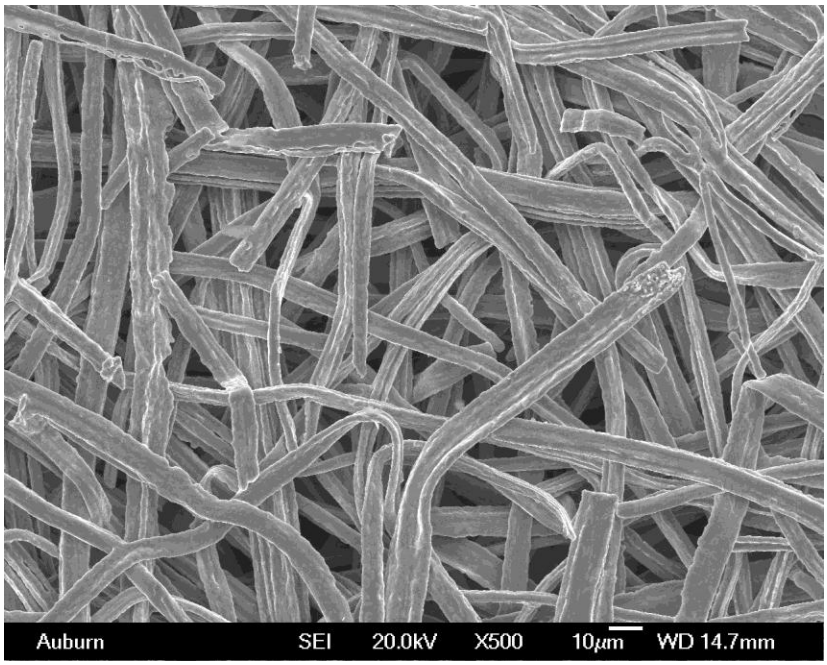

Fig. III-1. SEM image of sintered nickel microfibrous matrix made with 4 μm (dia.) nickel microfibers.

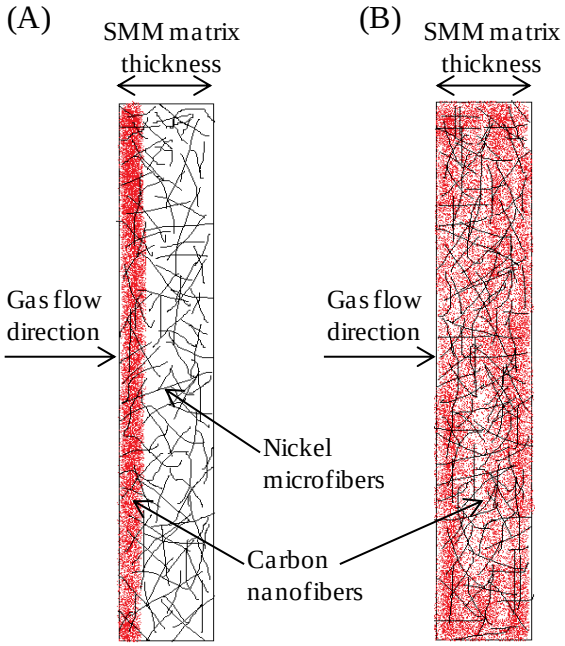

Fig. III-2. Side-view schematic diagram of sintered metal microfibrous (SMM) matrix with: (A) surface synthesis of CNF and (B) 3-dimensional synthesis of CNF.

III.3 Experimental

III.3.1 Materials

Ribbon-shaped nickel microfibers (alloy Ni-200) of metal purity >99% with nominal diameters of 4 μm and 8 μm and lengths of 3 mm and 6 mm, respectively, were obtained from Intramicron Inc. (Auburn, AL). Cold-rolled polycrystalline nickel foil of 99.5% purity (metal basis) and thickness of 0.1 mm was obtained from Alfa Aesar (stock # 44821). High purity nitrogen (99.999%), hydrogen (99.999%), acetylene (99.6%), anhydrous ammonia (99.999%) and breathing quality dry air (<67 ppm moisture) supplied from Airgas Inc. were used without further treatment.

III.3.2 Method

Nickel sintered metal microfibrous (SMM) matrices were prepared by dispersing the nickel microfibers in water using a laboratory mixer and/or blender. The viscosity of water was increased by the addition of 0.75% (w/w) hydroxyethyl cellulose (HEC). The water's increased viscosity and the optimized dispersion methodology prevented excessive reduction in the aspect ratio of nickel microfibers during dispersion. The nickel microfiber dispersions were used to make preforms of the SMM matrices by wet-lay formation using a 16 cm (dia.) TAPPI hand-sheet former. These preforms were sintered for 40 min at a temperature of 950˚C in a reducing environment of 10% hydrogen in nitrogen to form SMM matrices. Samples of the required dimensions were punched out using a steel punch and were compressed to reduce the voidage of SMM matrices. The thickness of the samples used in this study was ~0.36 mm with a voidage of ~76%. The SMM matrices have relatively large surface area because of the microfibers used to make SMM matrices. These SMM matrices were used as the catalysts for the CNF synthesis.

The thermal chemical vapor deposition (CVD) technique of CNF/CNT synthesis was chosen for this study. Thermal CVD allows for gas flow through the SMM matrices during CNF synthesis. In essence, the thermal CVD setup was a high temperature catalytic reactor with the SMM matrix positioned to act as a catalyst packed bed in the reactor (without any bypass). The flow of synthesis gas through the SMM matrix is very important for 3-dimensional synthesis of CNF within the SMM matrix. In order to understand the effects of synthesis conditions on the nickel SMM matrices, it was necessary to remove the factor of high surface area of SMM matrices from the synthesis studies for ease of analyses. This was done by using nickel foil (low surface area nickel catalyst) as a tool to simulate the surface of nickel microfibers within the SMM matrices. The use of nickel foil ensured that there was limited catalyst surface area, which made it possible to analyze the rate of reaction by easy gravimetric measurements.

In this study, the CNF were synthesized using a thermal CVD setup with a quartz tube of 51 mm ID as the reactor in a Lindberg furnace (Model # CF56822C). The flow rates of gases were controlled by Aalborg rotameters. Further details of the thermal CVD setup used have been described elsewhere [III.46]. The nickel foil sample was placed at the center of the reactor with its faces parallel to the direction of flow for equal exposure of gas to both faces of the foil. The sample was supported at two edges by layers of quartz wool. The temperatures inside the reactor were verified prior to experiments using a thermocouple inserted in the position of the sample.

The approach taken to increase the yield of CNF was the thermal redox faceting pretreatment of nickel substrates. Nickel foil was degreased with acetone prior to all experiments. The reactor tube with the sample was inserted in the furnace after the furnace reached the desired temperature. The reactor was kept under nitrogen flow for 15 min before the temperature ramp-up of the reactor and prior to pretreatment or synthesis in order to prevent any

interaction of foil with residual oxygen at high temperatures. For faceting pretreatment, the degreased nickel foil samples (25 mm × 25 mm) with a weight of ~0.65 g were faceted at various temperatures by three cycles of oxidation (using 10% air in nitrogen) and reduction (using 10% hydrogen in nitrogen); each cycle lasted for 11 min. Nitrogen was passed for 1 min between the steps of oxidation (5 min) and reduction (5 min) to avoid the mixture of hydrogen and air at high temperatures. At the end of all pretreatment cycles, the samples were reduced (using 10% hydrogen in nitrogen) for an additional 15 min to bring them to a metallic state. Samples that were not faceted were annealed at 715˚C for 15 min in 10% hydrogen, unless noted otherwise. The reactor was removed from the furnace after faceting/synthesis and cooled to ambient temperature under nitrogen flow. Typical cool down time was ~10 min.

The pretreated samples were used for univariant optimization of CNF synthesis parameters, as shown in Fig. III-3. Redox faceting pretreatment, synthesis temperature, and concentrations of hydrogen and ammonia were the parameters optimized for CNF synthesis. All the optimization studies were performed in absence of post-synthesis purifications such as acid treatment. All the gases required for synthesis except acetylene were passed at desired concentrations through the reactor for 15 min prior to synthesis to ensure that all the catalyst surface-gas interactions were at steady state before the introduction of acetylene. The total flow rate of the synthesis gas was always maintained at 1070 sccm, and the flow of acetylene was kept at 20 sccm (~2%). Synthesis time for all experiments with nickel foil was 10 min unless noted otherwise. All the experiments were performed at atmospheric pressure.

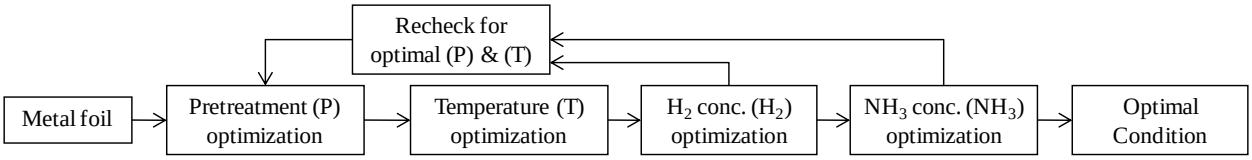

Fig. III-3. Univariant optimization experimental design for CNF synthesis.

III.3.3 Characterization

The yield of carbon on the nickel substrates was determined gravimetrically. The morphology of the carbon deposit was characterized by JEOL 7000-F scanning electron microscopy (SEM). A Renishaw InVia Raman spectrometer, in conjunction with SEM, provided a good estimate of the amount of amorphous carbon in the carbon deposit. The D/G ratio obtained from Raman spectroscopy is the ratio of sp^3 to sp^2 carbon in the sample. All the D/G ratios calculated from Raman spectra were obtained using 514 nm wavelength laser with a high signal-to-noise ratio and baseline correction. The D/G ratios were measured at 1-3 spots per sample with a minimum of 2 samples for each synthesis condition. Raman spectroscopy shows one number of D/G ratio for two characteristics of the carbon deposit. A high D/G ratio can be due to: a) a high fraction of sp^3 carbon in CNF (also known as lattice defects in the graphene sheet) and/or b) a high fraction of amorphous carbon. It is not possible to differentiate between the two distinct characteristics of the carbon deposit using only Raman spectroscopy. Therefore, Raman spectroscopy was used as a secondary characterization technique for carbon deposits. High quality CNF is defined here as CNF with a very low quantity of amorphous carbon byproduct observed by SEM and a low D/G ratio in Raman spectroscopy. Another supplementary characterization technique used was transmission electron microscopy (TEM).

Table III-1. Sequence of CNF synthesis optimization efforts on nickel foil substrates.

Phases		Experimental Details*				Results		
Phase No.	Description of Phase	Substrate Pretreatment	H_2 (%)	NH_3 (%)	T (˚C)	Raman (D/G ratio) (+/- 0.02)	Carbon yield (mg C / g Ni foil) (+/- 6%)	Supporting SEM
1	Effects of substrate pretreatment.	As received	10	0	470	0.96	10	4A & 5A
		Reduction at 715˚C for 15 min				1.06	16	4B & 5B
		Reduction at 815˚C for 120 min				1.04	17	4C & 5C
		Thermal faceting at 515˚C				1.06	21	4D & 5D
		Thermal faceting at 715˚C				1.07	69	4E & 5E
		Thermal faceting at 815˚C				1.14	82	4F & 5F
2	Effects of CNF synthesis temperature. (Following Phase 1)	Thermal faceting at 815˚C	10	0	420	-	3	6A
					470	1.14	82	6B
					520	1.19	102	6C
					570	1.31	44	6D
					670	0.93	2	6E
					770	-	8	6F
3A	Effects of hydrogen concentration. (Following Phase 2)	Thermal faceting at 815˚C	0	0	520	-	5	-
			10			1.19	102	-
			30			0.97	136	-
			98			0.84	150	-
3B	Verify optimal CNF synthesis temperature. (Following Phase 3A)	Thermal faceting at 815˚C	98	0	420	-	0	-
					470	0.75	17	7A
					520	0.84	150	7B
					570	0.9	179	7C
					620	1.11	177	7D
					670	1.49	108	7E
					720	-	3	7F
					770	-	0	-
3C	Verify effects of substrate pretreament. (Following Phase 3A)	Reduction at 715˚C for 15 min	98	0	420	-	0	-
					470	0.64	7	-
					520	0.82	48	-
					570	0.80	123	-
					620	0.97	51	-
					670	1.15	36	-
					720	-	3	-
					770	-	3	-
4A	Effects of ammonia concentration. (Following Phase 3B)	Thermal faceting at 815˚C	98	0	570	0.9	179	8A
			78	20		0.92	164	8B
			48	50		1	154	8C
			18	80		0.99	36	8D
			0	98		-	1	8E
4B	Verify 570˚C is optimal CNF synthesis temperature. (Following Phase 4A)	Thermal faceting at 815˚C	78	20	520	0.77	130	9A
					570	0.92	164	9B
					620	1.14	162	9C
					670	-	9	-
					720	-	2	-
					770	-	4	-
					820	-	3	-
					870	-	2	-
					920	-	3	-
4C	Verify effects of substrate pretreament. (Following Phase 4A)	Reduction at 715˚C for 15 min	78	20	570	-	68	10A
		Thermal faceting at 815˚C				0.92	164	10B.1
		-				-	-	-

*Nitrogen used as inert diluent, and 2 % acetylene for CNF synthesis.

III.4 Results and Discussion

III.4.1 Hydrocarbon for CNF synthesis

It has been reported that unsaturated hydrocarbons undergo rapid catalytic decomposition over transition metals at high temperatures [III.3]. Also, acetylene (ethyne) has been found to decompose faster than alkanes and alkenes [III.3]. Therefore, acetylene was chosen as the carbon source for synthesis because it is the smallest unsaturated hydrocarbon molecule and because examples of successful CNT/CNF synthesis using acetylene abound in the literature.

III.4.2 Effects of pretreatment

Catalyst activity has been shown to increase in the presence of grain boundaries or surface roughness [III.3, 30, 42, 47-49]. From a few preliminary experiments, a synthesis temperature of 470˚C with 10% hydrogen in nitrogen as the carrier gas was found to be the lowest temperature at which the CNF could be synthesized on nickel foil. The different pretreatment conditions tested and their effects on the carbon yield are shown in Table III-1 (Phase1) for CNF synthesis at 470˚C. The “as received” nickel foil had the least carbon yield after synthesis. This low carbon yield could be due to the oxide layer on the “as received” nickel foil catalyst, which suppressed the formation of carbon product [III.37, 50, 51]. It has been reported that reduction of the catalyst before synthesis increases the carbon yield [III.30, 37, 47, 52]. The increase in carbon yield after reduction of the catalyst was also observed in this study, as shown in Table III-1 (Phase 1). The samples reduced at 715˚C for 15 min and 815˚C for 120 min (using 10% hydrogen) had similar carbon yields (Table III-1 (Phase 1)), similar morphology of the carbon deposit, and similar D/G ratios in Raman spectroscopy (Table III-1 (Phase 1)). It was thus deduced that reduction at 715˚C for 15 min was sufficient to remove the oxide layer of the “as received” foil. Nanoparticles were not formed (as observed by SEM) after the reduction

of nickel foil at high temperatures, which is unlike the observations reported by Jeong et al. [III.25]. The carbon yield increased with the increase in the redox faceting temperature (Table III-1 (Phase 1)). The maximum carbon yield was 82 mg/(g of foil) for the 815˚C faceted sample at a synthesis temperature of 470˚C with 2% acetylene, 10% hydrogen and 88% nitrogen.

The yield of carbon for each pretreatment condition in Table III-1 (Phase 1) can be correlated to the SEM images of the pretreated samples shown in Fig. III-4. The faceting pretreatment added grain boundaries to the foil and increased the carbon yield. The number of grain boundaries increased progressively with the faceting pretreatment temperature. Distinct facets and maximum grain boundaries were observed for the 815˚C faceted sample, which also had the maximum yield as shown in Table III-1 (Phase 1).

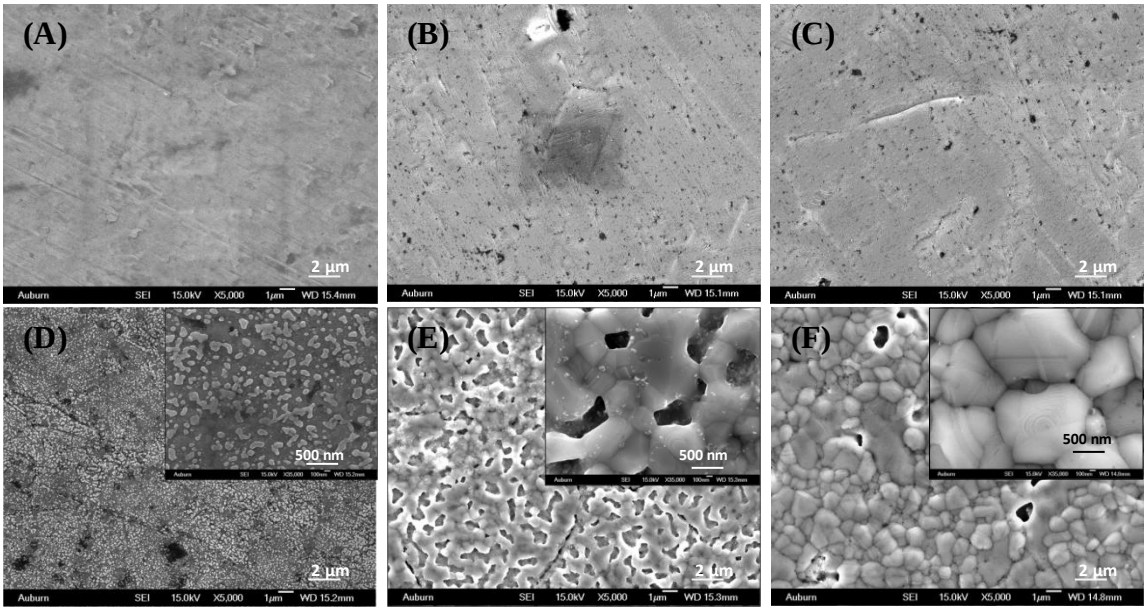

Fig. III-4. Effects of pretreatment on nickel foil: (A) as received, (B) reduced at 715˚C for 15 min, (C) reduced at 815˚C for 120 min, (D) thermal faceting at 515˚C, (E) thermal faceting at 715˚C, and (F) thermal faceting at 815˚C. (Table III-1 (Phase 1))

The SEM images of synthesized CNF on pretreated foil are shown in Fig. III-5. As expected, the CNF in the deposit had variations in diameter because the catalyst particle size could not be controlled. The deposit on the "as received" foil had less amorphous carbon. The synthesis on samples reduced at 715˚C and 815˚C had some amorphous carbon associated with it. After faceting pretreatment, the amorphous content of the deposit increased and was maximized for samples faceted at 815˚C (Fig. III-5 (F)). The high amorphous content on 815˚C faceted foil was also seen by Raman spectroscopy in the form of the highest D/G ratio (Table III-1 (Phase 1)).

It was found that a synthesis temperature of 470˚C with 10% hydrogen in nitrogen as the carrier gas gave the least rate of reaction with formation of CNF and limited amorphous carbon for "as received" and reduced nickel foil samples. This synthesis condition was taken as the optimal condition for the minimum rate of reaction for 3-dimensional deposition of CNF within the SMM matrix. For a high rate of reaction, of all the pretreatment conditions tested, the 815˚C faceting pretreatment was taken to be the optimal pretreatment condition for maximizing the carbon yield. Also, the optimal faceting pretreatment condition (faceting at 815˚C) did not change with the temperatures and gas compositions used for CNF synthesis. As seen in Fig. III-5 (F), the quality of CNF for the 815˚C faceted sample was worst among all the samples tested. Further studies on 815˚C faceted nickel foil were pursued in an attempt to enhance the yield and quality of CNF.

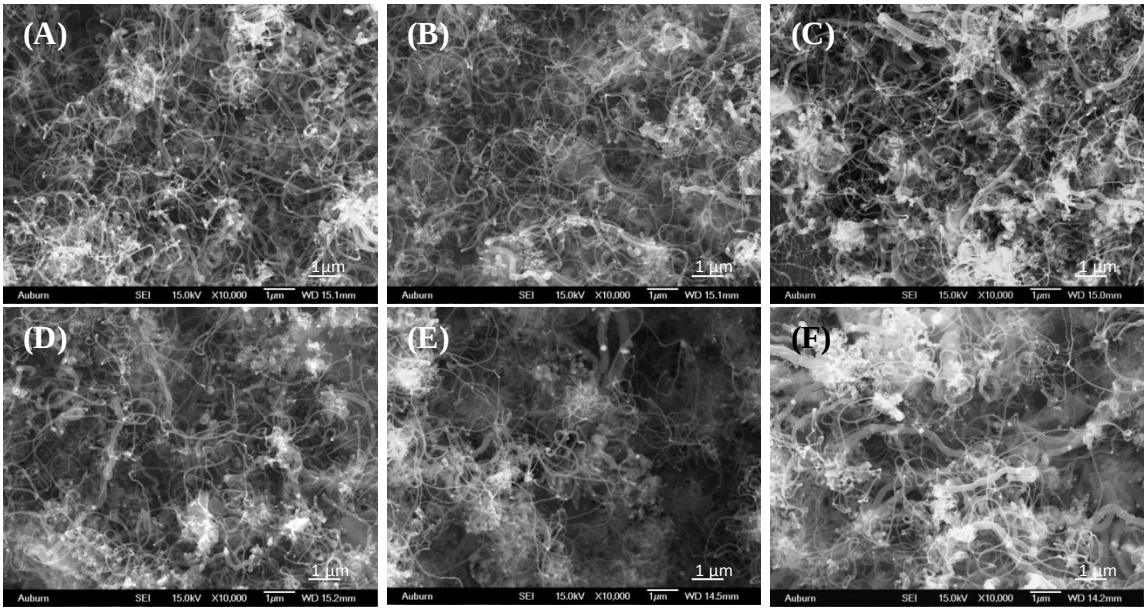

Fig. III-5. Synthesized CNF for effects of pretreatment on foil: (A) as received, (B) reduced at 715˚C for 15 min, (C) reduced at 815˚C for 120 min, (D) thermal faceting at 515˚C, (E) thermal faceting at 715˚C, and (F) thermal faceting at 815˚C. Synthesis conditions: 2% C_2H_2, 10% H_2, 88% N_2 and 470˚C. (Table III-1 (Phase 1))

III.4.3 Effects of synthesis temperature

After optimizing the pretreatment of foil to faceting at 815˚C for a high carbon yield, the effect of temperature on synthesis was studied to further increase the yield and quality of CNF. As shown in Table III-1 (Phase 2), the synthesis temperature for maximum carbon yield was 520˚C. At a synthesis temperature of 570˚C, the carbon deposit contained only large diameter CNF of the order of 300-600 nm (dia.) as shown in Fig. III-6 (D). That sample had a very high D/G ratio (Table III-1 (Phase 2)**)** in Raman spectroscopy, which indicated high sp^3 carbon fraction within the CNF. There were no CNF observed for synthesis temperatures of 420˚C, 670˚C and 770˚C. The temperature of 520˚C was chosen for further experiments due to its high carbon yield.

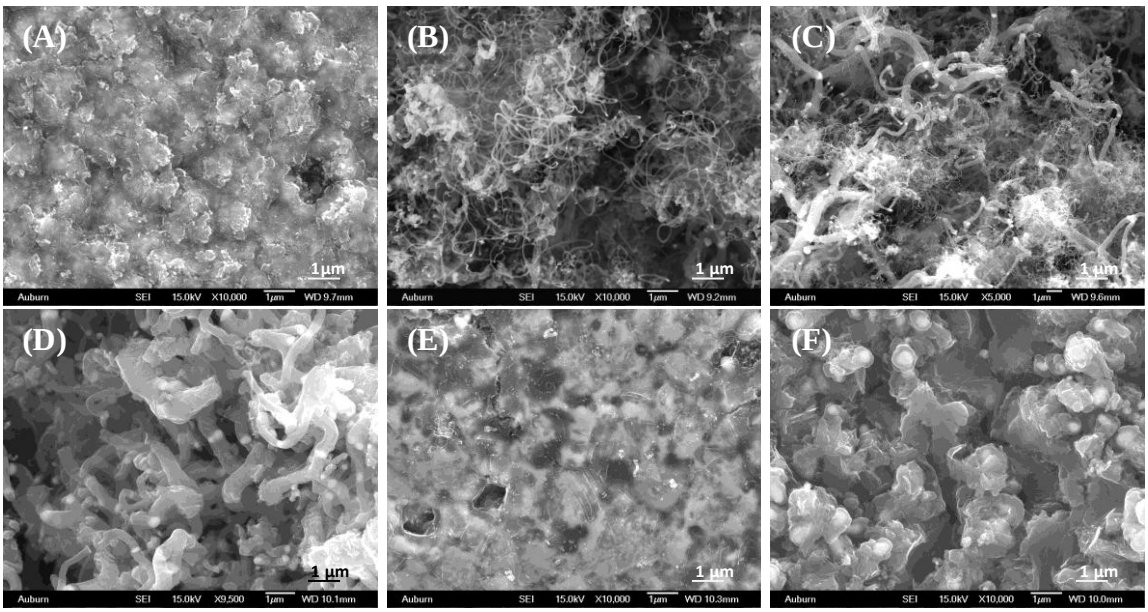

Fig. III-6. CNF growth in 10% H_2 (2% C_2H_2, 88% N_2). Temperature: (A) 420˚C, (B) 470˚C, (C) 520˚C, (D) 570˚C, (E) 670˚C and (F) 770˚C. Sample faceted at 815˚C. (Table III-1 (Phase 2))

III.4.4 Effects of hydrogen in synthesis gas

The effects of varying hydrogen concentration were studied to enhance the yield and quality of CNF. Hydrogen gas increases the carbon yield [III.30, 50, 52, 53] and keeps the catalyst active [III.54] during CNF synthesis by avoiding carbon encapsulation of the catalyst surface [III.52, 55]. A higher yield of carbon above 450˚C due to the presence of hydrogen has been reported in the kinetic studies of acetylene decomposition over nickel foil [III.50] and nichrome wire [III.5]. It has been reported that low concentrations of hydrogen can promote the formation of CNF on the catalyst, while high concentrations of hydrogen can be inhibitory to the formation of CNF [III.30, 54]. One reason stated is that a very high concentrations of hydrogen can rapidly remove the carbon from the catalyst surface, preventing CNF/CNT formation, while very low concentrations of hydrogen may lead to catalyst deactivation due to pyrolytic carbon buildup [III.30]. However, the effect of hydrogen may depend on the temperature of synthesis.

At high temperatures (>700˚C), excess hydrogen has been reported to have a negative effect [III.36] as compared to the typical positive effect reported in the literature at lower temperatures (<600˚C) mentioned above. It should be noted that at any temperature, synthesis with hydrogen in the synthesis gas will yield more carbon for a nickel catalyst as compared to synthesis in absence of hydrogen since hydrogen is required to keep the catalyst active [III.53]. It has been shown that the rate of carbon synthesis increases with an increase in concentration of hydrogen in the acetylene-hydrogen system at 608˚C for a bulk nickel metal catalyst [III.53]. These synthesis parameters were very similar to the parameters used in this study.

For the temperature range of interest (470˚C-620˚C), the increase in the concentration of hydrogen was expected to increase the carbon yield. This is shown in Table III-1 (Phase 3A) for the synthesis temperature of 520˚C. The maximum yield of carbon was found at 98% hydrogen in synthesis gas. Following the univariant experimental design (Fig. III-3), experiments were carried out to verify whether the optimum temperature of synthesis in 98% hydrogen environment remained at 520˚C. The yield of carbon for 98% hydrogen synthesis at various temperatures is shown in Table III-1 (Phase 3B). The temperature of maximum carbon yield changed from 520˚C to 570˚C with the change of hydrogen concentration from 10% to 98%. This was attributed to the change in the activity of the catalyst for higher concentrations of hydrogen.

The decrease in D/G ratio of Raman spectroscopy for 98% hydrogen synthesis (Table III-1 (Phase 3B)) as compared to 10% hydrogen synthesis (Table III-1 (Phase 2)) showed that the fraction of sp^3 carbon in CNF and/or amorphous carbon was reduced for the 570˚C synthesis. The SEM images (Fig. III-7) showed that the least amount of amorphous carbon was present in the sample synthesized at 570˚C which also had the maximum carbon yield (Table III-1 (Phase

3B)). Out of all the conditions tested in this study, the 570˚C synthesis with 98% hydrogen on 815˚C faceted nickel foil resulted in maximum carbon yield. However, the carbon yield may have been limited by the supply of acetylene rather than the catalytic activity of the foil. The face velocity of gas within the reactor at 570˚C reaction temperature was 22 mm/s and the 25 mm × 25 mm sample was placed at the center of 51 mm diameter reactor with faces parallel to the direction of flow. The void space of the reactor near the foil may have caused bypassing of gas, resulting in limited carbon yield on nickel foil. It is interesting to note that the 670˚C synthesis (Fig. III-7 (E)) had distinct CNF with little amorphous carbon as seen in the SEM images, but it had a very high D/G ratio in Raman spectroscopy (Table III-1 (Phase 3B)). It can be concluded that the sp^3 carbon within the CNF was very high with little or no amorphous carbon for the 670˚C synthesis.

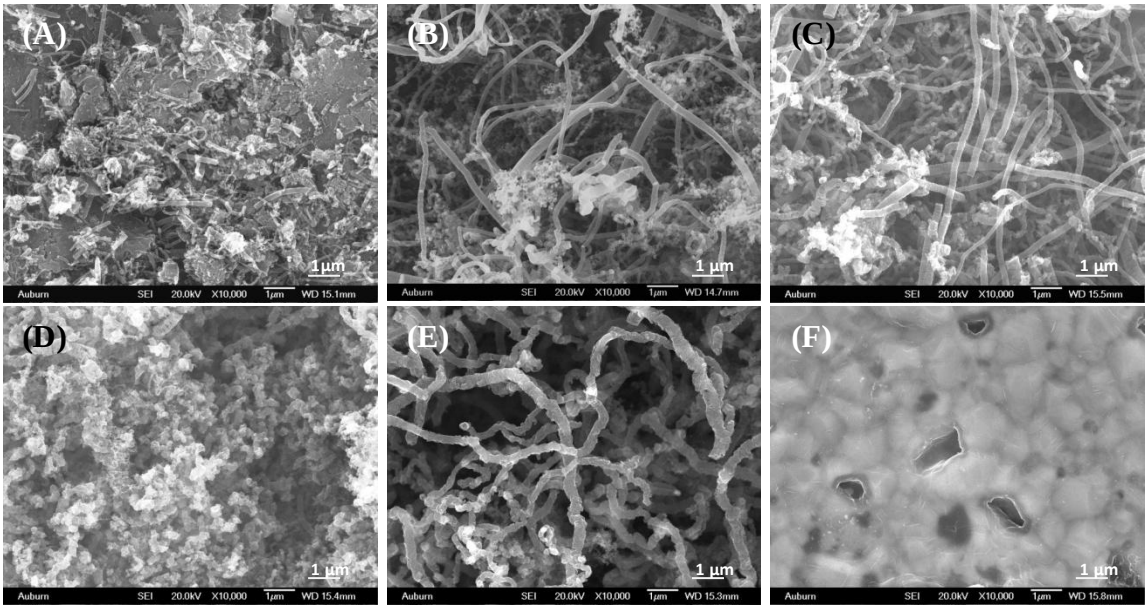

Fig. III-7. CNF growth in 98% H_2 (2% C_2H_2). Temperature: (A) 470˚C, (B) 520˚C, (C) 570˚C, (D) 620˚C, (E) 670˚C and (F) 720˚C. Sample faceted at 815˚C. (Table III-1 (Phase 3B))

Following the univariant experimental design (Fig. III-3), similar temperature optimization experiments were carried out for 715˚C reduced foil (non-faceted) to ensure that faceting was indeed an important independent variable which affected the yield of carbon and it was not overshadowed by the increase in yield due to the high fraction of hydrogen (98%). The carbon yields on the 715˚C reduced foil at various temperatures with 98% hydrogen are shown in Table III-1 (Phase 3C). The maximum yield for these non-faceted samples was also found to be at a temperature of 570˚C. However, comparing the carbon yield in Table III-1 (Phase 3B) and (Phase 3C), the yield of the 815˚C faceted sample was 46% higher than that of the 715˚C reduced sample. This proved that faceting pretreatment was an independent parameter for enhancement of carbon yield. As there was less amorphous carbon and maximum carbon yield for CNF synthesized at 570˚C on 815˚C faceted foil with 2% acetylene and 98% hydrogen, it was taken as the optimal synthesis condition for further studies.

III.4.5 Effects of ammonia in synthesis gas

Ammonia pretreatment [III.56-58] and synthesis in an ammonia environment [III.59-61] has been investigated by a few researchers for the synthesis of aligned CNF/CNT. It has been proposed that ammonia helps in the formation of a high density of nucleation sites on the catalyst for CNF/CNT synthesis and prevents catalyst passivation by removing amorphous carbon in the initial stages of synthesis [III.23, 56]. Also, researchers have shown that ammonia can keep the catalyst active resulting in higher carbon yield as compared to synthesis with hydrogen at temperatures above 750˚C [III.56, 62, 63]. Some researchers have proposed that atomic hydrogen [III.56] and/or atomic nitrogen [III.63] produced by catalytic decomposition of ammonia keeps the catalyst active at high temperatures for the synthesis of aligned CNF. Also, there are conflicting observations for the need of ammonia during the synthesis of aligned CNF

with some researchers proposing that ammonia is required only for the initial stage of synthesis [III.23], whereas others are proposing that ammonia is required during synthesis [III.56, 61, 64]. There are very few reports of aligned CNF on bulk nickel metal either with [III.60] or without ammonia [III.65]. However, these researchers used plasma enhanced CVD at low pressures of 1-20 torr. Bower et al. reported that plasma enhanced CVD technique is the reason for the alignment since the ferromagnetic catalysts such as nickel, cobalt or iron are oriented due to the electric field [III.66]. Therefore, it was not clear whether ammonia or the synthesis technique was responsible for the alignment. In this study, attempts were made to align CNF on faceted nickel foil using ammonia using thermal CVD technique at atmospheric pressures.

Varying the ammonia concentration in synthesis gas between 0% and 98% had no discernible effect on the orientation of CNF. The carbon yields for various concentrations of ammonia in synthesis gas at a 570˚C synthesis temperature are shown in Table III-1 (Phase 4A). As the ammonia concentration increased, the yield of carbon progressively decreased. At 20% ammonia, the amorphous carbon in the deposit decreased significantly (Fig. III-8 (B)). Fig. III-8 (C), (D) and (E) show the degradation of quality of the carbon deposit for ammonia concentrations greater than 20%. Therefore, 20% ammonia in synthesis gas was the optimum condition for the least amount of amorphous carbon with a high carbon yield at 570˚C. The high D/G ratio in Table III-1 (Phase 4A) also indicated the degeneration of quality of the carbon deposit for ammonia concentrations greater than 20%.

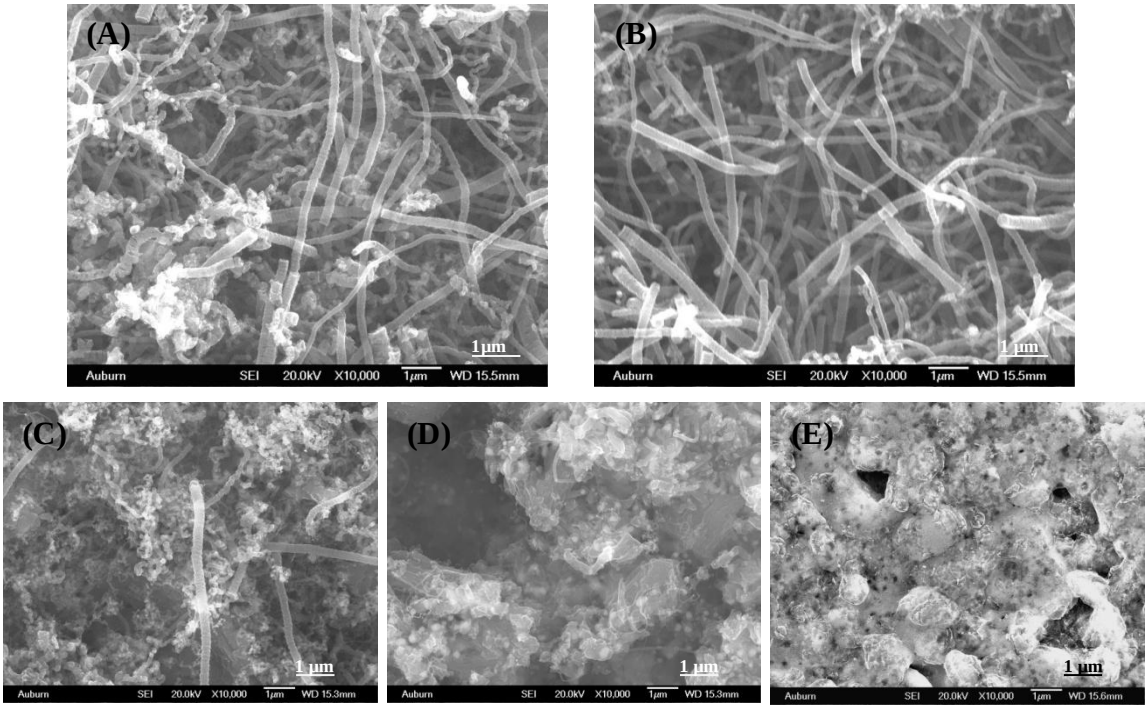

Fig. III-8. Synthesized CNF for effects of NH_3 during synthesis on 815˚C faceted foil. NH_3 concentration: (A) 0%, (B) 20%, (C) 50%, (D) 80% and (E) 98%. Synthesis conditions: 570˚C, 2% C_2H_2 and remainder H_2. (Table III-1 (Phase 4A))

Few researchers have used ammonia at high temperatures (>700˚C) for the alignment of CNF/CNT using the thermal CVD technique on different catalyst configurations [III.23, 56, 67]. Therefore, a synthesis temperatures range of 520 -920˚C was probed with 20% ammonia as shown in Table III-1 (Phase 4B). There was no improvement in alignment or carbon yield at temperatures higher than 570˚C and the nickel foil became catalytically inactive at temperatures greater than 670˚C. Solid carbon deposits were found on the walls of the reactor above 800˚C. This was attributed to the high rate of self-decomposition of acetylene above 700˚C [III.68]. Following the univariant optimization experimental design (Fig. III-3), Table III-1 (Phase 4B) shows that the temperature of maximum carbon yield remained at 570˚C after the addition of

20% ammonia in synthesis gas. Also, the SEM images (Fig. III-9) showed that the synthesis temperature for best morphology of the carbon deposit remained at 570˚C.

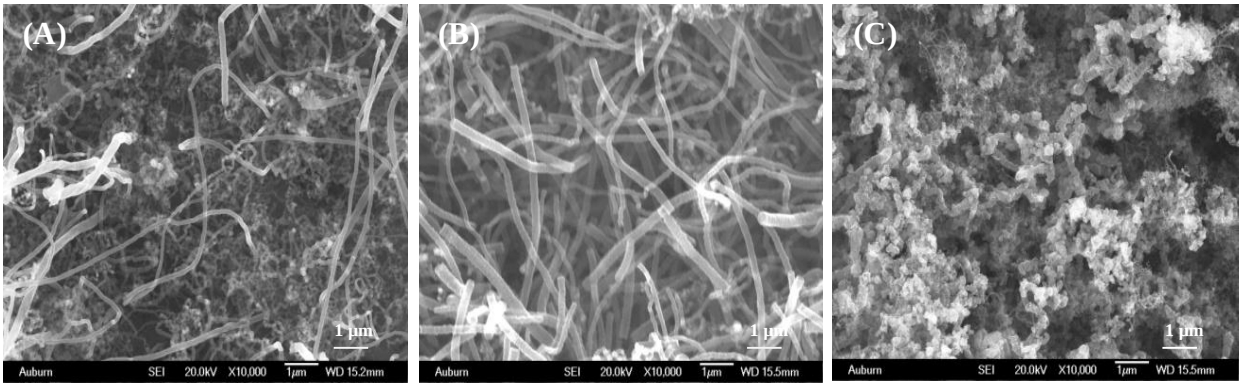

Fig. III-9. Synthesized CNF for effect of synthesis temperature on 815˚C faceted foil. Temperature: (A) 520˚C, (B) 570˚C and (C) 620˚C. Synthesis gas: 2% C_2H_2, 20% NH_3 and 78% H_2. (Table III-1 (Phase 4B))

Following the univariant optimization experimental design (Fig. III-3), CNF synthesis was done on both faceted foil and non-faceted foil to verify that the faceting pretreatment gave the best yield and quality of CNF. As shown in Fig. III-10, the morphology of the deposit for 815˚C faceted foil (Fig. III-10 (B)) was better than that for 715˚C annealed foil (Fig. III-10 (A)) for the same synthesis temperature. Although ammonia did not assist in CNF orientation, it reduced the amorphous carbon of the deposit for faceted samples. Fig. III-10 (B.2) shows the TEM image of CNF synthesized on faceted samples at optimal conditions (20% ammonia). This shows that the CNF are made from stacks of carbon blocks. These carbon blocks probably have "platelet" orientation of graphene sheets as they were not hollow in the center. For high yield and quality of CNF, the optimal synthesis condition was found to be 20% ammonia, 78% hydrogen and 2% acetylene at a 570˚C synthesis temperature. This synthesis condition was taken as the

optimal condition for a high rate of reaction for surface deposition of CNF on the nickel microfibrous matrices.

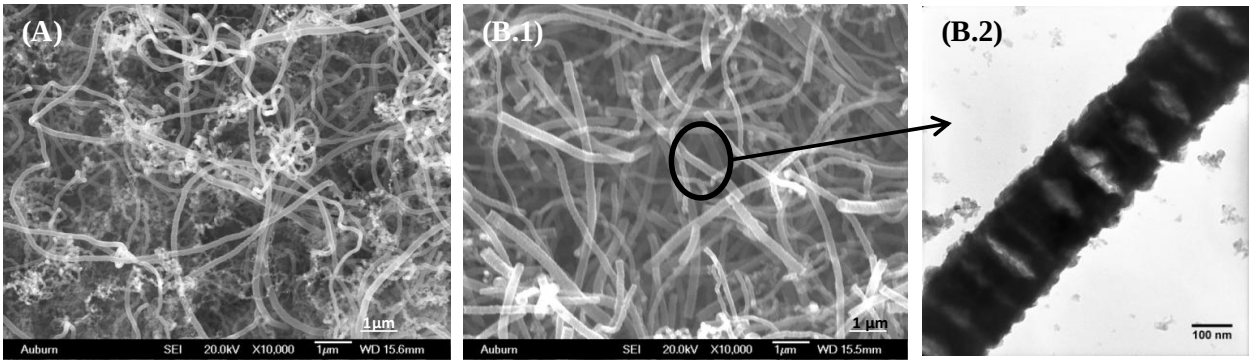

Fig. III-10. Synthesized CNF for effect of 20% NH_3 on different pretreated foils: (A) SEM of CNF on 715˚C reduction pretreatment, (B.1) SEM of CNF on 815˚C faceting pretreatment, and (B.2) TEM of B.1. Synthesis conditions: 2% C_2H_2, 20% NH_3,78% H_2 and 570˚C. (Table III-1 (Phase 4C))

III.4.6 Mechanism of CNF synthesis

The basic steps in the mechanism of CNF/CNT synthesis involve adsorption and catalytic decomposition of hydrocarbon gas to yield atomic carbon on the catalyst surface. The carbon atoms are transported to active catalyst sites by surface diffusion [III.1] and/or bulk diffusion [III.55], where the synthesis occurs. The rate determining step for CNF synthesis is reported to be the diffusion of carbon through/over the catalyst [III.50, 52, 55]. Typically three periods are observed in the synthesis of CNF: (a) incubation period, (b) constant synthesis rate period and (c) tailing off period [III.50, 52]. Finally, the reaction stops because of catalyst poisoning due to deviation from the reaction equilibrium which coats the catalyst particle with a carbon layer [III.52, 55]. The incubation period at atmospheric pressures is not significant for acetylene decomposition on nickel [III.3]. In this study, all experiments were performed in the constant synthesis rate period as observed in Fig. III-11 for faceted and non-faceted foil. The experimental

errors involved in this study prevented detection of an incubation period of synthesis. Also, a tail off period was not observed due to the short synthesis times (10-15 min).

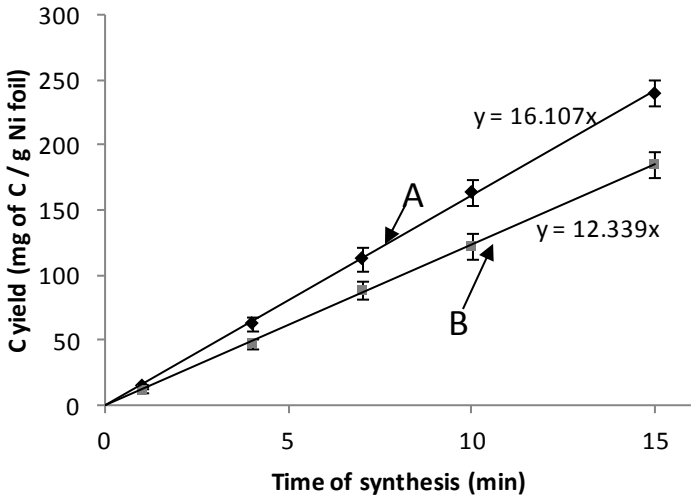

Fig. III-11. Yield of carbon versus time. (A) 815˚C faceted foil; 2% C_2H_2, 20% NH_3,78% H_2 and 570˚C. (B) 715˚C reduced foil; 2% C_2H_2, 98% H_2 and 570˚C.

Formation of small catalyst crystallites is necessary for the synthesis of CNF, as they are known to be the source of CNF growth. These crystallites are formed during the incubation period of the synthesis process. The faceting pretreatment optimized in this study added grain boundaries to the nickel catalyst. It has been previously reported that the grain boundaries on bulk metals act as nucleation sites [III.3, 47] due to local changes in topography and/or effect of local impurities [III.69]. Also, grain boundaries provide a fast path for mass transport [III.39]. The enhanced mass transport into faceted nickel foil accelerated the formation of crystallites, which resulted in the increase in the carbon yield.

Figueiredo et al. reported that hydrogen does not affect the CNF synthesis on supported nickel catalyst, but it affects synthesis on bulk nickel metal by helping in initial crystallite formation and enhancing the process of nucleation of carbon at the grain boundaries [III.2]. The

higher carbon yield on foil for higher hydrogen concentrations may have been due to the combination of accelerated crystallite formation [III.2] and maintaining the nickel catalyst activity [III.52, 55, 70]. Ammonia decomposes over the nickel catalyst at experimental conditions close to those used in this study [III.71]. Also, Shalagina et al. concluded that ammonia in synthesis gas significantly changed the CNF morphology and the quantity of nitrogen in CNF [III.72]. We hypothesize that the endothermic decomposition of ammonia may change the catalyst characteristics for the exothermic acetylene decomposition during CNF synthesis. It has also been proposed by other researchers that there is an effect on the synthesis product due to atomic hydrogen [III.56] and/or atomic nitrogen [III.63] produced by the decomposition of ammonia. These contributing factors may have modified the morphology of carbon deposits due to ammonia addition in the synthesis gas. However, the role of ammonia during CNF growth is not very well understood and requires further investigation.

III.4.7 Synthesis of CNF within sintered metal microfibrous (SMM) matrices

Optimization of CNF synthesis on nickel foil was studied with the aim of finding the synthesis conditions for 3-dimensional (low rate of reaction) and surface (high rate of reaction) deposition of CNF within the SMM matrices. Fig. III-12 shows the SEM images of the 3-dimensional deposition of CNF within the SMM matrix using the synthesis conditions optimized in this study for a low rate of reaction. Fig. III-12 (A) and (B) show the SEM images of SMM matrix before and after an 11 min synthesis, respectively [III.46]. Fig. III-12 (C.1), (C.2) and (C.3) show that the CNF are uniformly deposited throughout the thickness of the SMM matrix [III.46]. These matrices with 3-dimensional deposition of CNF have shown enhancement in air filtration performance due to CNF synthesis [III.46]. Fig. III-13 shows the SEM images of surface deposition of CNF on the SMM matrix using synthesis conditions optimized in this study

for a high rate of reaction. Fig. III-13 (A) and (B.1) show the SMM matrix before and after the redox faceting pretreatment. Fig. III-13 (C.1) shows the cross-sectional view of SMM matrix after an 11 min synthesis of CNF. Fig. III-13 (C.2) and (C.3) clearly show that the CNF are densely synthesized only on the surface of the SMM matrix and the CNF are not synthesized throughout the thickness of the SMM matrix. Fig. III-12 corresponds to the schematic diagram Fig. III-2 (B) and Fig. III-13 corresponds to Fig. III-2 (A).

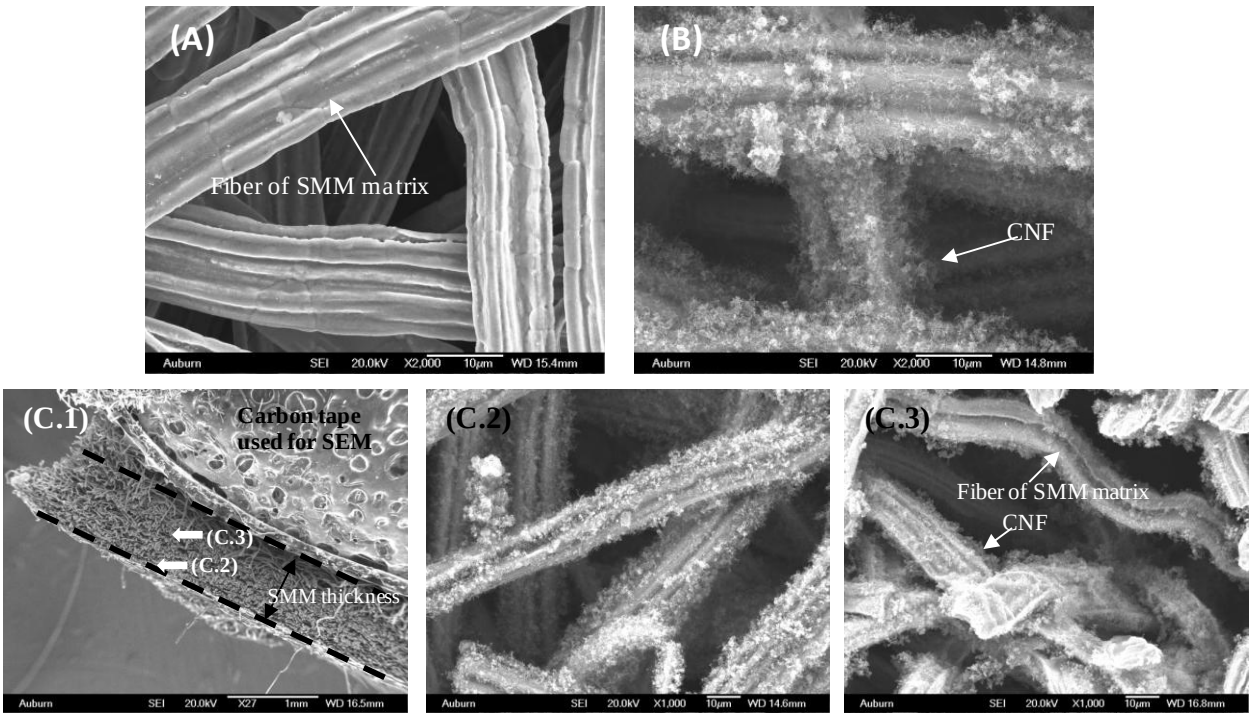

Fig. III-12. 3-dimensional deposition of CNF within 8 μm SMM matrix: (A) top-view before synthesis, (B) top-view after CNF 11 min synthesis, (C.1) low magnification (27X) cross-sectional view, (C.2) cross-sectional view at 1000X of the matrix edge shown in C.1, and (C.3) cross-sectional view at 1000X of the matrix thickness centerline shown in C.1 [III.46].

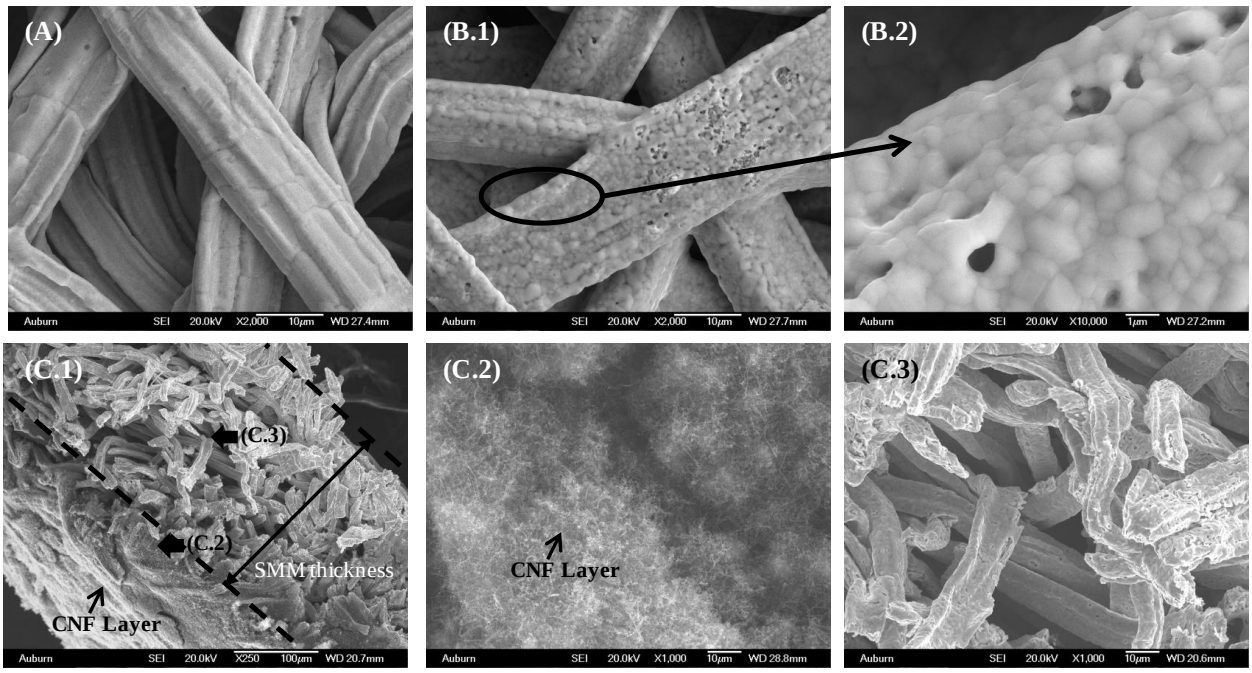

Fig. III-13. Surface deposition of CNF on 8 μm SMM matrix: (A) SMM matrix, (B.1) faceted SMM matrix, (B.2) high magnification (10000X) of faceted SMM matrix, (C.1) cross-sectional view at 250X, (C.2) cross-sectional view at 1000X of the surface shown in C.1, and (C.3) cross-sectional view at 1000X of the matrix thickness centerline shown in C.1.

III.5 Conclusion

Carbon nanofiber synthesis on sintered nickel microfibrous substrates was optimized for two different reaction conditions: (a) high rates of reaction for surface synthesis of carbon nanofibers (CNF) and (b) low rates of reaction for uniform 3-dimensional synthesis of CNF within nickel sintered metal microfibrous (SMM) matrices. Univariant optimization was used in this study. Factors considered during optimization were the rate of reaction and the quality of CNF produced. Redox faceting pretreatment, synthesis temperature, hydrogen concentration and ammonia concentration were the parameters optimized. During the optimization for high rates of reaction, it was found that redox faceting pretreatment introduced additional grain boundaries and increased the catalytic activity of the nickel substrate resulting in an 8-fold increase in the

carbon yield. In the temperature range from 470˚C to 670˚C, carbon yield increased with increase in the concentration of hydrogen. Ammonia (20%) in the synthesis gas reduced the quantity of amorphous carbon.

For surface deposition of CNF on SMM matrices (which requires a high rate of reaction), the optimum synthesis condition were: 570˚C, 78% hydrogen, 20% ammonia and 2% acetylene on 815˚C faceted nickel. For 3-dimensional deposition of CNF within SMM matrices (which requires a low rate of reaction), the optimum synthesis condition were: 470˚C, 10% hydrogen, 88% nitrogen and 2% acetylene on non-faceted nickel.

III.6 References

[III.1] T. Baird, J.R. Fryer, B. Grant, Carbon formation on iron and nickel foils by hydrocarbon pyrolysis. Reactions at 700˚C, Carbon, 12 (1974) 591-602.

[III.2] J.L. Figueiredo, D.L. Trimm, Carbon formation on unsupported and supported nickel catalysts, J. Appl. Chem. Biotechnol., 28 (1978) 611-616.

[III.3] L.S. Lobo, D.L. Trimm, Carbon formation from light hydrocarbons on nickel, J. Catal., 29 (1973) 15-19.

[III.4] L.S. Lobo, D.L. Trimm, Studies of carbon formation on metals using a vacuum microobalance, Progr. Vac. Microbalance Tech., 2 (1973) 1-8.

[III.5] P.A. Tesner, E.Y. Robinovich, I.S. Rafal'kes, E.F. Aref'eva, Formation of carbon fibers from acetylene, Carbon, 8 (1970) 433-442.

[III.6] Y. Nishiyama, Y. Tamai, Carbon formation on copper-nickel alloys from benzene, J. Catal., 33 (1974) 98-107.

[III.7] A. Oberlin, M. Endo, T. Koyama, Filamentous growth of carbon through benzene decomposition, J. Cryst. Growth, 32 (1976) 335-349.

[III.8] H.W. Kroto, J.R. Heath, S.C. O'Brien, R.F. Curl, R.E. Smalley, C60: buckminsterfullerene, Nature, 318 (1985) 162-163.

[III.9] S. Iijima, Helical microtubules of graphitic carbon, Nature, 354 (1991) 56-58.

[III.10] L.A. Chernozatonskii, E.F. Kukovitskii, A.L. Musatov, A.B. Ormont, K.R. Izraeliants, S.G. L'Vov, Carbon crooked nanotube layers of polyethylene: synthesis, structure and electron emission, Carbon, 36 (1998) 713-715.

[III.11] A.L. Musatov, N.A. Kiselev, D.N. Zakharov, E.F. Kukovitskii, A.I. Zhbanov, K.R. Izrael'yants, E.G. Chirkova, Field electron emission from nanotube carbon layers grown by CVD process, Appl. Surf. Sci., 183 (2001) 111-119.

[III.12] Y. Saito, K. Hata, A. Takakura, J. Yotani, S. Uemura, Field emission of carbon nanotubes and its application as electron sources of ultra-high luminance light-source devices, Physica B, 323 (2002) 30-37.

[III.13] P. Avouris, R. Martel, V. Derycke, J. Appenzeller, Carbon nanotube transistors and logic circuits, Physica B, 323 (2002) 6-14.

[III.14] P.G. Collins, M.S. Arnold, P. Avouris, Engineering carbon nanotubes and nanotube circuits using electrical breakdown, Science, 292 (2001) 706-709.

[III.15] A. Bachtold, P. Hadley, T. Nakanishi, C. Dekker, Logic circuits with carbon nanotube transistors, Science, 294 (2001) 1317-1320.

[III.16] V. Derycke, R. Martel, J. Appenzeller, P. Avouris, Carbon Nanotube Inter- and Intramolecular Logic Gates, Nano Lett., 1 (2001) 453-456.

[III.17] C. Zhou, J. Kong, E. Yenilmez, H. Dai, Modulated chemical doping of individual carbon nanotubes, Science, 290 (2000) 1552-1555.

[III.18] P. Sharma, P. Ahuja, Recent advances in carbon nanotube-based electronics, Mater. Res. Bull., 43 (2008) 2517-2526.

[III.19] A.P. Graham, G.S. Duesberg, W. Hoenlein, F. Kreupl, M. Liebau, R. Martin, B. Rajasekharan, W. Pamler, R. Seidel, W. Steinhoegl, E. Unger, How do carbon nanotubes fit into the semiconductor roadmap?, Appl. Phys. A: Mater. Sci. Process., 80 (2005) 1141-1151.

[III.20] A.R. Bhattacharyya, T.V. Sreekumar, T. Liu, S. Kumar, L.M. Ericson, R.H. Hauge, R.E. Smalley, Crystallization and orientation studies in polypropylene/single wall carbon nanotube composite, Polymer, 44 (2003) 2373-2377.

[III.21] M.J. Biercuk, M.C. Llaguno, M. Radosavljevic, J.K. Hyun, A.T. Johnson, J.E. Fischer, Carbon nanotube composites for thermal management, Appl. Phys. Lett., 80 (2002) 2767-2769.

[III.22] M. Cadek, J.N. Coleman, V. Barron, K. Hedicke, W.J. Blau, Morphological and mechanical properties of carbon-nanotube-reinforced semicrystalline and amorphous polymer composites, Appl. Phys. Lett., 81 (2002) 5123-5125.

[III.23] Y.-T. Jang, J.-H. Ahn, Y.-H. Lee, B.-K. Ju, Effect of NH3 and thickness of catalyst on growth of carbon nanotubes using thermal chemical vapor deposition, Chem. Phys. Lett., 372 (2003) 745-749.

[III.24] W.Z. Li, D.Z. Wang, S.X. Yang, J.G. Wen, Z.F. Ren, Controlled growth of carbon nanotubes on graphite foil by chemical vapor deposition, Chem. Phys. Lett., 335 (2001) 141-149.

[III.25] N.-J. Jeong, J.-H. Lee, Y.-H. Kim, J.-H. Kim, H.-Y. Kim, High-density growth of carbon nanotubes with catalytic sites activated on nickel substrate, Res. Chem. Intermed., 34 (2008) 761-766.

[III.26] P. Nikolaev, M.J. Bronikowski, R.K. Bradley, F. Rohmund, D.T. Colbert, K.A. Smith, R.E. Smalley, Gas-phase catalytic growth of single-walled carbon nanotubes from carbon monoxide, Chem. Phys. Lett., 313 (1999) 91-97.

[III.27] M.J. Bronikowski, P.A. Willis, D.T. Colbert, K.A. Smith, R.E. Smalley, Gas-phase production of carbon single-walled nanotubes from carbon monoxide via the HiPco process: A parametric study, J. Vac. Sci. Technol., A, 19 (2001) 1800-1805.

[III.28] B.C. Satishkumar, A. Govindaraj, R. Sen, C.N.R. Rao, Single-walled nanotubes by the pyrolysis of acetylene-organometallic mixtures, Chem. Phys. Lett., 293 (1998) 47-52.

[III.29] R. Sen, A. Govindaraj, C.N.R. Rao, Carbon nanotubes by the metallocene route, Chem. Phys. Lett., 267 (1997) 276-280.

[III.30] R.L. Vander Wal, L.J. Hall, Carbon nanotube synthesis upon stainless steel meshes, Carbon, 41 (2003) 659-672.

[III.31] S.J. Park, D.G. Lee, Development of CNT-metal-filters by direct growth of carbon nanotubes, Current Appl. Phys., 6 (2006) e182-e186.

[III.32] S.J. Park, D.G. Lee, Development of CNT-metal-filters by direct growth of carbon nanotubes, Current Appl. Phys., 6 (2006) e182-e186.

[III.33] D. Park, Y.H. Kim, J.K. Lee, Synthesis of carbon nanotubes on metallic substrates by a sequential combination of PECVD and thermal CVD, Carbon, 41 (2003) 1025-1029.

[III.34] M. Karwa, Z. Iqbal, S. Mitra, Scaled-up self-assembly of carbon nanotubes inside long stainless steel tubing, Carbon, 44 (2006) 1235-1242.

[III.35] Y. Soneda, M. Makino, Formation and texture of carbon nanofilaments by the catalytic decomposition of CO on stainless-steel plate, Carbon, 38 (2000) 478-480.

[III.36] N. Jeong, J. Lee, Growth of filamentous carbon by decomposition of ethanol on nickel foam: Influence of synthesis conditions and catalytic nanoparticles on growth yield and mechanism, J. Catal., 260 (2008) 217-226.

[III.37] W. Huang, X.-B. Zhang, J. Tu, F. Kong, Y. Ning, J. Xu, G. Van Tendeloo, Synthesis and characterization of graphite nanofibers deposited on nickel foams, Phys. Chem. Chem. Phys., 4 (2002) 5325-5329.

[III.38] N.A. Jarrah, F. Li, J.G. Van Ommen, L. Lefferts, Immobilization of a layer of carbon nanofibres (CNFs) on Ni foam: a new structured catalyst support, J. Mater. Chem., 15 (2005) 1946-1953.

[III.39] C. Du, N. Pan, CVD growth of carbon nanotubes directly on nickel substrate, Mater. Lett., 59 (2005) 1678-1682.

[III.40] A. Sacco, Jr., F.W.A.H. Geurts, G.A. Jablonski, S. Lee, R.A. Gately, Carbon deposition and filament growth on iron, cobalt, and nickel foils using methane-hydrogen-water-carbon monoxide-carbon dioxide gas mixtures, J. Catal., 119 (1989) 322-341.

[III.41] P.S. Guo, Z. Sun, Y.W. Chen, Z.H. Zheng, A novel approach to mass synthesis of raw CNTs for printed field emission cathodes by chemical vapour deposition, Mater. Lett., 60 (2006) 966-969.

[III.42] E.F. Kukovitsky, S.G. L'Vov, N.A. Sainov, V.A. Shustov, CVD growth of carbon nanotube films on nickel substrates, Appl. Surf. Sci., 215 (2003) 201-208.

[III.43] W. Wunderlich, Growth model for plasma-CVD growth of carbon nano-tubes on Ni-sheets, Diamond Relat. Mater., 16 (2007) 369-378.

[III.44] C. Masarapu, V. Subramanian, H. Zhu, B. Wei, Long-cycle electrochemical behavior of multiwall carbon nanotubes synthesized on stainless steel in Li ion batteries, Adv. Funct. Mater., 19 (2009) 1008-1014.

[III.45] V. Martinez-Hansen, N. Latorre, C. Royo, E. Romeo, E. Garcia-Bordeje, A. Monzon, Development of aligned carbon nanotubes layers over stainless steel mesh monoliths, Catal. Today, 147 (2009) S71-S75.

[III.46] A.N. Karwa, B.J. Tatarchuk, Aerosol filtration enhancement using carbon nanostructures synthesized within a sintered nickel microfibrous matrix, Sep. Pur. Tech., (In press) (2011).

[III.47] C. Bernardo, D.L. Trimm, Structural factors in the deposition of carbon on nickel, Carbon, 14 (1976) 225-228.

[III.48] N.K. Reddy, J.-L. Meunier, S. Coulombe, Growth of carbon nanotubes directly on a nickel surface by thermal CVD, Mater. Lett., 60 (2006) 3761-3765.

[III.49] L.E. Cratty, Jr., A.V. Granato, Dislocations as "active sites" in heterogeneous catalysis, J. Chem. Phys., 26 (1957) 96-97.

[III.50] C.A. Bernardo, L.S. Lobo, Kinetics of carbon formation from acetylene on nickel, J. Catal., 37 (1975) 267-278.

[III.51] R.T.K. Baker, J.J. Chludzinski, Jr., Filamentous carbon growth on nickel-iron surfaces: the effect of various oxide additives, J. Catal., 64 (1980) 464-478.

[III.52] R.T.K. Baker, M.A. Barber, P.S. Harris, F.S. Feates, R.J. Waite, Nucleation and growth of carbon deposits from the nickel catalyzed decomposition of acetylene, J. Catal., 26 (1972) 51-62.

[III.53] Y. Nishiyama, Y. Tamai, Effect of hydrogen on carbon deposition catalyzed by copper-nickel alloys, J. Catal., 45 (1976) 1-5.

[III.54] M.S. Kim, N.M. Rodriguez, R.T.K. Baker, Interaction of hydrocarbons with copper-nickel and nickel in the formation of carbon filaments, J. Catal., 131 (1991) 60-73.

[III.55] R.T.K. Baker, P.S. Harris, R.B. Thomas, R.J. Waite, Formation of filamentous carbon from iron-, cobalt-, and chromium-catalyzed decomposition of acetylene, J. Catal., 30 (1973) 86-95.

[III.56] G.S. Choi, Y.S. Cho, S.Y. Hong, J.B. Park, K.H. Son, D.J. Kim, Carbon nanotubes synthesized by Ni-assisted atmospheric pressure thermal chemical vapor deposition, J. Appl. Phys., 91 (2002) 3847-3854.

[III.57] C.J. Lee, J. Park, Y. Huh, J.Y. Lee, Temperature effect on the growth of carbon nanotubes using thermal chemical vapor deposition, Chem. Phys. Lett., 343 (2001) 33-38.

[III.58] C.J. Lee, J. Park, S.Y. Kang, J.H. Lee, Growth of well-aligned carbon nanotubes on a large area of Co-Ni co-deposited silicon oxide substrate by thermal chemical vapor deposition, Chem. Phys. Lett., 323 (2000) 554-559.

[III.59] Z.P. Huang, D.Z. Wang, J.G. Wen, M. Sennett, H. Gibson, Z.F. Ren, Effect of nickel, iron and cobalt on growth of aligned carbon nanotubes, Appl. Phys. A: Mater. Sci. Process., 74 (2002) 387-391.

[III.60] Z.P. Huang, J.W. Xu, Z.F. Ren, J.H. Wang, M.P. Siegal, P.N. Provencio, Growth of highly oriented carbon nanotubes by plasma-enhanced hot filament chemical vapor deposition, Appl. Phys. Lett., 73 (1998) 3845-3847.

[III.61] Z.Y. Juang, I.P. Chien, J.F. Lai, T.S. Lai, C.H. Tsai, The effects of ammonia on the growth of large-scale patterned aligned carbon nanotubes using thermal chemical vapor deposition method, Diamond Relat. Mater., 13 (2004) 1203-1209.

[III.62] S. Wei, W.P. Kang, J.L. Davidson, J.H. Huang, Aligned carbon nanotubes fabricated by thermal CVD at atmospheric pressure using Co as catalyst with NH_3 as reactive gas, Diamond Relat. Mater., 15 (2006) 1828-1833.

[III.63] M. Jung, K.Y. Eun, Y.-J. Baik, K.-R. Lee, J.-K. Shin, S.-T. Kim, Effect of NH_3 environmental gas on the growth of aligned carbon nanotube in catalytically pyrolizing C_2H_2, Thin Solid Films, 398-399 (2001) 150-155.

[III.64] Z.F. Ren, Z.P. Huang, J.W. Xu, J.H. Wang, P. Bush, M.P. Siegel, P.N. Provencio, Synthesis of large arrays of well-aligned carbon nanotubes on glass, Science, 282 (1998) 1105-1107.

[III.65] Y. Chen, S. Patel, Y. Ye, D.T. Shaw, L. Guo, Field emission from aligned high-density graphitic nanofibers, Appl. Phys. Lett., 73 (1998) 2119-2121.

[III.66] C. Bower, W. Zhu, S. Jin, O. Zhou, Plasma-induced alignment of carbon nanotubes, Appl. Phys. Lett., 77 (2000) 830-832.

[III.67] S.-F. Lee, Y.-P. Chang, L.-Y. Lee, Effects of Ni catalyst annealing in nitrogen-containing gases on the surface morphology and field-emission properties of thermal chemical vapor deposited carbon nanotubes, Xinxing Tan Cailiao, 23 (2008) 302-308.

[III.68] C.F. Cullis, N.H. Franklin, The pyrolysis of acetylene at temperatures from 500 to 1000˚C, Proc. Roy. Soc., 280 (1964) 139-152.

[III.69] A.E.B. Presland, P.L. Walker, Jr., Growth of single-crystal graphite by pyrolysis of acetylene over metals, Carbon, 7 (1969) 1-8.

[III.70] M.S. Kim, N.M. Rodriguez, R.T.K. Baker, The interplay between sulfur adsorption and carbon deposition on cobalt catalysts, J. Catal., 143 (1993) 449-463.

[III.71] R.W. McCabe, Kinetics of ammonia decomposition on nickel, J. Catal., 79 (1983) 445-450.

[III.72] A.E. Shalagina, Z.R. Ismagilov, O.Y. Podyacheva, R.I. Kvon, V.A. Ushakov, Synthesis of nitrogen-containing carbon nanofibers by catalytic decomposition of ethylene/ammonia mixture, Carbon, 45 (2007) 1808-1820.

Chapter IV A novel nano-nonwoven fabric with 3-dimensionally dispersed nanofibers: entrapment of carbon nanofibers within nonwovens using wet-lay process

IV.1 Abstract

This study describes the manufacturing of novel nano-nonwovens that are comprised of 3-dimensionally distributed carbon nanofibers within the matrices of traditional wet-laid nonwovens. The preparation of these nano-nonwovens involves dispersing and flocking carbon nanofibers, and optimizing colloidal chemistry during wet-lay formation. The distribution of nanofibers within the nonwoven was verified using polydispersed aerosol filtration testing, air permeability, low surface tension liquid capillary porometry, SEM and cyclic voltammetry. All these characterization techniques indicated that nanofiber flocks did not behave as large solid clumps, but retained the 'nano-porous' structure expected from nanofibers. The reduction-oxidation reactions of functional groups on nanofibers and the linear variation of electric double layer capacitance with nanofiber loading were measured using cyclic voltammetry. More than 700 ft^2 of the composite were made during the demonstration of process scalability using a Fourdrinier type continuous pilot papermaking machine.

IV.2 Introduction

Nonwoven fabrics/media are a class of fibrous materials made from strands of fibers that are neither woven nor knitted. These fabrics can be made from a variety of materials such as cellulose, polymer, glass, and/or metal fibers. This flexibility of fiber materials along with the proven manufacturing processes makes nonwovens a popular choice for various applications such as filtration, medical fabrics and hygiene products. The next generation of nonwovens being intensely researched are nonwoven composites with nanofibers [IV.1-5]. Nanofiber nonwoven fabrics/media have various applications such as aerosol filtration [IV.2, 5-8], coalescence filtration [IV.9, 10] and high flux ultrafiltration membranes [IV.11]. The nanofibers with regard to nonwoven media are typically defined as fibers with diameter less than 500 nm.

Currently, electrospinning technology is predominantly used to produce nonwoven media with polymer nanofibers [IV.3, 7, 12]. It is capable of producing polymer nanofibers between 100-1000 nm [IV.1]. Melt-blown fiber technologies have the potential to produce polymer nanofibers and are now breaking the 500 nm barrier [IV.3]. However, electrospinning and melt-blown fiber technologies produce fragile structures of polymer nanofibers that lack the strength required for many processing and applications involving nonwovens. Therefore, nonwoven media with fibers of diameter 2-20 μm are used as support structures with nanofibers layered over them, producing a heterogeneous structure. The nanofiber nonwoven media produced by these technologies have a 2-dimensional surface distribution of nanofibers.

No existing process can produce nonwoven composites with uniform 3-dimensional distribution of nanofibers within the nonwovens. Also, the use of carbon nanotubes/nanofibers within nonwoven media has not been widely researched and is of significant interest due to their nano-scale dimensions [IV.13, 14]. The scalability of the process/technology is an important

factor to be considered for any application involving nanomaterials in order to harness the potential of 'nano' for engineering applications. Therefore, the use of commercially available carbon nanofibers in the manufacturing of nanofiber nonwoven composite (nano-nonwoven) is an attractive option for a scalable process. However, commercial nanofibers are in the form of large clumps and aggregates that do not readily yield 'nano-porous' characteristics within the nonwovens.

The focus of this work was to create a novel nano-porous nonwoven media with uniform 3-dimensional distribution of carbon nanofibers and to demonstrate process scalability. The wet-lay process for manufacturing nonwovens was the process of choice because it could incorporate the existing methodologies for nanofiber dispersion with wet-processing of microfibers.

IV.3 Experimental

IV.3.1 Materials

The nano-nonwovens were made using microfibers and nanofibers, where the microfibers created the supporting matrices within which nanofibers were entrapped. Vapor grown carbon nanofibers (VGCF) (product # PR-19-XT-PS-OX - batch 5713) with an average diameter of 150 nm were obtained from Pyrograf Products Inc. The surfactant Pluronic-F68 manufactured by BASF was obtained from Sigma-Aldrich. Cationic polyacrylamide flocculent 'Superfloc-4512' (39% polyacrylamide solution in water with 10% (mol.) cationic charge) was obtained from Kemira. Nickel microfibers (alloy Ni-200) with nominal diameter of 4 μm and length of 3 mm were obtained from Intramicron Inc. (Auburn, AL). Glass fibers of nominal diameter 2.4 μm and 5 μm were obtained from Lauscha Fiber International. The cellulose fibers were a mixture of hardwood and softwood fibers.

IV.3.2 Method

The vapor grown carbon nanofibers (VGCF) dispersion was made by adding VGCF to 1 g/l aqueous solution of Pluronic-F68 surfactant, and mixing it for at least 72 hrs using a magnetic stirrer or a laboratory mixing propeller. The concentration of VGCF in the dispersion was 1 g/l. The dispersed VGCF were flocked using cationic polyacrylamide (cPAM) flocculent. The as-received solution of cPAM was diluted to 0.39% solids (w/w) to exfoliate the polymer chains before its use. The addition of 0.8-1 ml of cPAM solution was sufficient to completely flock 1 liter of VGCF dispersion. For all calculations, the absolute density of VGCF was taken as 1.6 g/cc including the hollow center of VGCF, as per the manufacturer's recommendation.

Microfibers, such as nickel or glass fibers, were dispersed in water using a mechanical blender in a separate container. The dispersions of microfibers and flocked VGCF were mixed to make preforms of nano-nonwoven media, using a 16 cm diameter TAPPI hand-sheet former. The microfibers in the wet-laid preform are randomly oriented due to the inherent randomness of the wet-lay formation. The VGCF flocks were entrapped within the microfibrous matrix during wet-lay formation, creating a nonwoven preform with a uniform 3-dimensional distribution of nanofibers. The final nonwoven media is made by binding the microfibers of the preform using a chemical binder or by thermal binding (sintering). If cellulose fibers are used during wet-lay, there is no need for chemical binders because hydrogen bonding between cellulose fibers gives the strength required for the nonwoven structures. The nano-nonwoven preforms made with nickel microfibers were sintered for 30 min at 950^{o}C with 5-7% hydrogen in nitrogen.

The required dimensions of the samples were punched out from the nonwoven media using a steel punch. The nonwoven media made with nickel microfibers can be cold-compressed to a large extent due to the malleable nature of metal fibers. The samples were compressed

between two 15.2 cm × 15.2 cm × 0.64 cm polished steel plates. Washers were used as spacers between the steel plates to define the final thickness of the samples. A sample size of 54 mm diameter was required for aerosol filtration efficiency and Gurly permeability tests, and 14.3 mm diameter samples were used for cyclic voltammetry tests. Unless noted otherwise, all the analyses in this study were done on nano-nonwovens made with 4 μm nickel microfibers and varying quantities of VGCF. All nickel nonwoven samples had a thickness of 0.8 mm and the nickel fiber volume was kept constant at 3.4%.

IV.3.3 Characterization

IV.3.3.1 Physical structure characterization

The process of VGCF dispersion, flocking and interaction with microfibers during wet-lay was captured using an optical microscope. The final microscopic structures of the nano-nonwoven composites were observed using a JEOL 7000-F SEM. The nitrogen Brunauer-Emmett-Teller (BET) surface area of VGCF was found using Autosorb-1 from Quantachrome Instruments. A capillary porometer (model# CFP-1200-AEXM) from Porous Materials Inc. was used to measure the mean pore diameter and bubble point diameter of the nano-nonwovens. The wetting liquid used for porometry was Galwick^{TM}, which has a low surface tension of 15.9 mJ/m^2 at 20^{o}C.

IV.3.3.2 Air permeability and aerosol filtration efficiency testing

Air permeability and aerosol filtration efficiency across the nonwovens were measured using the setup shown in Fig. IV-1. House air was used as the air supply required for the setup. As shown in Fig. IV-1, a silica-gel desiccator was used to remove any moisture from the house air. Thereafter, the air was filtered using inline HEPA filters to remove any background aerosol

contamination. For filtration testing, the dry air was split into two flow paths and their flow rates were controlled using mass flow controllers (MFC). One portion of the dry air was directed to the nebulizer, and the other portion of the air was used as aerosol drying air. The DeVilbiss nebulizer (product # 4650D-621) with 10% (w/w) potassium chloride solution was used to produce low concentration of polydispersed aerosol. The drying air was ionized using a SIMCO neutralizer (product # AN-6) to neutralize any static charge developed on the potassium chloride particles due to aerosolizing. The flow to the nebulizer was 1.2-1.4 l/min and the aerosol drying air was 25-30 l/min. The final concentration of the challenge aerosol was between 160,000 to 300,000 particles per 100 cc after the mixing of drying air and nebulizer air. Most of the aerosol stream was directed towards the exhaust. Approximately 10% of the aerosol stream was forced through the sample using a Venturi vacuum pump. The face velocity of air at the media was controlled by the downstream MFC before the Venturi vacuum pump. The downstream MFC was protected by two inline HEPA filters. The particle counter used for filtration efficiency tests was LAS-X II from Particle Measuring Systems (Boulder, Co). The error bars on the aerosol filtration efficiency tests are reported at a 95% confidence interval as per ASHRAE 52.2 standard [IV.15].

For air permeability measurements, the pressure drop across the media was measured at various face velocities using an Omega (Product # PX154-010DI) pressure transducer. A small modification to the setup was required for measuring pressure drop across the nonwoven media. The exhaust and the nebulizer air supply were shut off, and the vacuum line was opened for ambient pressure exhaust. The filter media test section was made of a 25.4 mm ID stainless steel pipe and flanges. The filtration/pressure drop test area was 25.4 mm in diameter. Samples with a

larger diameter (54 mm) than the test area were used to provide good leak-proofing around the test area.

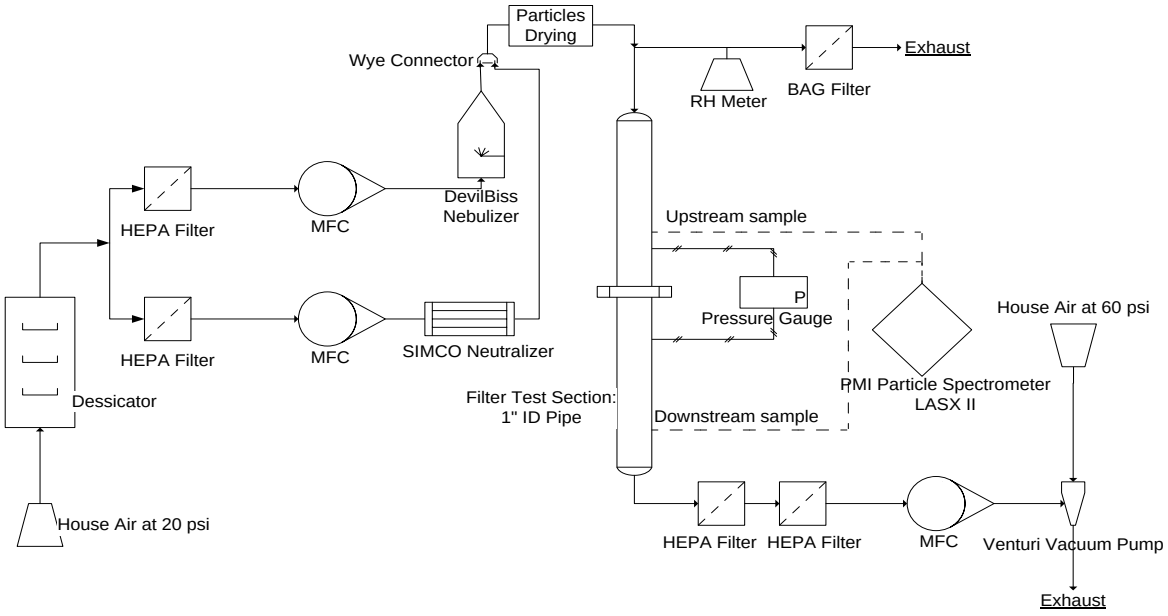

Fig. IV-1. Aerosol filtration efficiency and pressure drop test setup.

IV.3.3.3 Cyclic voltammetry

Nano-nonwovens made with nickel microfibers were used to electrically verify the entrapment of VGCF. Samples with a diameter of 14.3 mm were sintered to nickel foils to make the electrode assemblies. The nickel foil acted as the current collector for the electrodes. The redox reactions and double layered capacitance were measured using cyclic voltammetry (CV). The tests were performed with a 5 M potassium hydroxide solution as the electrolyte, a platinum foil as counter electrode and a silver/silver chloride reference electrode. The EG&G Princeton Applied Research Potentiostat (model 273A) was used for the CV tests. The scan rate for CV was 100 mV/s and the data was collected on the 5^{th} sweep.

IV.4 Results and Discussion

IV.4.1 Vapor grown carbon nanofibers (VGCF) dispersion and flocking

IV.4.1.1 Vapor grown carbon nanofibers (VGCF) dispersion

The as-received VGCF were in the form of dry powder with large clumps ranging in diameter from a few hundred microns to a few mm. The clumps are formed because of the strong van der Waals forces between the nanofibers. These VGCF clumps can be entrapped within nonwoven media during wet-lay formation. However, the clumps will act as large solid particles and will not yield any enhancement in property by the nano-scale of VGCF. To harness the novel properties of nanofibers, it is important to exfoliate the VGCF clumps into individual nanofibers.

The VGCF clumps can be broken and the nanofibers can be individualized by overcoming the van der Waals forces between nanofibers. The easiest method to individualize VGCF is by using a surfactant or solvent. The use of surfactants and solvents to disperse carbon nanotubes/nanofibers and other nanostructures has been widely studied [IV.16-21]. The surfactant method of dispersing VGCF was chosen because of its ease of scalability and the inherent safety of the process. Dispersion of VGCF requires long mixing times to overcome the van der Waals forces. The mixing time of VGCF-surfactant solution was chosen as 72 hours for this study. The individual nanofibers obtained after dispersion do not get entrapped within the large cage matrix created by 2-20 μm (dia.) microfibers during wet-lay, and drain with water because of their small dimensions. The individually dispersed VGCF were entrapped within 0.6 μm and 0.45 μm (dia.) glass microfiber nonwovens. However, the water drain time during wet-lay was more than 24 hours, which made the process non-scalable for VGCF entrapment using glass microfibers.

IV.4.1.2 Flocking

The approach taken to entrap the VGCF was to disperse them into individual nanofibers and then flock them using a flocking agent. Low charge polymeric flocking agents, like the one used in this study, flock the materials by counter-charge bridge mechanism, as shown in Fig. IV-2 [IV.22]. The flocking agents require charged surfaces to which they adsorb with multiple loops, extending beyond the electric double layer of the charged surface (Fig. IV-2 (a)). These loops adsorb to the second surface during mixing and flock the two surfaces (Fig. IV-2 (b)). For the VGCF dispersion to flock, the nanofibers need to be a charged species in the colloidal system. The catalytically synthesized vapor grown carbon nanofibers (VGCF) do not have any charge on their surface. However, functionalizing the VGCF can make them anionic/cationic in water depending on the functional groups.

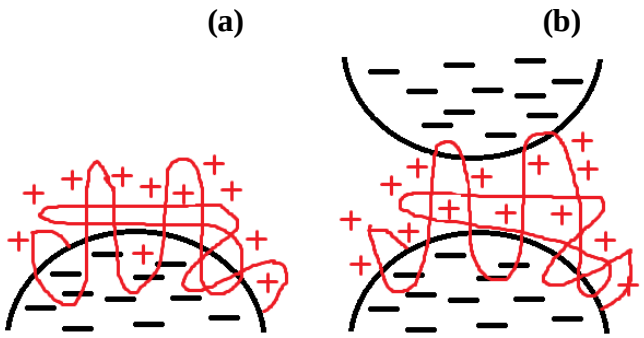

Fig. IV-2. Schematics of the counter-charge bridge mechanism of flocking: (a) cationic polymer flocculent initially adsorbs onto anionic particle, and (b) the flocculent loops adsorb onto second anionic particle causing “bridge” flocculation.

The manufacturer, Pyrograf Products Inc., produce oxidized VGCF which have 10% (atomic) oxygen as observed by XPS. The oxidized VGCF have carboxylic acid, phenol, lactone and quinine functional groups. At a pH of 7, the carboxylic acid groups dissociate in water to

give a negative charge to the VGCF. This negatively charged VGCF can be flocked using a positively charged polymeric flocking agent such as cationic polyacrylamide (cPAM). Ionic surfactants interfere with the ionic colloidal interaction between VGCF and cPAM, and prevent the flocking of VGCF. For example, a widely used anionic surfactant, sodium dodecyl sulfate (SDS) dispersed in water, interacts with cPAM and renders the cationic charge of cPAM ineffective for flocking VGCF. Therefore, a non-ionic surfactant was seen as the best route to prevent any unwanted ionic interference in the VGCF-cPAM colloidal system. The non-ionic surfactant chosen was Pluronic-F68, manufactured by BASF. Pluronic-F68 surfactant is a copolymer of polypropylene oxide (hydrophobic) and polyethylene oxide (hydrophilic). The quantity of cPAM required to completely flock VGCF is shown in Table IV-1. Fig. IV-3 shows the change in the packing density of VGCF after dispersion and flocking. The as-received VGCF had a packing density of 45.4 kg/m^3 (Fig. IV-3 (a)) which decreased to ~2.22 kg/m^3 (Fig. IV-3 (c)) after dispersion and flocking. The significant change in the packing density after dispersion and flocking of VGCF signifies the exfoliation of VGCF clumps. The low density flocks of VGCF will occupy more volume as compared to the VGCF clumps, for the same weight of entrapped VGCF.

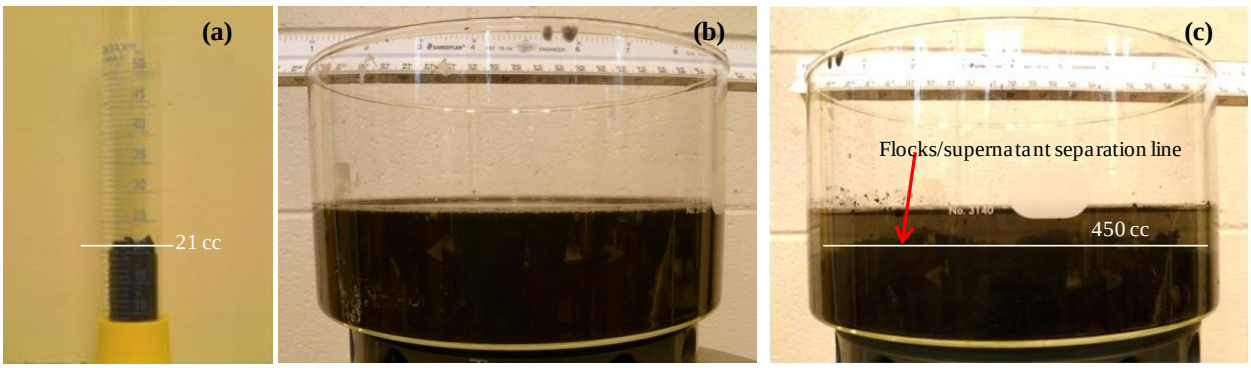

Fig. IV-3. Photographs of 1 g VGCF at various stages of nano-nonwoven preparation: (a) as-received, (b) dispersed using surfactant (1 liter solution at VGCF concentration of 1 g/l), and (c) flocked.

Table IV-1. Quantity of cPAM flocculent required for flocking VGCF dispersion.

Sr. no.	1 g/lt VGCF dispersion (ml)	cPAM added (0.39%) (ml)	Observation
1	100	0.02	No flocs visible
2	100	0.04	Supernatant has dispersed VGCF
3	100	0.08	Most VGCF flocked
4	100	0.1	All VGCF flocked
5	100	0.2	All VGCF flocked

IV.4.2 Wet-lay preform and nickel nonwoven with VGCF

VGCF clumps (Fig. IV-4 (a)) dispersed very well in 1 g/l solution of Pluronic-F68 after 72 hours of mixing. The VGCF dispersion (Fig. IV-4 (b)) was flocked using cPAM prior to wet-lay. As shown in Fig. IV-4 (c), the large size of VGCF flocks gave them the ability to get entrapped within the nonwoven matrices of 2-20 µm (dia.) microfibers. These flocks retained the nano-porous structure expected from individual nanofibers. The VGCF flocks were non-rigid soft structures that were entangled with microfibers in the TAPPI hand-sheet former, as shown in Fig. IV-4 (d). After draining the water from the hand-sheet former, the VGCF were randomly

distributed within the 3-dimensional nonwoven preform. Gravimetric measurements showed that there was no significant loss of VGCF with the drain water.

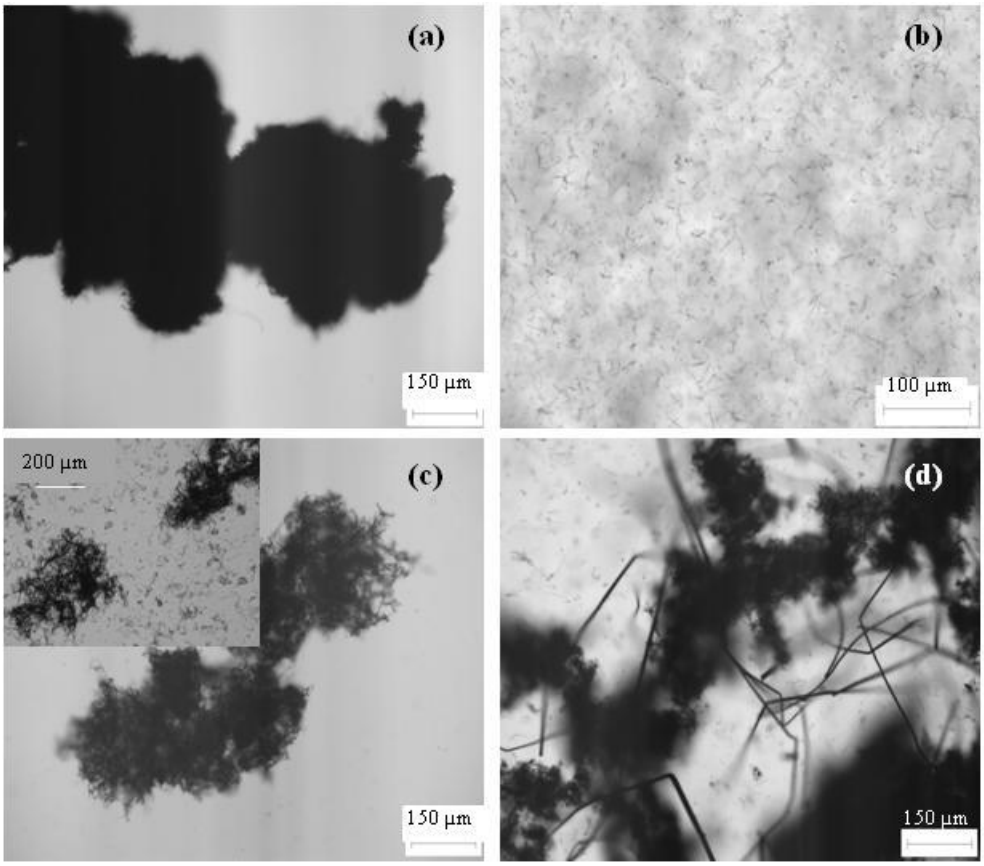

Fig. IV-4. Optical microscope images at various stages of nano-nonwoven preparation: (a) as-received VGCF dry clumps, (b) VGCF dispersion in surfactant solution, (c) flocked VGCF prior to addition in the hand-sheet former, and (d) VGCF flocks mixed with 4 µm nickel fiber dispersion before wet-lay (sample taken from liquid in the head box of hand-sheet former).

Nickel microfibers were chosen to prepare the nano-nonwovens because of their electrical conductivity, the easy compressibility of nickel nonwovens due to the malleable nature of nickel, and their ability to sinter which avoids the use of a chemical binder. Chemical binders were avoided because they may clog the pores of the VGCF flocks leading to inaccurate analysis. Nickel microfibers of 4 µm (dia.) were used to entrap varying quantities of the VGCF

using the flocking procedure described in Section IV.4.1. These nickel nonwoven preforms, made in the hand-sheet former, were sintered to form mechanically robust nonwovens without any addition of chemical binders. The sintering of the nickel preform was done at 950^{o}C for 30 min in a reducing environment with 5-7% hydrogen in nitrogen. The Fig. IV-5 (a) shows the SEM image of as-received VGCF clumps that were dispersed and then flocked. The SEM images of the final sintered nickel nonwovens with varying quantities of VGCF are shown in Fig. IV-5 (b), (c), (d) and (e).

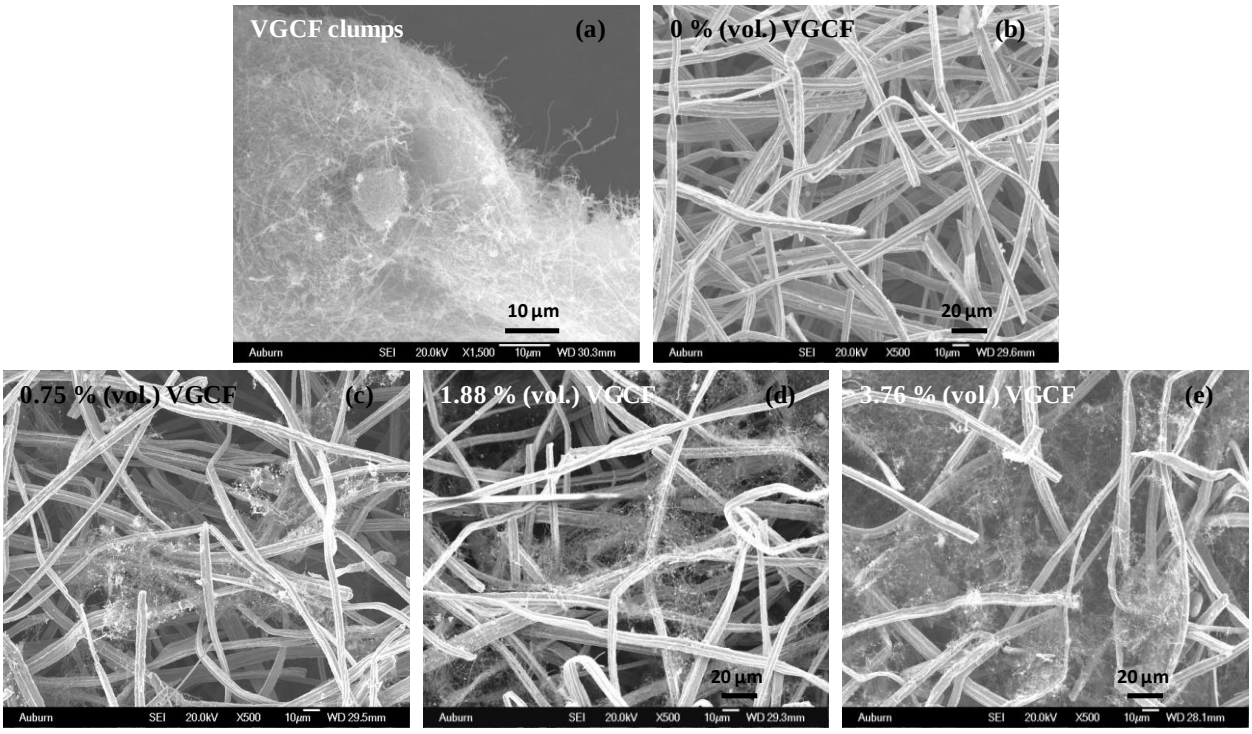

Fig. IV-5. SEM images of: (a) as-received VGCF clumps, (b) 4 µm sintered nickel fiber nonwoven sheet (3.4% (vol.)), (c) 0.75% (vol.) VGCF within sintered nickel sheet (3.4% (vol.)), (d) 1.88% (vol.) VGCF within sintered nickel sheet (3.4% (vol.)), and (e) 3.76% (vol.) VGCF within sintered nickel sheet (3.4% (vol.)).

One concern during metal nonwoven sintering was the catalytic gasification of entrapped carbon [IV.23-25]. The sintering conditions were simulated in a thermal gravimetric analyzer

(TGA) to check for the loss of VGCF due to catalytic gasification. The temperature ramp to 950˚C was done at 100˚C/min under helium flow to minimize the time required to reach the desired temperature (950˚C). At 950˚C, the gas was switched from helium to 5% hydrogen in helium, and the weight loss was measured for 30 min. As shown in Fig. IV-6, there was an insignificant loss of 0.3% (wt.) observed for nickel fiber matrix for sintering conditions at the end of the 30 min run. This small loss in weight of nickel fibers can be attributed to the reduction of nickel oxide to metallic nickel and contaminant removal from the surface of fibers. For the same conditions, the as-received VGCF lost ~3.25% of its weight. The solid line in Fig. IV-6 shows the calculated weight loss of nickel nonwoven with entrapped VGCF without any gasification. The TGA data for nickel nano-nonwoven shows the loss of weight due to gasification of VGCF. From Fig. IV-6 it can be deduced that the weight loss due to the gasification of VGCF was ~3.25% of its original weight. This showed that there was no significant loss of VGCF due to gasification during the sintering of the nickel nano-nonwovens.

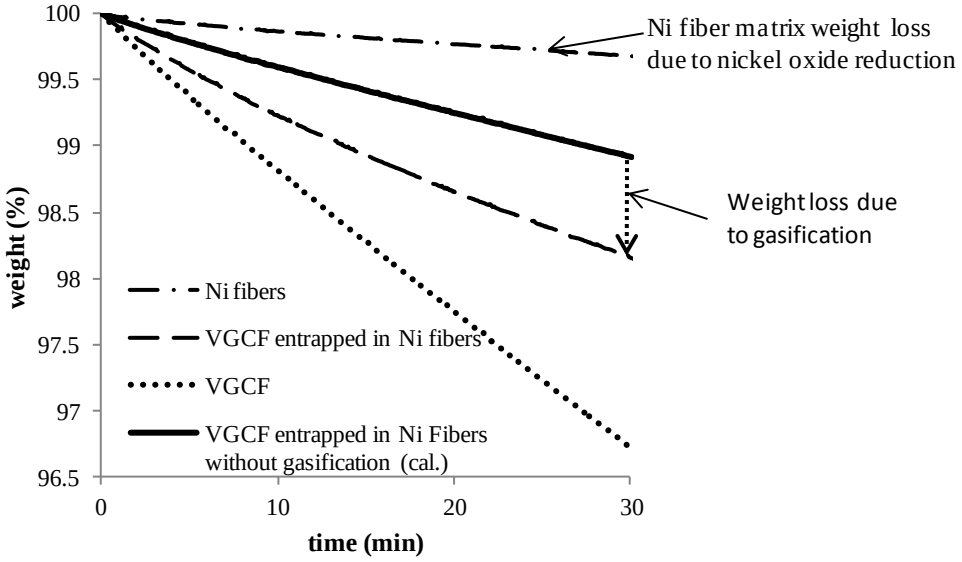

Fig. IV-6. TGA of 4 μm nickel nonwoven (3.4% (vol.)) with VGCF (5.78% (vol.)). (Gas: 5% in H_2 in He, temperature 950˚C)

Instead of flocking and physically entrapping VGCF within the microfibrous matrices, the microfibers can be coated with nanofibers by changing the point of cPAM addition. If microfibers have anionic functional groups on the surface, such as Kraft cellulose fibers, the cPAM will attach to the microfibers. When the cPAM attached microfibers come in contact with the non-ionic surfactant dispersion of VGCF, the cPAM interacts with the anionic VGCF to form a coating of VGCF on the surface of microfibers. However, most of the VGCF in the dispersion did not interact with microfibers and was lost with the drain water during the preform formation. Due to no significant retention of VGCF, the coating method was not studied in detail and the flocking of VGCF before wet-lay was chosen as the preferred route for VGCF entrapment.

IV.4.3 Pore size distribution

The VGCF porous flocks occupy a certain volume within the nickel nonwoven matrices. Increasing the volume fraction of VGCF decreases the pore diameters of the nano-nonwovens. The decrease in mean pore diameter and bubble point pore diameter due to VGCF entrapment was observed using capillary porometry. The bubble point pore diameter is the largest pore diameter of the nonwoven. Nickel nano-nonwovens with varying quantities of VGCF were tested using porometry. Care was taken to keep the sample thickness constant (0.8 mm) with the same volume fraction of nickel fibers (3.4% (vol.)). The pore diameter was calculated using the formula described in Eq. (IV.1), where ‘d’ is the pore diameter (m), ‘σ’ is the surface tension of liquid (J/m^2), ‘θ’ is contact angle between liquid and pore wall (˚), and ‘p’ is the pressure (Pa) required for displacing liquid from the pore diameter [IV.26]. For a low surface tension liquid, such as the one used in this study, ‘θ’ can be assumed to be 0˚ [IV.27]. This means that the analysis of pore size distribution remains accurate irrespective of the nonwoven materials.

$$d = \frac{2.86\sigma \cos\theta}{p} \qquad \text{(IV.1)}$$

As shown in Fig. IV-7, bubble point and mean pore diameters decrease with increasing VGCF volume fraction. We hypothesize that, if the VGCF volume fraction is high enough, the VGCF forms a continuous nano-porous network throughout the nonwoven. This hypothesis is supported by the decrease of mean pore diameter to less than 500 nm for 5.78% (vol.) of VGCF in the nickel nonwoven. This small mean pore diameter cannot be achieved unless the large pores of microfibers are completely covered by VGCF.

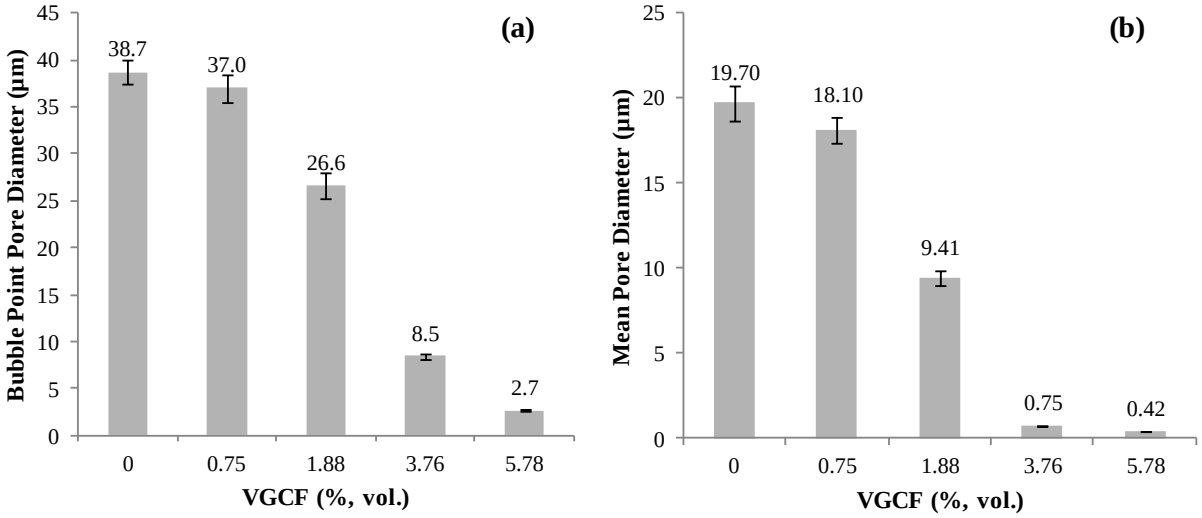

Fig. IV-7. Liquid capillary porometry data for 4 µm nickel nonwoven (3.4% (vol.)) with varying quantity of VGCF: (a) bubble point pore diameter and (b) mean pore diameter. (Sample thickness was 0.8 mm.)

The change in drain time of water during wet-lay can give a qualitative understanding of the change in the pore size distribution of the nonwovens. Typically during wet-lay, the use of small diameter microfibers increase the resistance to water drainage because of the smaller pores

created within the nonwoven. As shown in Table IV-2, the drain time increases notably for VGCF/Ni-fiber ratios (vol.) greater than 1. For VGCF/Ni volume ratios greater than 1.7, the water drain rate was very slow. The significant increase in drain time qualitatively demonstrates the large decrease in mean pore diameter of the nonwovens due to the addition of VGCF.

Table IV-2. Drain time of water from the sheet former during wet-lay of nano-nonwoven with 5 g of 4 μm nickel fibers and varying quantity of VGCF.

VGCF / Ni ratio (vol.)	VGCF % after compression	Drain time (s)
0	0	< 3
0.22	0.75	< 3
0.55	1.88	< 3
1.11	3.76	10
1.70	5.78	40

IV.4.4 Pressure drop and aerosol filtration efficiency

Nonwoven media are used as water and aerosol filters. The flow of fluid through the nonwoven media, characterized by filtration efficiency and pressure drop, can provide an insight into the structure of nonwovens. The change in aerosol filtration efficiency and pressure drop of the nickel nano-nonwovens due to the addition of VGCF was studied.

IV.4.4.1 Pressure drop/Air permeability

The pressure drop across the nano-nonwovens follow Darcy's law, where the pressure drop increases linearly with the face velocity, as shown in Fig. IV-8 (A). The Fig. IV-8 (B) shows the rapid increase in pressure drop with VGCF volume fraction within the nano-nonwoven. The rapid increase in pressure drop may be attributed to the reduction of mean pore diameter of the nonwoven and the increase in total surface area due to the entrapped VGCF.

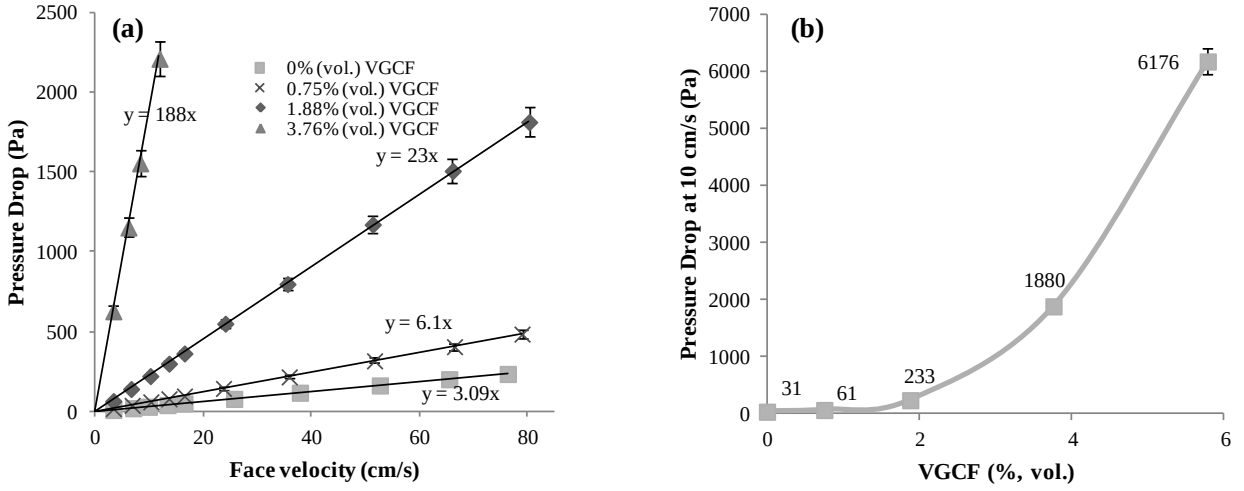

Fig. IV-8. Pressure drop across 4 μm nickel nonwoven (3.4% (vol.)) with varying quantities of VGCF: (a) variation with face velocity and (b) variation with quantity of VGCF (face velocity: 10 cm/s). (Sample thickness was 0.8 mm.)

IV.4.4.2 Aerosol filtration efficiency

The filtration efficiency of the nano-nonwovens increased with VGCF volume fraction. As shown in Fig. IV-9, the filtration efficiency can be varied from 24% to 99.9% by varying the quantity of VGCF. The filtration efficiency is a very strong function of the filter fiber surface area. The significant increase in filtration efficiency (Fig. IV-9) indicates that the VGCF were acting as individual fibers and not macro-size particles. In comparison with the entrapment of solid particles with diameters between 90-125 μm, the pressure drop and filtration efficiencies of VGCF nano-nonwoven increased much faster than that of nonwovens with solid particles. Nonwovens with ~5% (vol.) of 90-125 μm particles contributed to a fractional increase in pressure drop and filtration efficiency [IV.28], which is unlike the trends shown in Fig. IV-8 and Fig. IV-9. This implies that the flocked VGCF had characteristics of individual nanofibers during airflow through the nonwoven composites.

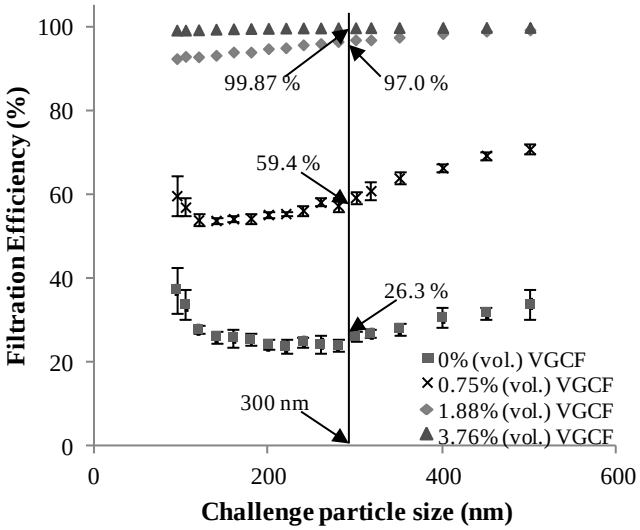

Fig. IV-9. Aerosol filtration efficiency of 4 μm nickel nonwoven (3.4% (vol.)) with varying quantities of VGCF. (Sample thickness was 0.8 mm. Tested at 10 cm/s face velocity.)

IV.4.4.3 Quality factor

There exists an optimal volume fraction of VGCF which enhances the filtration efficiency without a significant increase in the pressure drop. The optimal quantity of VGCF can be found by the quality factor (QF) analysis. The physical significance of the QF is that for the same pressure drop penalty, filters with a higher QF will have higher filtration efficiency. The QF was calculated using Eq. (IV.2), where 'E' is the fractional filtration efficiency and 'ΔP' is the pressure drop (Pa) [IV.29]. The QF for aerosol particles of various diameters is shown in Fig. IV-10. The QF increases from 0.01 (0% VGCF) to 0.015 (1.88% VGCF) for 300 nm aerosol particle. Increasing the VGCF quantity more than 1.88% (vol.) decreases the quality factor significantly. Therefore, the optimal quantity of VGCF within 4 μm nickel nonwovens is 0.75-1.88% (vol.) from the point of view of aerosol filtration. The quality factor of the optimal VGCF nonwoven composite was marginally higher than that of commercial Lydall HEPA glass-fiber filter media as shown in Table IV-3.

$$QF = \frac{-\ln(1-E)}{\Delta P} \quad \text{(IV.2)}$$

Table IV-3. Comparison of aerosol filtration performance between nickel (3.4% (vol.)) nano-nonwoven and commercial Lydall HEPA filter media.

Filter media	**Filtration efficiency (%, 240 nm)**	**ΔP (Pa) at 10 cm/s**	**Thickness (mm)**	**Quality Factor (240 nm)**
VGCF 1.88% (vol.)	99.991	670	2.3	0.0139
Lydall HEPA	99.990	704	0.5	0.0130

Nanofibers have the potential to enhance aerosol filtration efficiency without a significant increase in pressure drop due to slip flow over nanofibers [IV.1]. When the nonwoven fiber diameter approaches the mean free path of air (65 nm at STP), the fluid mechanics boundary condition of zero velocity at the fiber surface no longer remains true. Modifications have to be made to the boundary condition to include the molecular movement of air. This modification is in the form of non-zero velocity at boundary called the slip flow boundary condition. The slip flow has to be considered for fiber diameters less than 500 nm [IV.1, 4]. The enhancement in QF, due to VGCF entrapment within nonwovens, may be attributed to the slip flow over entrapped nanofibers.

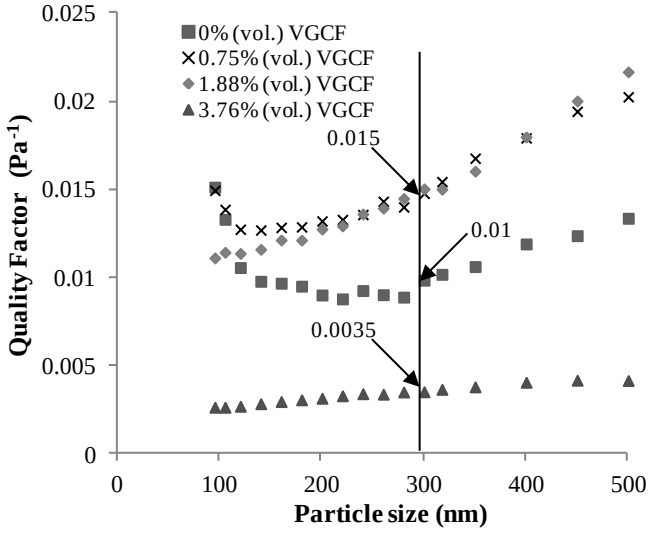

Fig. IV-10. Quality factor of 4 μm nickel nonwoven (3.4% (vol.)) with varying quantities of VGCF.

IV.4.5 Cyclic voltammetry (CV)

Nickel metal microfibers were chosen to study these nano-nonwovens because they could provide additional insight via electrical measurements. Cyclic voltammetry on the nickel nano-nonwovens was investigated to electrically verify the presence of entrapped VGCF. Unlike microscopes which look at only the 2-dimensional surface of the matrix, the CV analyzes the entire 3-dimensional nonwoven matrix. The working electrodes were made by sintering the samples to a nickel foil current collector, as shown in Fig. IV-11. Fig. IV-12 (a) shows the current-voltage data used for calculating double-layer capacitance of nano-nonwovens with varying quantities of VGCF. The double layer capacitance was calculated by Eq. (IV.3), where 'C' is the electric double-layer capacitance (F), 'q' is the total charge stored (C), 'Δt' is the time taken to scan in one direction (s), 'v' is the scan rate (V/s) and 'i' is the current (A) [IV.30]. The low volume fractions of entrapped VGCF were also easily detected. The calculated capacitance was found to vary linearly with the quantity of VGCF as shown in Fig. IV-12 (b). Linear

variation in the capacitance implies that all the entrapped VGCF were electrically detected. The double-layer capacitance of VGCF was found to be 10.5 μF/cm^2. The capacitance per unit area is comparable to the values reported in literature for similar carbon nano-materials [IV.31-34]. The BET surface area for VGCF was found to be 22 m^2/g.

$$C = \frac{q}{2v\Delta t} = \frac{\int i\, dt}{2v\Delta t} \qquad \text{(IV.3)}$$

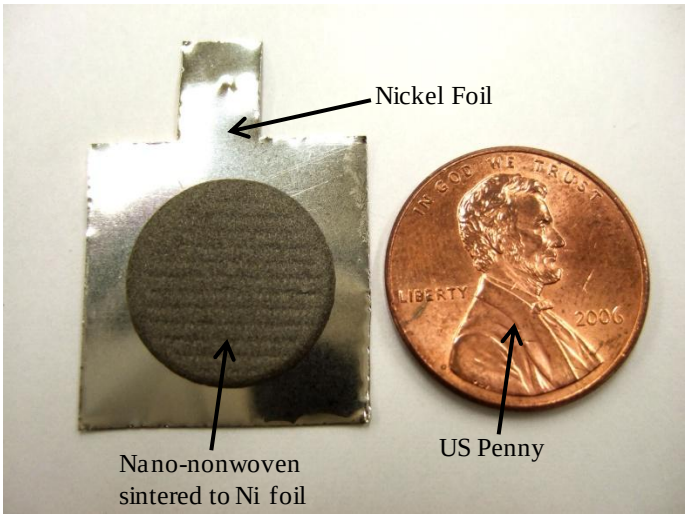

Fig. IV-11. Photograph of electrode made of nickel nano-nonwoven sintered to nickel foil.

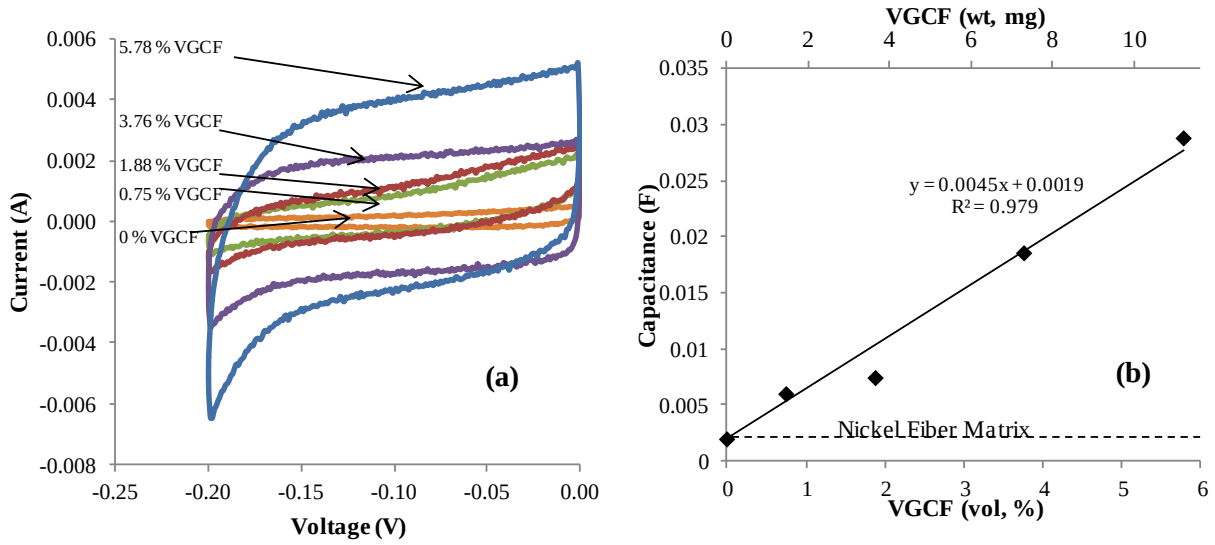

Fig. IV-12. Small voltage-range cyclic voltammetry data for electrodes made of nickel nonwoven (3.4% (vol.)) with varying quantity of VGCF: (a) current-voltage (I-V) data and (b) calculated capacitance from I-V data. (Scan rate: 100 mV/s, Electrolyte: 5 M KOH, Reference Electrode: Ag-AgCl, Counter Electrode: Pt foil)

Cyclic voltammetry was used to observe the presence of functional groups on the VGCF surface. Fig. IV-13 (a) shows the redox peaks of nickel nonwoven without VGCF, and Fig. IV-13 (b) shows the additional redox peaks of the functional groups on the VGCF. The VGCF functional groups undergoing oxidation and reduction may be the following [IV.35, 36]:

$$>C\text{-}OH \leftrightarrow >C{=}O + H^{+} + e^{-}$$

$$-COOH \leftrightarrow -COO + H^{+} + e^{-}$$

$$>C{=}O + e^{-} \leftrightarrow >C\text{-}O^{-}$$

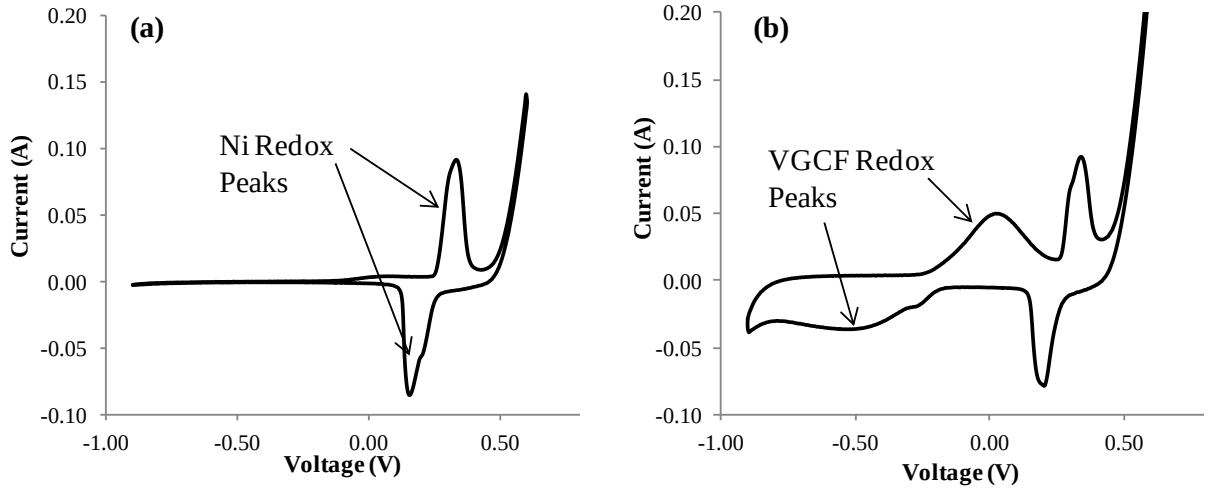

Fig. IV-13. Large voltage-range cyclic voltammetry data for electrodes made of nickel nonwoven (3.4% (vol.)): (a) without VGCF and (b) with 5.78% (vol.) VGCF. (Scan rate: 100 mV/s, Electrolyte: 5 M KOH, Reference Electrode: Ag-AgCl, Counter Electrode: Pt foil)

IV.5 Scale-up demonstration

The manufacturability of the nano-nonwoven composites was demonstrated on a Fourdrinier type continuous pilot papermaking machine shown in Fig. IV-14 (a). 1600 liters of 1 g/l VGCF dispersion was made in 1 g/l Pluronic-F68 solution with a double blade-single shaft agitator. The dispersion was stirred in the agitator for 72 hours. The dispersed VGCF were flocked using cPAM flocculent. The flocked VGCF, along with the microfiber dispersion of glass fibers and cellulose (2:1 ratio by weight), were used to make more than 700 ft^2 of the nano-nonwoven composite. The microfiber dispersion was made separately in a high shear helical mixer. The glass fibers used were 2.4 μm and 5 μm in diameter (3:1 ratio by weight). The lengths of glass fibers were not uniform and varied between L/D ratios of 1000 to 3000. Glass fibers were used because of their low cost. Cellulose fibers were added for additional wet and dry strength that was required for the pilot papermaking machine. Using a similar procedure,

some rolls were made with an addition of polymer fibers, 4 µm nickel fibers and/or activated carbon particles in the glass fiber nano-nonwoven. Fig. IV-14 (b) shows a photograph of the rolls of nano-nonwovens made during scale-up demonstration. Fig. IV-14 (c) shows the nano-porous web of entrapped VGCF within the glass fiber nonwoven rolls.

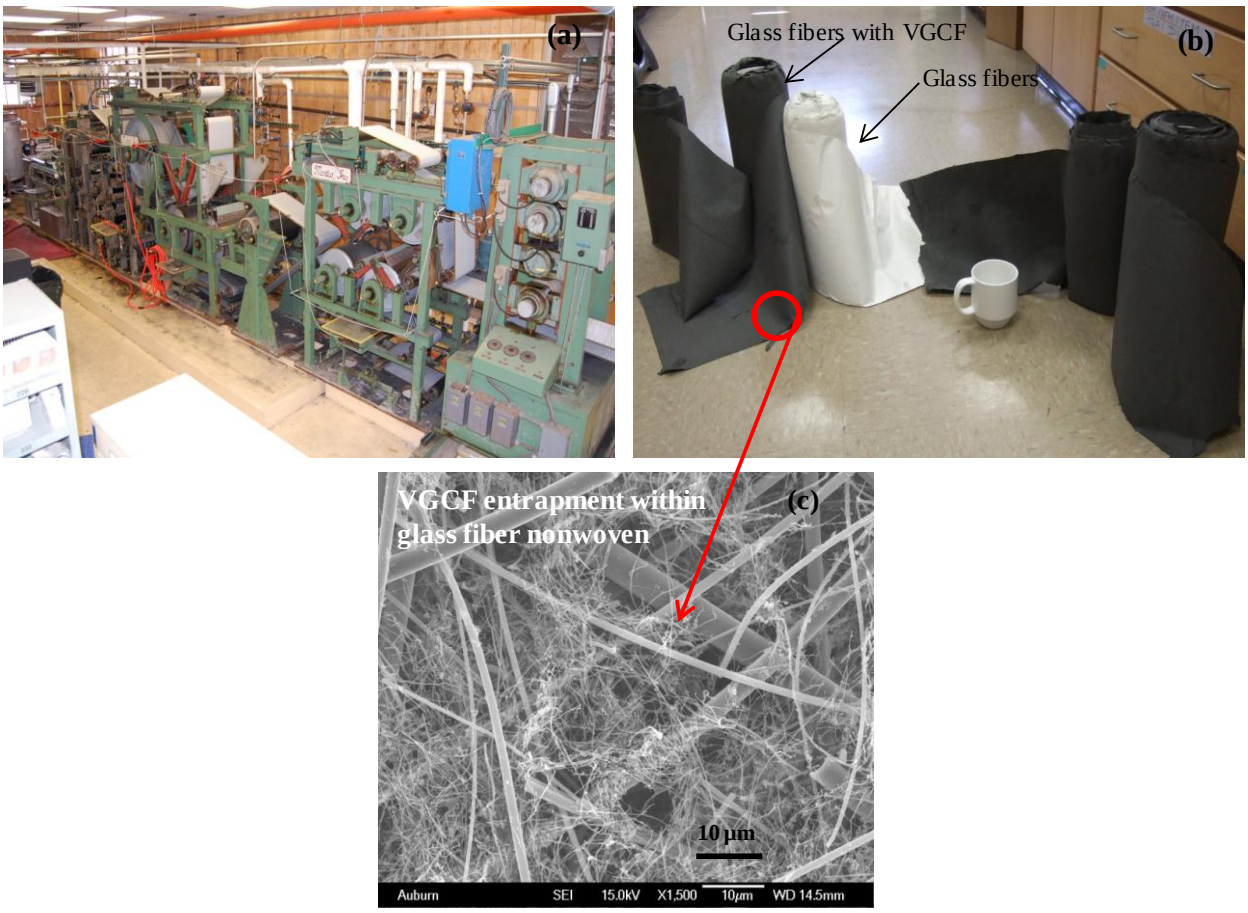

Fig. IV-14. (a) Photograph of Fourdrinier type continuous pilot papermaking machine and (b) photograph of multiple rolls of the nano-nonwovens made during scale-up demonstration, and (c) SEM image of the roll with 2.5% (vol.) VGCF within the glass nonwoven (4% (vol.)).

IV.6 Hypothesis: Effects of 'nano-porous' VGCF flocks on nano-nonwovens

The as-received VGCF are tightly held to each other by strong van der Waals forces and behave as large macro-particles instead of individual nanofibers. These clumped VGCF have a

high packing density of 45.4 kg/m^3. In order to access the 'nano' dimensions of the VGCF, they need to be exfoliated into individual nanofibers by dispersing them in aqueous or solvent based systems. Pluronic-F68 surfactant (1 g/l) solution was used to form an aqueous colloidal suspension of VGCF (1 g/l). These individually dispersed VGCF were flocked using cPAM to form 'nano-porous' web-like structures (Fig. IV-4 (c)). The VGCF flocks are inherently very porous since the nanofibers have point-to-point contacts. The porous structure of the VGCF flocks is indicated by the drastic reduction of the packing density from 45.4 kg/m^3 (as-received VGCF) to ~2.2 kg/m^3 (flocked VGCF).

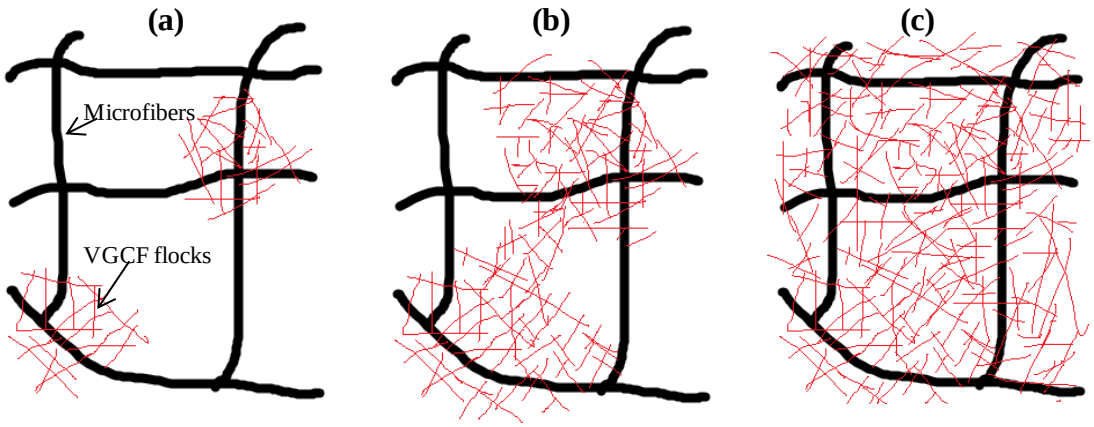

Fig. IV-15. Conceptual view of the effects of variation in VGCF quantity within the nonwoven: (a) low, (b) medium, and (c) high.

The VGCF flocks get entrapped within the 'micro-porous' structure of the nickel nonwoven during wet-lay formation. Fig. IV-15 summarizes our hypothesis predicting the effects of increasing VGCF volume within the nonwovens. Fig. IV-15 is a conceptual view of the pore structures of nano-nonwovens which summarizes the effects of the 3-dimensional interpenetrating interconnecting network of VGCF flocks in a 2-dimensional plane of paper. Fig. IV-15 (a) shows the schematic representation of a low volume of VGCF within the nickel

nonwoven. At a low volume of VGCF, it is hypothesized that the VGCF flocks will give limited enhancement in the filtration performance because micro-pores of the nonwoven provide less resistance to air flow than the nano-pores of VGCF flocks. This limited enhancement in filtration at a low VGCF volume is seen for the sample with 0.75% VGCF in Fig. IV-16 (an outlier from the linear trend). The linear line is the trend of the single fiber filtration efficiency model [IV.29] described by Eq. (IV.4), where 'E' is the fraction filtration efficiency and 'c' is the solid fraction of fiber. Eqs. (IV.4) and (IV.5) are used to decouple the filtration contributions of nickel fibers and VGCF. For the 0.75% VGCF sample, the experimental filtration efficiency for 240 nm aerosol particle was 56%, whereas the single fiber efficiency model gave the value of 75%. This deviation in performance is attributed to the low accessibility to the nano-pores of the VGCF flocks. It should be noted that the filtration efficiency did increase even for 0.75% VGCF, which means that at least some pores of the VGCF flocks were accessible and the flocks did not behave as large solid particles. The porous structure of the VGCF flocks is due to the inherent structure of flocks and could have been increased by the shearing viscous forces of water during wet-lay formation.

$$-\mathrm{Ln}(1-E) \propto \frac{\mathrm{c}}{(1-\mathrm{c})} \tag{IV.4}$$

$$\mathrm{Ln}(1-E)_{VGCF} = \mathrm{Ln}(1-E)_{composite} - \mathrm{Ln}(1-E)_{no\ VGCF} \tag{IV.5}$$

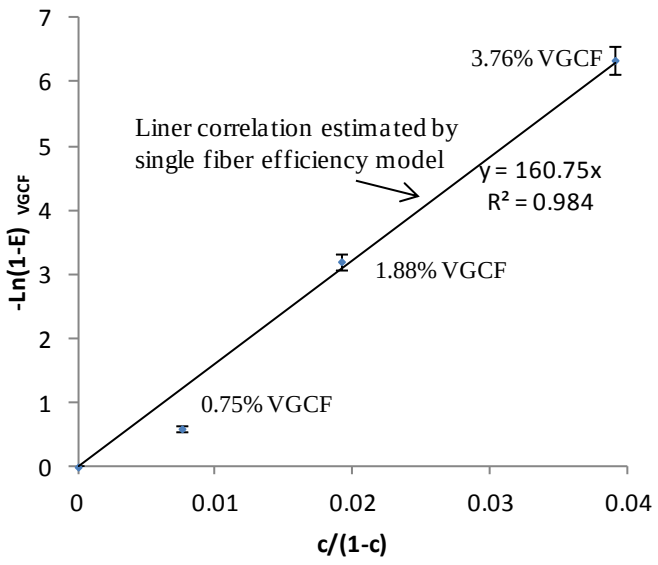

Fig. IV-16. Aerosol filtration efficiency contribution by VGCF varying with VGCF solid fraction plotted as per the single fiber efficiency model for 300 nm aerosol particles.

With an increase in the volume of VGCF, the micro-pores of nonwoven shrink as shown in Fig. IV-15 (b). This decrease in micro-pores may force the air through the VGCF flocks, which increases access to the nano-pores of VGCF flocks. This may lead to an enhancement in filtration, as seen for 1.88% VGCF samples in Fig. IV-9 and Fig. IV-16. Fig. IV-15 (c) shows the high volume of VGCF that closes all the micro-pores, and allows only nano-pores to be left in the structure. The closing of micro-pores lead to a significant increase in pressure drop and a reduction in mean pore diameter, as seen for samples with 3.88% VGCF. This simplistic hypothesis explains all the data, but does not delve into other complications such as the self-healing property of the wet-lay process, which might change the micro-porous structure of nickel nonwoven with the addition of VGCF. The enhancement in filtration efficiency seen in Quality Factor calculations (Fig. IV-10) is attributed to the slip-flow over the nanofibers.

IV.7 Conclusions

This study demonstrates a scalable process to produce a novel nanofiber nonwoven composite (nano-nonwoven) with a uniform 3-dimensional distribution of nanofibers. Commercially available vapor grown carbon nanofibers (VGCF) with a diameter of 150 nm, along with 4 μm (dia.) nickel microfibers and glass microfibers, were used to make these nano-nonwovens via both batch and continuous wet-lay processes. These carbon nanofibers are relatively inexpensive (~$200 per lb) as compared to carbon nanotubes (1-50 nm diameter) that cost $100-1000 per 10 g. As-received VGCF were dispersed in a surfactant solution to exfoliate the VGCF clumps into individual nanofibers. However, these dispersed VGCF were not retained within the microfibrous nonwovens due to their very small dimensions. Flocking of the dispersed VGCF was envisioned as a possibility to retain the 'nano' dimensions of VGCF while creating flocks with sufficiently large dimensions to enable their entrapment within the larger fiber nonwoven matrix (mean pore diameter of ~20 μm for nickel nonwoven) during wet-lay. For successful flocking and entrapment of VGCF, the carboxylic acid groups on the VGCF and the use of a non-ionic surfactant for the VGCF dispersion were found to be important. The VGCF flocks retained the 'nano-porous' structure expected from individual nanofibers. This technique of making nano-nonwovens should be extendable to incorporate multi-walled/single-walled carbon nanotubes.

SEM images show the nano-porous network of the VGCF in the final structure of nano-nonwovens. The mean and bubble point pore diameters decreased with increasing quantity of VGCF. Liquid capillary porometry, polydispersed aerosol filtration and air permeability studies indicated that the VGCF flocks had nano-porous structure, and the flocks did not behave as large macro-particles. Quality Factor ($-\ln(1-E)/\Delta P$) calculations gave the optimal quantity of VGCF

(0.75-1.88% (vol.)) for enhancement in aerosol filtration performance of the 4 μm nickel nano-nonwovens. The reduction-oxidation (redox) characteristics and the double layer capacitance of the nano-nonwovens were measured using cyclic voltammetry. The redox peaks observed in voltammetry confirmed the presence of functional groups on the surface of VGCF. Also, the linear increase in capacitance with the quantity of VGCF showed the electrical connectivity of all the entrapped nanofibers. Scale-up of the process of making nano-nonwovens was demonstrated on a pilot papermaking machine. During the scale-up demonstration, more than 700 ft^2 of the nano-nonwoven composite were made using a continuous Fourdrinier papermaking machine.

IV.8 References

[IV.1] R.S. Barhate, S. Ramakrishna, Nanofibrous filtering media: Filtration problems and solutions from tiny materials, J. Membr. Sci. 296 (2007) 1-8.

[IV.2] K. Kosmider, J. Scott, Polymeric nanofibres exhibit an enhanced air filtration performance, Filtr.+Sep. 39 (2002) 20-22.

[IV.3] T. Grafe, K. Graham, Polymeric nanofibers and nanofiber webs: A new class of nonwovens, Int. Nonwovens J. 12 (2003) 51-55.

[IV.4] K. Graham, M. Ouyang, T. Raether, T. Grafe, B. McDonald, P. Knauf, Polymeric nanofibers in air filtration applications, Adv. Filtr. Sep. Technol. 15 (2002) 500-524.

[IV.5] Q. Zhang, J. Welch, H. Park, C.-Y. Wu, W. Sigmund, J.C.M. Marijnissen, Improvement in nanofiber filtration by multiple thin layers of nanofiber mats, J. Aerosol Sci. 41 (2010) 230-236.

[IV.6] A. Podgorski, A. Balazy, L. Gradon, Application of nanofibers to improve the filtration efficiency of the most penetrating aerosol particles in fibrous filters, Chem. Eng. Sci. 61 (2006) 6804-6815.

[IV.7] F. Dotti, A. Varesano, A. Montarsolo, A. Aluigi, C. Tonin, G. Mazzuchetti, Electrospun porous mats for high efficiency filtration, J. Ind. Text. 37 (2007) 151-162.

[IV.8] A. Kirsh, A. Budyka, V. Kirsh, Filtration of aerosols with fiber materials FP, Russ. J. Gen. Chem. 79 (2009) 2045-2050.

[IV.9] C. Shin, G.G. Chase, D.H. Reneker, Recycled expanded polystyrene nanofibers applied in filter media, Colloid Surface A 262 (2005) 211-215.

[IV.10] M.G. Hajra, K. Mehta, G.G. Chase, Effects of humidity, temperature, and nanofibers on drop coalescence in glass fiber media, Sep. Pur. Tech. 30 (2003) 79-88.

[IV.11] K. Yoon, K. Kim, X. Wang, D. Fang, B.S. Hsiao, B. Chu, High flux ultrafiltration membranes based on electrospun nanofibrous PAN scaffolds and chitosan coating, Polymer 47 (2006) 2434-2441.

[IV.12] W.W. Leung, C. Hung, Investigation on pressure drop evolution of fibrous filter operating in aerodynamic slip regime under continuous loading of sub-micron aerosols, Sep. Pur. Tech. 63 (2008) 691-700.

[IV.13] S.J. Park, D.G. Lee, Performance improvement of micron-sized fibrous metal filters by direct growth of carbon nanotubes, Carbon 44 (2006) 1930-1935.

[IV.14] G. Viswanathan, D.B. Kane, P.J. Lipowicz, High efficiency fine particulate filtration using carbon nanotube coatings, Adv. Mater. 16 (2004) 2045-2049.

[IV.15] ASHRAE 52.2, Method of testing general ventilation air-cleaning devices used for removal efficiency by particle size, American National Standard, Atlanta, GA, U.S.A., 1999.

[IV.16] M.F. Islam, E. Rojas, D.M. Bergey, A.T. Johnson, A.G. Yodh, High Weight Fraction Surfactant Solubilization of Single-Wall Carbon Nanotubes in Water, Nano Lett. 3 (2003) 269-273.

[IV.17] Z. Sun, V. Nicolosi, D. Rickard, S.D. Bergin, D. Aherne, J.N. Coleman, Quantitative Evaluation of Surfactant-stabilized Single-walled Carbon Nanotubes: Dispersion Quality and Its Correlation with Zeta Potential, J. Phys. Chem. C 112 (2008) 10692-10699.

[IV.18] O. Matarredona, H. Rhoads, Z. Li, J.H. Harwell, L. Balzano, D.E. Resasco, Dispersion of Single-Walled Carbon Nanotubes in Aqueous Solutions of the Anionic Surfactant NaDDBS, J. Phys. Chem. B 107 (2003) 13357-13367.

[IV.19] V.C. Moore, M.S. Strano, E.H. Haroz, R.H. Hauge, R.E. Smalley, J. Schmidt, Y. Talmon, Individually Suspended Single-Walled Carbon Nanotubes in Various Surfactants, Nano Lett. 3 (2003) 1379-1382.

[IV.20] K.D. Ausman, R. Piner, O. Lourie, R.S. Ruoff, M. Korobov, Organic Solvent Dispersions of Single-Walled Carbon Nanotubes: Toward Solutions of Pristine Nanotubes, J. Phys. Chem. B 104 (2000) 8911-8915.

[IV.21] S. Giordani, S.D. Bergin, V. Nicolosi, S. Lebedkin, M.M. Kappes, W.J. Blau, J.N. Coleman, Debundling of Single-Walled Nanotubes by Dilution: Observation of Large Populations of Individual Nanotubes in Amide Solvent Dispersions, J. Phys. Chem. B 110 (2006) 15708-15718.

[IV.22] W.E. Scott, Principles of wet end chemistry, TAPPI Press, 1996.

[IV.23] D. Kohler, J. Zabasajja, A. Krishnagopalan, B. Tatarchuk, Metal-Carbon Composite Materials from Fiber Precursors: Preparation of Carbon-Stainless Steel Composite Electrodes, J. Electrochem. Soc. 137 (1990) 136-141.

[IV.24] D. Kohler, J. Zabasajja, A. Krishnagopalan, B. Tatarchuk, Metal-Carbon Composite Materials from Fiber Precursors: II. Electrochemical Characterization of Stainless-Carbon Structures, J. Electrochem. Soc. 137 (1990) 1750-1757.

[IV.25] B.J. Tatarchuk, M.F. Rose, A. Krishnagopalan, J.N. Zabasajja, D.A. Kohler, Mixed fiber composite structures high surface area-high conductivity mixtures, US Patent 5,080,963, 1992.

[IV.26] I.M. Hutten, Handbook of nonwoven filter media, first ed., Butterworth-Heinemann, Oxford, 2007.

[IV.27] V. Gupta, A.K. Jena, Substitution of alcohol in porometers for bubble point determination, Adv. Filtr. Sep. Technol. 13B (1999) 833-844.

[IV.28] A.N. Karwa, B.J. Tatarchuk, Pressure drop and aerosol filtration efficiency of microfibrous entrapped catalyst and sorbent media: Semi-empirical models, Sep. Pur. Tech. (In Press) (2011).

[IV.29] R.C. Brown, Air filtration: an integrated approach to the theory and applications of fibrous filters, Pergamon Press, 1993.

[IV.30] D.A. Kohler, J.N. Zabasajja, A. Krisnagopalan, M.F. Rose, B.J. Tatarchuk, Metal-carbon composite electrodes from fiber precursors: II. Electrochemical characterization of stainless steel -carbon structures, Energy Conversion Engineering Conference, 1989. IECEC-89., Proceedings of the 24th Intersociety, 1989, pp. 1441-1446 vol.1443.

[IV.31] C.-C. Hu, J.-H. Su, T.-C. Wen, Modification of multi-walled carbon nanotubes for electric double-layer capacitors: Tube opening and surface functionalization, J. Phys. Chem. Solids 68 (2007) 2353-2362.

[IV.32] M. Jung, H.-G. Kim, J.-K. Lee, O.-S. Joo, S.-i. Mho, EDLC characteristics of CNTs grown on nanoporous alumina templates, Electrochim. Acta 50 (2004) 857-862.

[IV.33] Y.-T. Kim, T. Mitani, Competitive effect of carbon nanotubes oxidation on aqueous EDLC performance: Balancing hydrophilicity and conductivity, J. Power Sources 158 (2006) 1517-1522.

[IV.34] B. Xu, F. Wu, Y. Su, G. Cao, S. Chen, Z. Zhou, Y. Yang, Competitive effect of KOH activation on the electrochemical performances of carbon nanotubes for EDLC: Balance between porosity and conductivity, Electrochim. Acta 53 (2008) 7730-7735.

[IV.35] E. Frackowiak, F. Béguin, Carbon materials for the electrochemical storage of energy in capacitors, Carbon 39 (2001) 937-950.

[IV.36] E. Frackowiak, K. Metenier, V. Bertagna, F. Beguin, Supercapacitor electrodes from multiwalled carbon nanotubes, Appl. Phys. Lett. 77 (2000) 2421-2423.

Chapter V Pressure drop and aerosol filtration efficiency of microfibrous entrapped catalyst and sorbent media: Semi-empirical models

V.1 Abstract

A three dimensional network of 4-12 μm sintered nickel fibers occupying 2.5-40% (vol.) was used to entrap 5-45% (vol.) aluminum oxide particles with diameters between 90-600 μm. Pressure drop was measured at face velocities of ≤100 cm/s, and filtration efficiency was measured using polydispersed aerosols of potassium chloride particles from 0.09 to 5 μm (dia.). Traditional models for pressure drop and filtration efficiency use mixing rules when combining two components of different diameters. However, these mixing rules gave large errors because of the significant difference between the diameters of the fibers and the entrapped particles. This study describes semi-empirical models for estimating aerosol filtration efficiency and pressure drop, taking into account the heterogeneity created due to the wide diameter variations of the components. An empirical factor accounting for the filtration efficiency due to entrapped particles was added to the single fiber efficiency model by Payet et al. (1992) [V.15]. An empirical correction factor accounting for heterogeneity due to entrapped particles was needed to fit the data to the pressure drop model developed by Harris et al. (2001) [V.4]. The modeled filtration efficiency agreed with the experimental results with errors less than 8% for structures with fiber loading from 2.5% to 12% (vol.) and particle loading from 5% to 45% (vol.). Pressure drop model agreed with the experimental results with errors less than 10% for structures with fiber loading from 2.5% to 40% (vol.) and particle loading from 5% to 45% (vol.).

Nomenclature

a_v surface to volume ratio of a solid shape (m^2/m^3)

c, c_f, c_p total, fiber, and particle solid fraction, respectively (-)

Cr correction factor (-)

D_f, D_s characteristic fiber and particle diameter, respectively (m)

D_{eq} equivalent sphere diameter (=$6/a_v$) (m)

L bed thickness (m)

ΔP pressure drop (Pa)

v face velocity (m/s)

x_i volume fraction of component i (-)

x_{fd} form drag parameter (-)

Greek symbols

τ tortuosity factor (-)

μ viscosity of air (Pa.s)

θ angle of flow path through bed (rad)

$\emptyset$ shape factor (-)

$\eta_{t,}$ total aerosol filtration efficiency (%)

$\eta_{p,}\eta_{f}$ particle and fiber filtration efficiency contribution, respectively (%)

V.2 Introduction

Purifying air by removing both aerosol and molecular contaminants is a requirement for a variety of technologies and applications. Applications such as personal safety masks and fuel cell cathode air filters require the removal of both aerosol particles along with molecular contaminants such as carbon monoxide, sulfur dioxide and nitrogen oxides. Traditionally, these applications employ two segregated systems of filtration: one for aerosol filtration and the other, a catalytic/sorbent system for molecular contaminant removal. For such systems, issues such as pressure drop, volume and weight of the system have to be addressed for high single pass removal efficiency with a minimal energy penalty. Typically, the energy requirement calculated in terms of pressure drop per pass removal of aerosol and chemical contaminant is optimized for applications. For certain specialized applications, both the weight and the volume are also of importance.

In a previous study, the single pass removal efficiency of molecular contaminants was compared for catalysts in three different structures: packed beds, monoliths and microfibrous entrapped catalysts (MFEC) [V.1]. It was found that pleated MFEC systems performed best and had higher removal rates per unit of pressure drop than monoliths or packed beds in terms of heterogeneous contacting efficiency due to the enhanced interphase and intraparticle mass transport rates in MFEC [V.1]. There appears to be an opportunity to simultaneously remove aerosol and molecular contaminants using MFEC because of its fibrous structure and the ability to entrap catalyst/sorbent particles.

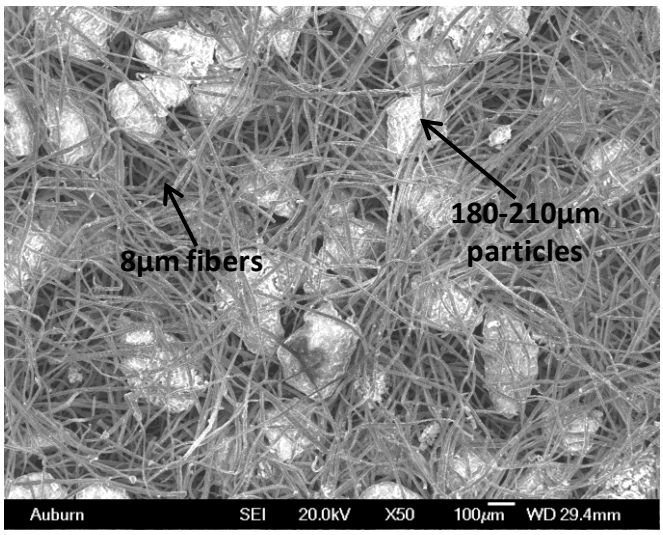

Fig. V-1. SEM image of microfibrous entrapped catalyst (MFEC) with aluminum oxide particles (180-210 µm) entrapped in 8 µm nickel fibers.

A typical sinter locked matrix of a MFEC is shown in Fig. V-1. These materials have good structural stability due to the fibers being thermally bonded (sintered). MFEC is made using a wet-lay process of manufacturing. The properties and materials of MFEC can be varied depending on the requirement of the application. The surface area of MFEC can vary from 1.5 m^2/g to about 1500 m^2/g depending on the fraction of high surface area material [V.2]. MFEC can also be made to have a void volume between 30% and 98% [V.3]. The high void volume of the MFEC facilitates intralayer heat and mass transfer [V.4]. Metal, glass or polymer microfibers can be used to create MFEC structures. The diameter of these microfibers is typically between 1 µm and 25 µm [V.5]. Typically, high surface area catalyst/sorbent particles with diameters between 50 µm and 1000 µm are commonly used. However, support particles with average diameters of 100-200 µm are preferred [V.5]. The advantage of using small catalyst/sorbent particles for chemical filtration is its high heterogeneous contacting efficiency [V.1, 6]. There have been studies for potential uses of MFEC in molecular contaminant removal such as the

catalytic removal of carbon monoxide for fire-escape masks, adsorptive cathode-filters for purifying air for fuel cells and catalytic removal of ozone/VOCs from the cabin air of commercial jets [V.1, 7, 8]. Due to the applicability of MFEC to remove contaminants by particulate filtration as well as chemical adsorption and/or catalyst surface reaction, this study has been conducted to determine the pressure drop penalties and aerosol filtration attributes of this media.

V.3 Experimental

V.3.1 Materials

Ribbon-shaped nickel fibers of metal purity >99% (alloy Ni-200) with nominal diameters of 4 μm, 8 μm and 12 μm and lengths between 3 mm and 6 mm were obtained from Intramicron, Inc. (Auburn, AL). Aluminum oxide pellets (stock # 43832, lot # A29W008) were obtained from Alfa Aesar. These pellets were ground and sieved four times to obtain particles of three sizes: 90-125 μm, 180-210 μm and 500-600 μm. A typical blotter paper made of a mixture of hardwood and softwood cellulose fibers was used. Air and hydrogen (99.9% purity) used in experiments were obtained from Airgas Inc. E-glass fibers of 6 μm diameter and 6 mm length (product # EC6-6-SP) were obtained from Lauscha Fiber International.

V.3.2 Methods

V.3.2.1 Microfibrous entrapped catalysts (MFEC) preparation

Microfibrous entrapped catalysts (MFEC) were prepared using a wet-lay process. For preparing nickel MFEC samples, fibers of nickel and cellulose were dispersed in high viscosity water to create a dispersion of fibers. The viscosity of water was modified by the addition of 0.75% (w/w) water resistant hydroxy ethyl cellulose (HEC) and subsequent hydrolysis of HEC at

~10 pH using sodium hydroxide. After the addition of fibers to the water, the mixture was stirred at low RPM using a blunt propeller to disperse most of the fibers in water. At the last stage of mixing, the dispersion was mixed at a high RPM to disperse the few nickel fibers still in bundles. Using a viscosity modifier for water as well as two-stage mixing ensured that the fibers were dispersed without excessive reduction in their aspect ratio. The dispersion of fibers was used to create a preform of MFEC on 16 cm TAPPI hand-sheet former. During the hand-sheet formation, aluminum oxide particles of different sizes (Fig. V-2) were added to the hand-sheet former. Thus, the preform of MFEC was a three dimensional structure consisting of particles, nickel fibers and cellulose fibers. Cellulose fibers act as temporary binder which imparts wet and dry strength to the preform due to hydrogen bonding between cellulose fibers. The nickel MFEC preform was oxidized (10% oxygen in nitrogen) at 450 ^{o}C to oxidize the cellulose fibers. Subsequently, the preform was sintered at a temperature of 950 ^{o}C for 40 min in 10% hydrogen in nitrogen environment. The nickel fibers sinter to form the nickel MFEC. A similar procedure can be followed to create the E-glass MFEC with or without modifying the viscosity of water.

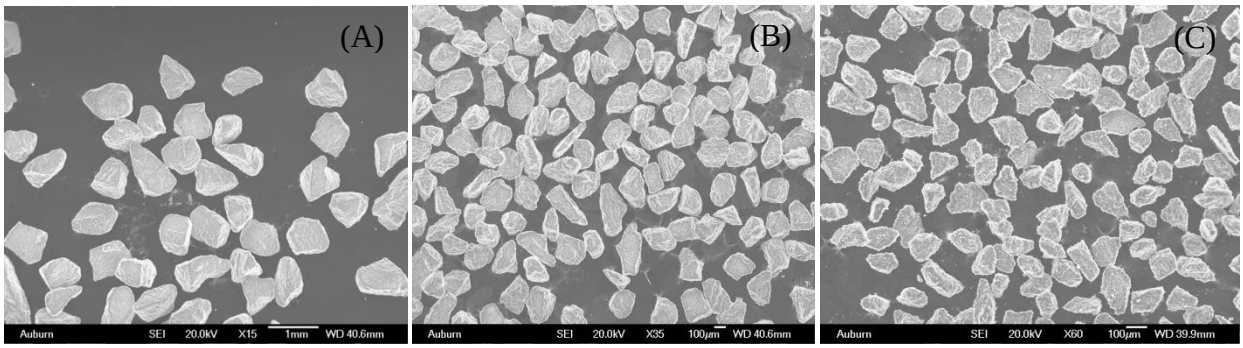

Fig. V-2. SEM images of sieved aluminum oxide particles of size: (A) 500-600 µm, (B) 180-210 µm and (C) 90-125 µm.

Samples of 54 mm diameter were punched out from the MFEC using a steel punch. A hydraulic press was used to compress the samples, which were placed between two 152 mm ×

152 mm × 3.2 mm tight thickness tolerance steel plates with washers used as spacers to define the final thickness of the nickel MFEC. The final thickness of MFEC was measured accurately under a pressure of 1 kPa. The voidage of nickel MFEC can be changed significantly by compression due to the malleable nature of nickel, but E-glass MFEC samples cannot be compressed due to the brittle nature of the E-glass fibers. Aluminum oxide support particles were chosen for entrapment in nickel fibers because of their high crushing strength. High crushing strength ensured that the entrapped particles would not deform or break when MFEC were compressed.

For this study, to discern the effects of different components of MFEC, the MFEC was first made only with different diameter nickel fibers. Subsequently, cellulose fibers were added to nickel fibers to study the effects of cellulose fibers. Finally, particles of various sizes were added to nickel fibers to understand the effects of particles on filtration efficiency and pressure drop.

V.3.2.2 Filtration efficiency and pressure drop characterization

The experimental setup used for filtration efficiency and pressure drop measurements is shown in Fig. V-3. The setup utilized compressed house air that was dehumidified using a silica gel desiccator. After dehumidification, the air was split into two streams used for the nebulizer and for drying the aerosol. The air streams were filtered using inline HEPA filters to remove any background aerosol. The flow to the nebulizer and the drying air was controlled using mass flow controllers. After testing six different nebulizers for consistency of concentration of generated aerosol particles, DeVilbiss nebulizer (product # 4650D-621) was selected. A potassium chloride solution (10% w/w) was used in the nebulizer for particle generation. To neutralize the static charge generated on particles due to aerosol generation, the drying air was passed through a

SIMCO neutralizer (product # AN-6), which ionizes the air to neutralize the static charge. The neutralized potassium chloride particles with a concentration between 140,000 and 180,000 particles (larger than 90 nm in diameter) per 100 cc of air was used as the challenge for testing the filtration efficiency of MFEC. Most of the aerosol stream was vented, and approximately 10% of the aerosol stream was forced through the sample holder using a venturi vacuum pump with an inline mass flow controller to control the face velocity of air through the sample. Two HEPA filters protected the mass flow controller before the Venturi vacuum pump.

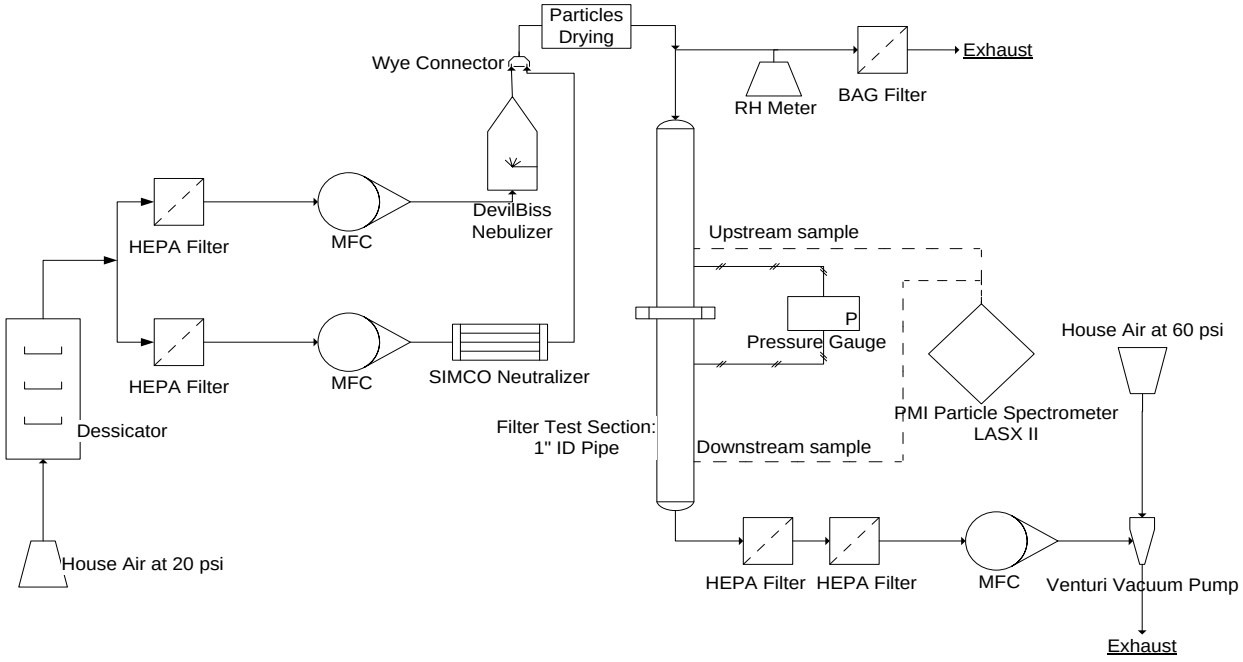

Fig. V-3. Experimental setup for filtration efficiency and pressure drop measurements.

The sample holder was made from a 25.4 mm ID stainless steel pipe and flanges because stainless steel is known to have less particle transport losses than other materials. Flanges with a closed-cell foam gasket were used to form an air-tight seal around the edges of the sample. The upstream and downstream samples were taken at L/D ratio greater than 15 to allow uniform dispersion of particles before sampling by the particle counter. The particle counter used in this

study was a LAS-X II from Particle Measuring Systems (Boulder, Co). The LAS-X II particle counter can count particles from 90 nm to 7500 nm with 100 selectable channel sizes. The sampling of aerosol by the particle counter can be carried out at selectable flow rate between 10-100 cc/min, which makes it ideal for filter media testing at small scale. For all aerosol efficiency tests in this study, the sample size of particle counter was 50 cc/min, which was 1.7% of the total flow through the sample. All filtration efficiency tests were carried out at a face velocity of 10 cm/s. The relative humidity of the aerosol stream was always less than 5%. The humidity level in the aerosol stream is important because potassium chloride droplets form solid particles for relative humidity less than 70% [V.9].

The pressure drop across the MFEC was measured using an Omega (Product # PX154-010DI) pressure transducer. To measure pressure drop using the same experimental setup, a slight modification of the flow streams was required. Only the drying air stream was used with the vent closed and the vacuum stream opened for ambient pressure exhaust after the sample holder. All the filtration tests and analyses were carried out according to the ASHRAE 52.2 standard [V.9] with 7-10 upstream and downstream samples of 1 min. The filtration efficiency data reported in this study has error bars at a 95% confidence interval as per the ASHRAE 52.2 standard.

V.4 Results and Discussion

V.4.1 Nickel fibers

Manufacturing MFEC typically includes using inorganic fibers, cellulose fibers and high surface area particles/fibers. MFEC structures were simplified by studying the effects of one component at a time. To gauge the effect of the diameter of nickel fibers on filtration efficiency

and pressure drop, MFEC were made with only nickel fibers of 4 μm, 8 μm and 12 μm diameters. These simplified structures with only nickel fibers were similar to typical aerosol filter media.

V.4.1.1 Pressure drop of nickel fibers

There are a few popular models used for estimating pressure drop across void structures. The Blake Kozeny equation (viscous loss term in the Ergun equation) [V.10] is the most popular model to describe pressure drop due to viscous losses over a packed bed of particles. The Blake Kozeny equation has been shown to be valid for solid fractions (*c*) of 0.4-0.6 [V.11]. It is also valid until c = 0.8after changing the empirical constant used in the equation [V.11]. The Brinkman equation is popular to describe pressure drop across a fluidized bed. The Brinkman equation is valid for pressure drop across a fluidized/packed bed with c = 0.5 to c < 0.2 [V.11]. The Davies model described in Eq. (V.1) is an empirical model for pressure drop estimation of filter media with an average fiber diameter as observed in microscope. It has been shown to be applicable for c from 0.006 to 0.3 [V.12]. A porous material permeability (PMP) model derived earlier by using a combination of the 'channel flow' model used for Blake Kozeny equation and the 'free particle' Stokes flow model is shown in Eq. (V.2) [V.4]. However, modification to the PMP model was needed due to the lack of a reliable experimental method to measure the flow path angle (θ). The PMP model (Eq. (V.2)) was modified by equating the Blake Kozeny equation to the PMP equation at c = 0.4 to find the constant for the modified PMP model. The modified PMP equation is shown in Eq. (V.3).

$$\frac{\Delta P}{L} = 64\frac{\mu v}{D_f^2}c^{1.5}(1 + 56c^3) \tag{V.1}$$

$$\frac{\Delta P}{L} = 72\frac{\mu v}{(\emptyset D_s)^2}\frac{c^2}{(1-c)^3}\frac{\tau^2}{\cos^2\theta}\left(1 + x_{fd}\right) \tag{V.2}$$

where, $\tau = \left(\frac{2+c}{2}\right)$ and $x_{fd} = \frac{(1-c)^2}{12c}$.

$$\frac{\Delta P}{L} = 97 \frac{\mu v}{(\emptyset D_s)^2} \frac{c^2}{(1-c)^3} \tau^2 \left(1 + x_{fd}\right) \quad \text{(V.3)}$$

The pressure drop across a porous media like MFEC obeys Darcy's law. This means that the pressure drop varies linearly with respect to the face velocity of air as shown in Fig. V-4. Shape factors (ϕ) for all the materials used were determined by the Blake Kozeny equation at high solid fraction using a log-mean particle diameter, as shown in Table V-1. Shape factor [V.11, 13], also known as sphericity [V.14], accounts for the deviation of particle shape from an ideal sphere (ϕ=1 for spherical particles) and it must be obtained empirically for irregular shaped particles [V.11]. It is important to note that metal fibers were used for this study because the metal fiber samples could be compressed to high solid fractions due to their malleable nature. This compressibility of metal fiber samples allowed for the experimental determination of shape factor of fibers using the Blake Kozeny equation. Other fibers such as glass fibers cannot be compressed to such a high solid fraction (c = 0.4) due to their brittle nature.

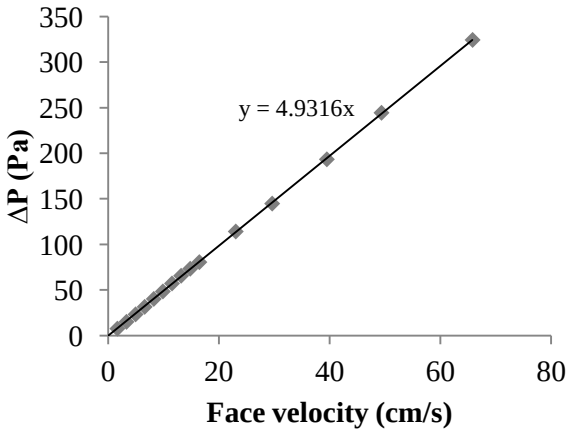

Fig. V-4. Typical pressure drop (ΔP) variation with face velocity for MFEC.

Table V-1. Measured shape factor using Blake Kozeny equation for various components of MFEC.

Particles/Fibers	Shape factor (ϕ)	Solid fraction during measuring 'ϕ'
90-125 µm particles	0.77	0.62
180-210 µm particles	0.80	0.62
500-600 µm particles	0.74	0.62
4 µm fibers	1.09	0.39
8 µm fibers	1.09	0.41
12 µm fibers	1.04	0.40

As shown in Fig. V-5, for MFEC with c from 0.025 to 0.4, the Blake Kozeny equation was not successful in estimating the pressure drop of MFEC for samples with low solidities. Also, the estimations of the Brinkman equation for the fluidized bed did not match the pressure drop data for the rigid structures of MFEC with high voidage. The Davies model fits well for data for $c \leq 0.12$, but it gave errors of more than 15% for $c > 0.12$. However, the modified PMP equation (Eq. (V.3)) fit the pressure drop data well with the least errors for nickel MFEC samples as shown in Table V-2. The RMS error shown in Table V-2 was calculated by Eq. (V.4). Fig. V-6 shows that the modified PMP matched the pressure drop data with a RMS error less than 6% for MFEC made of only fibers of diameters 4 µm, 8 µm and 12 µm. The modified PMP model was used in further modeling of pressure drop across MFEC due to its minimal error in estimation over the range of solid fractions of interest ($0.025 < c < 0.4$). For samples with a mixture of multiple fiber diameters, the average diameter for use in the modified PMP model can be calculated by the equivalent surface to volume ratio as used for Blake Kozeny equation.

$$Error_{RMS}(\%) = \sqrt{\frac{\sum_n \left(\frac{\Delta P_{model} - \Delta P_{experimental}}{\Delta P_{model}} \times 100\right)^2}{n}} \qquad \text{(V.4)}$$

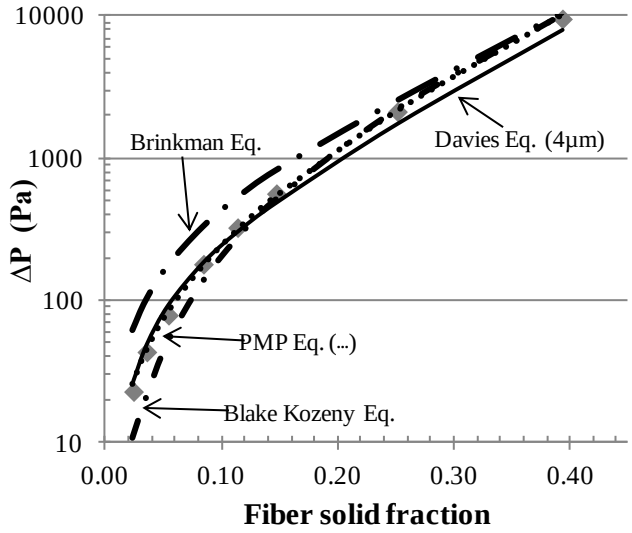

Fig. V-5. Pressure drop (ΔP) variation with fiber solid fraction for MFEC made of 4 μm fibers. (Data reported for face velocity of 10 cm/s and sample thickness of 1 mm.)

Table V-2. Root mean square (RMS) errors of various models for pressure drop data in Fig. V-5.

Model	RMS Error (%)
Blake Kozeny	61
Brinkman (Fluidized bed)	42
Davies (using 4 μm in model)	15
PMP	6

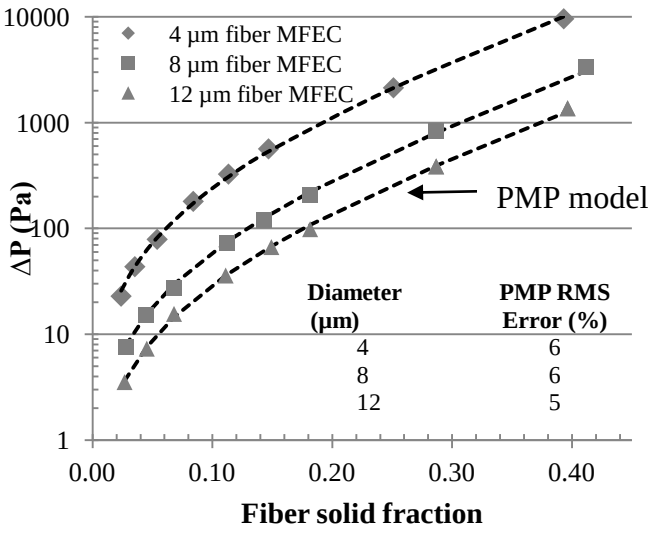

Fig. V-6. Pressure drop (ΔP) variation with fiber solid fraction for MFEC made with 4, 8 and 12 μm fibers. (Data reported for face velocity of 10 cm/s and sample thickness of 1 mm.)

V.4.1.2 Filtration efficiency of nickel fibers

The model derived by Payet et. al. [V.15] is a popular model used for estimating the filtration efficiency of filter media. The Payet model can be used to predict the efficiency of the fibers of MFEC which act as typical filter media in the absence of entrapped aluminum oxide particles. However, the diameter used in pressure drop estimations by the PMP equation is the equivalent sphere diameter, and the diameter used in Payet model is the equivalent fiber diameter. The two are correlated by the surface to volume ratio of sphere and fiber (infinite cylinder) as shown in Eq. (V.5).

$$D_{f,Payet\ model} = \frac{D_{eq}}{1.5} = \frac{\emptyset D_s}{1.5} \qquad \text{(V.5)}$$

After the diameter modification, the Payet model gave good estimates of the filtration efficiency of MFEC with only nickel fibers. A typical fit with the Payet model is shown in Fig. V-7. To make the data of various samples more coherent, a size range of 230-250 nm particle

diameter (240 nm average) was plotted for various other samples. Fig. V-8 shows filtration efficiency of 240 nm particles as a function of fiber solid fraction of various fiber diameters and the estimations by Payet model. As shown in Fig. V-8, the Payet model estimations fit the data with minimal errors up to $c < 0.12$. For $c > 0.12$, the error in estimation by the Payet model was significantly large. However, the typical fiber solid fraction (c_f) in MFEC with entrapped particles is between 0.02 and 0.08. Therefore, for practical purposes, the Payet model is very useful in the estimation of filtration efficiency of fibers in the MFEC structures.

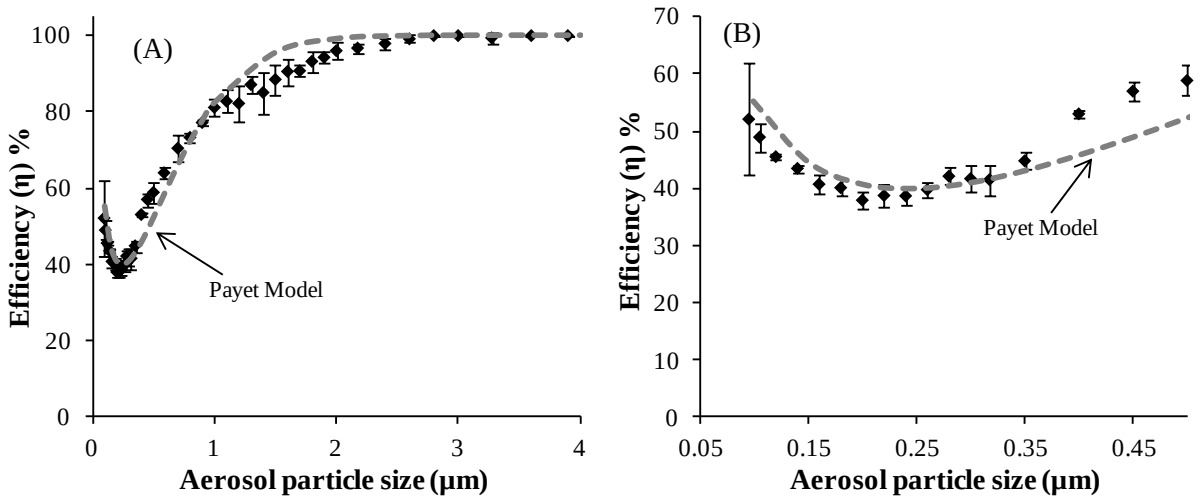

Fig. V-7. Typical filtration efficiency data of MFEC for aerosol particles size range of: (A) 0 to 4 µm and (B) 0.05 to 0.5 µm. (Sample: 4 µm fiber MFEC with 0.035 fiber solid fraction and 1.5 mm thickness. Tested at face velocity of 10 cm/s.)

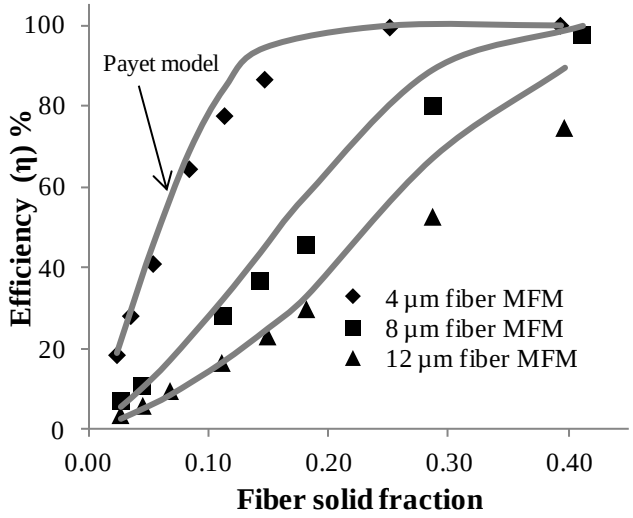

Fig. V-8. Variation of filtration efficiency (for 240 nm particles) with fiber solid fraction for MFEC made with 4, 8 and 12 µm fibers. (Data reported for 1 mm sample thickness. Tested at face velocity of 10 cm/s.)

V.4.2 Nickel fibers with cellulose fibers

Cellulose fibers made of a mixture of hardwood and softwood are used as a temporary binder in MFEC for the structural integrity of the preform after wet-lay formation and before the sintering process. Typically, the cellulose fibers are not a part of the final MFEC. The cellulose fibers have diameters of 10-50 µm and lengths of 1-7 mm [V.16]. These cellulose fibers were oxidized immediately prior to the sintering step. The oxidation of cellulose fibers leaves behind excess voidage in the MFEC structure. The cellulose fiber diameter is significantly larger than the diameter of the nickel fibers (4-12 µm), which may create significant heterogeneity in the structure upon oxidation of cellulose fibers. Experiments were carried out to find out whether the oxidation of cellulose created heterogeneity in the structure which affected the performance of MFEC, or whether the nickel fibers were randomized enough in the structure to have no effect of oxidation of cellulose.

V.4.2.1 Pressure drop and filtration efficiency of nickel fibers with cellulose

Pressure drop and filtration efficiency tests were carried out for sintered MFEC samples with different quantities of cellulose in wet-lay sample preparation. After oxidizing the cellulose fibers and sintering the nickel fibers, gravimetric analysis suggested that there was no cellulose left in the sintered MFEC structure. If cellulose fibers were not completely oxidized after the oxidation step, there would be a surface area contribution by the residual cellulose fibers. This would have shown in the pressure drop data. As shown in Fig. V-9 (A), there was no significant variation in the pressure drop data with different quantities of cellulose, which proved that no residue of cellulose was left in the final MFEC structure. Also, the uniformity of the pressure drop in Fig. V-9 (B) suggests that there was no significant heterogeneity created after oxidizing the cellulose.

The heterogeneity in structure would be more pronounced in the filtration efficiency data because any change in pore size distribution would change the filtration efficiency significantly. However, Fig. V-9 (B) shows that the filtration efficiencies of all the samples remained almost constant which proved that there was no significant heterogeneity created due to addition and oxidation of cellulose in MFEC.

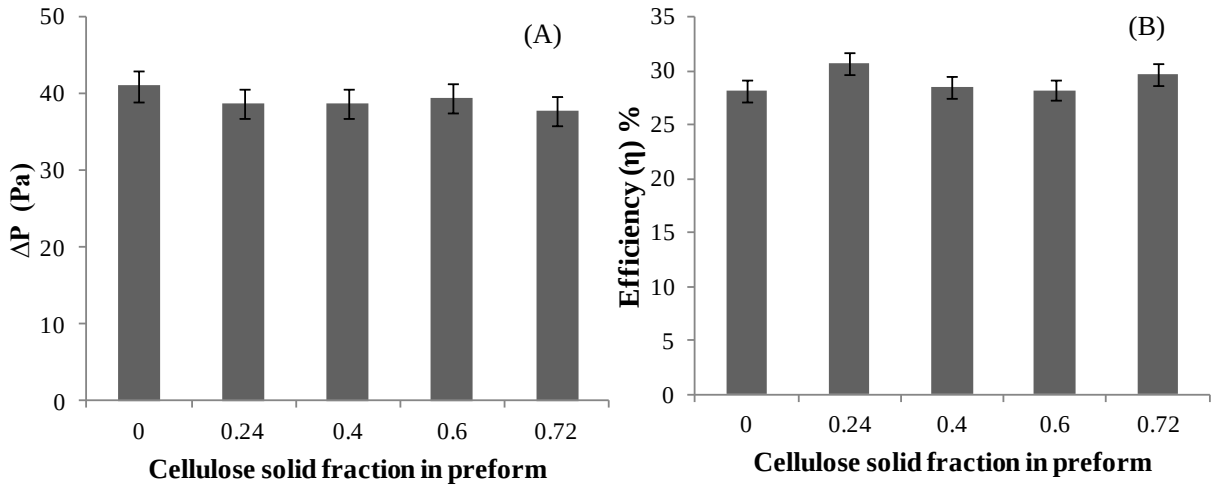

Fig. V-9. Effect of cellulose fibers (temporary binder) in final MFEC: (A) pressure drop (reported for face velocity of 10 cm/s) and (B) filtration efficiency for 240 nm aerosol particles (tested at face velocity of 10 cm/s). (Solid fraction of 4 μm fibers was approximately 0.036 for all samples. Data reported for 1 mm sample thickness.)

V.4.3 Nickel fibers with entrapped particles

A typical final MFEC structure contains inorganic fibers and high surface area particles. MFEC with sintered nickel fibers and entrapped aluminum oxide particles of three average sizes of 107 μm, 195 μm and 550 μm were studied to analyze the effect of particle size on pressure drop and filtration efficiency.

V.4.3.1 Pressure drop of nickel fibers with entrapped particles

Typically, for pressure drop estimation by a model, two components of different diameters are combined by a simple mixing rule of volume weighted average or surface-volume ratio weighted average [V.11, 17]. However, if there is significant difference in the diameter of the two components, the traditional mixing equations lead to large errors in the estimation of pressure drop. Even for packed bed of particles with diameters of ratio 1:5, the Blake Kozeny equation failed to estimate the pressure drop when the smaller particles were less than 30%

[V.18]. For the studied MFEC structures, the diameter ratio of fibers and particles varied from 1:9 to 1:137 with low volume fraction of fibers. For these structures, the pressure drop could not be estimated using the pressure drop equations. The PMP equation [V.4] with modified constant described in Eq. (V.6) overestimated the pressure drop, as shown in Fig. V-10. An empirical correction factor (*Cr*) applied to PMP model as described in Eqs. (V.7 and V.8) reduced the error in estimation to less than 10%. It was experimentally found that *Cr* is a function of solid fraction and diameter of particles and is independent of the fiber diameter as well as the ratio of fiber volume to particle volume. Therefore, the pressure drop of the final MFEC could be estimated by using modified PMP equation and the correction factor (*Cr*).

$$\frac{\Delta P}{L} = 97\mu v \frac{c^2}{(1-c)^3}\tau^2 \left[\left(\sum \frac{x_i}{\emptyset D_s}\right)^2 + x_{fd} \sum \frac{x_i}{(\emptyset D_s)^2}\right] \quad \text{(V.6)}$$

$$Cr = \left(1.651c_p^2 - 1.357c_p + 1\right)\left[1 - 0.1c_p\left(\frac{\emptyset D_s}{(\emptyset D_s)_{107\ \mu m\ particles}} - 1\right)\right] \quad \text{(V.7)}$$

$$\left(\frac{\Delta P}{L}\right)_{with\ Cr} = Cr \times \left(\frac{\Delta P}{L}\right)_{PMP\ Model} \quad \text{(V.8)}$$

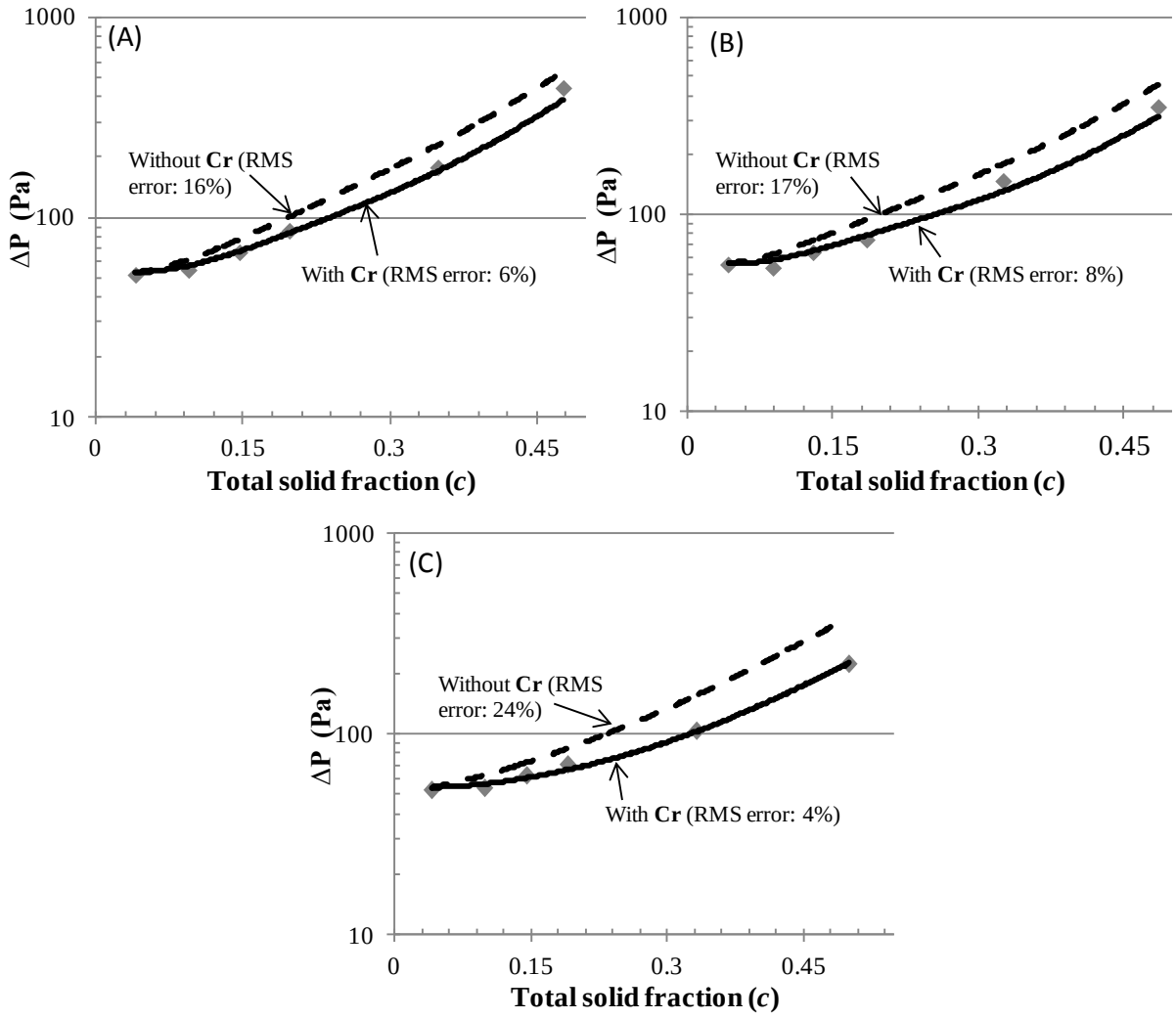

Fig. V-10. Pressure drop variation with total solid fraction of MFEC with entrapped particles of size: (A) 90-125 µm, (B) 180-210 µm and (C) 500-600 µm. (Solid fraction of 4 µm fibers was approximately 0.04 for all samples. Data reported for face velocity of 10 cm/s and sample thickness of 1 mm.)

V.4.3.2 Filtration efficiency of nickel fibers with entrapped particles

In the Payet model, an effective average fiber diameter found by the pressure drop test is used to estimate filtration efficiency [V.15]. However, the efficiency estimations by this approach did not agree with the data. This may be because the Payet model assumes uniformity of the filter media. However, for MFEC structures, there is significant local disparity in the pore

size near the particles when compared to the parts without particles due to the particle's relatively large diameter. Different mixing rules were attempted to fit the data and the model without any success.

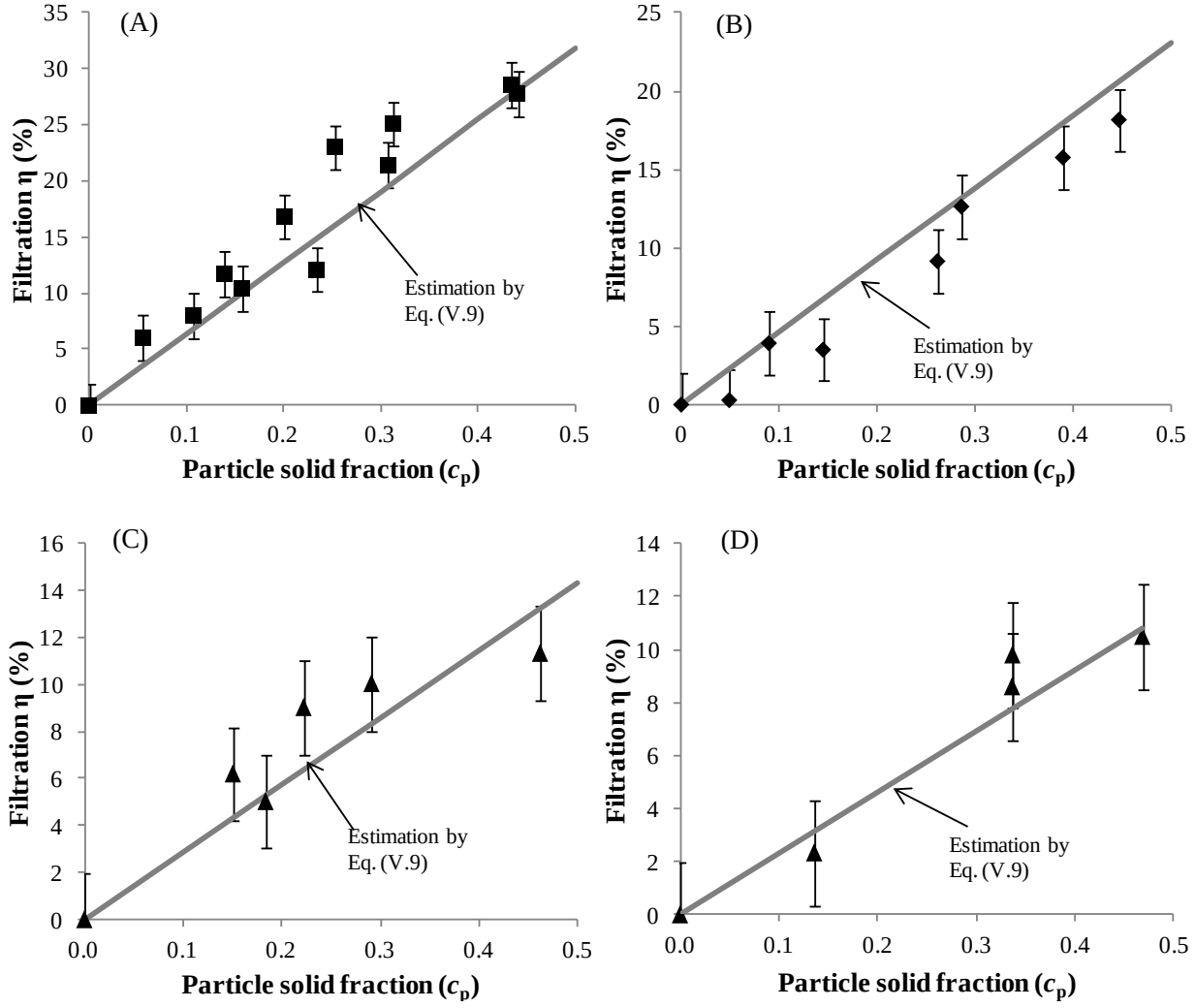

Fig. V-11. Filtration efficiency (for 240 nm particles) contributions (cal.) by entrapped particles: (A) 90-125 µm entrapped in 4 µm fibers, (B) 180-210 µm entrapped in 4 µm fibers, (C) 500-600 µm entrapped in 4 µm fibers and (D) 180-210 µm entrapped in 8 µm fibers. (Data reported for 1 mm sample thickness. Tested at face velocity of 10 cm/s.)

In absence of the applicability of mixing rules, an empirical approach was sought to describe the filtration efficiency of MFEC with particles. However, it was not possible to pack particles so that $c_p < 0.5$. The estimations from the Payet model for the efficiency contribution of fibers were subtracted from the data for MFEC with nickel fibers and particles in order to understand the filtration efficiency contribution due to the particles solid fraction in the range of $0.4 < c_p < 0.05$. During this analysis, the face velocity parameter of the model was changed to compensate for the change in the interstitial velocity in the filter due to the addition of particles in the matrix. This analysis gave a linear dependence of efficiency contributions with the particle solid fraction as shown in Fig. V-11. The efficiency contributions due to the particle solid fraction for a 1 mm thick sample can be described by Eq. (V.9). For samples which have a total estimated efficiency more than 70% for 240 nm aerosol particles (Eq. (V.10)), the efficiency estimation can be done for thickness which gives efficiency less than 70% and then extrapolated to higher thickness using Payet model. This modification to the model has to be done to take into account the non-linear part of the efficiency curve at higher solid fractions as seen in Fig. V-8 for MFEC with 4 μm fibers at $c > 0.12$. In this manner, Eq. (V.10) can estimate the total filtration efficiency of MFEC for 240 nm aerosol particle combining efficiency contributions of the Payet model for fibers and Eq. (V.9) for entrapped particles. The entire filtration efficiency curve can be generated by changing the diameter parameter in the Payet model to match the efficiency for 240 nm aerosol particle where the solid fraction parameter of the model is kept at the solid fraction of fibers.

$$\eta_{p\ at\ 240\ nm} = \frac{2.5\times10^{-6} c_p}{(\emptyset D_s)_{fibers} \times \sqrt{(\emptyset D_s)_{particles}}} \tag{V.9}$$

$$\eta_{t\ at\ 240\ nm} = \eta_{f\ at\ 240\ nm} + \eta_{p\ at\ 240\ nm} \tag{V.10}$$

V.4.4 Experimental verification of the models

The model was verified for many samples with varying particle sizes and diameter of fibers. Fig. V-12 shows the pressure drop and filtration efficiency estimations by models and their good agreement to raw data for sample with particles of two different sizes (107 µm and 195 µm) entrapped in 4 µm fibers. Also, sintered E-glass fibers with an average diameter of 6 µm were chosen to determine whether the shape factor changes with a change in the shape of fibers. For a perfect cylindrical fiber, the shape factor calculated from the pressure drop data should be 1.5. E-glass fibers are manufactured at high temperatures that tend to make the fibers circular in cross section. The shape factor observed for the sintered E-glass fibers was 1.35 as they are more cylindrical than the ribbon shaped nickel fibers (ϕ = ~1.09). The difference between the ideal shape factor and that observed for sintered E-glass fibers may be due to the non-ideal nature of a real filter media sample.

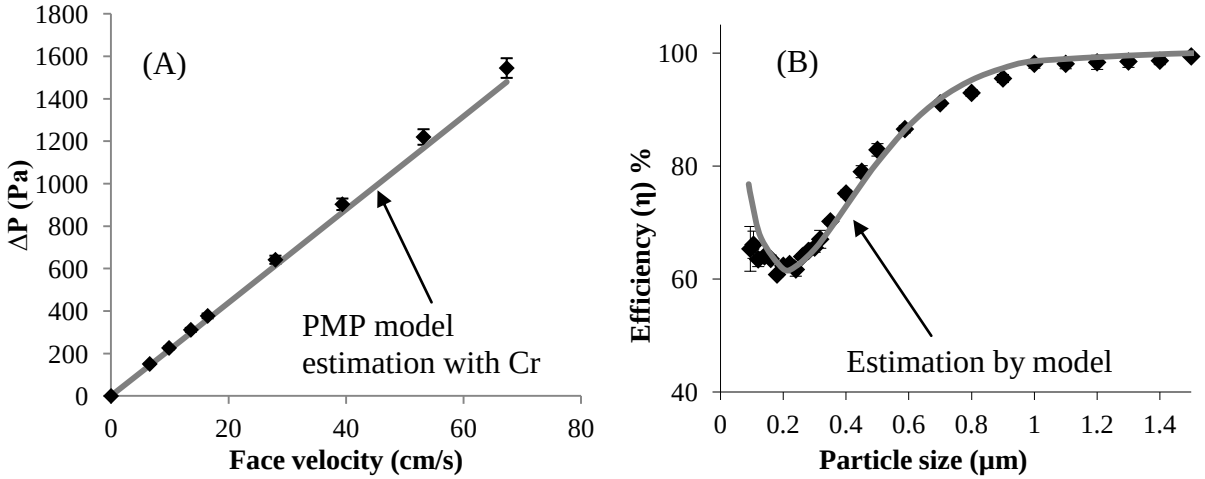

Fig. V-12. MFEC with 90-125 µm particles (solid fraction of 0.16) and 180-210 µm particles (solid fraction of 0.16) entrapped in 4 µm fibers (fibers solid fraction of 0.043): (A) pressure drop characteristics and (B) filtration efficiency characteristics (tested at 10 cm/s). (Sample thickness: 1.23 mm.)

It can be deduced from experimental data that the addition of entrapped particles does not significantly increase the filtration efficiency because of the low external surface area of the particles as compared to fibers. However, the pressure drop increases significantly due to the increase in interstitial velocity within the media with entrapped particles. Therefore, there exists a trade-off between the removal of molecular contaminants and an increase in the pressure drop penalty by MFEC structures. Comparing per pass molecular contaminant removal efficiencies per unit pressure drop, MFEC were found to be more efficient than packed beds [V.1]. Therefore, MFEC can be tailored for molecular and aerosol contaminant removal, and pressure drop penalty for specific applications. Also, models derived here for aerosol filtration efficiencies and pressure drop of MFEC can be combined with the model for filter media pleating of full scale filters [V.19, 20] to give a model for designing full scale macroscopic MFEC filtration systems from the microscopic scale fibers and particles.

V.5 Conclusion

Combinations of empirical and theoretical models were used to estimate the pressure drop and filtration efficiency of three dimensional structures containing micron size fibers and catalyst/sorbent particles. These structures, known as microfibrous entrapped catalysts (MFEC), have potential applications in simultaneous aerosol and molecular contaminant removal. A well established Payet model for filtration efficiency was used to estimate efficiency contributions from fibers and an empirical model was formulated for efficiency contributions from particles. An existing porous material permeability (PMP) model was modified and used for estimating pressure drop across low solidity/high voidage materials. An empirical correction factor (*Cr*) was needed in the modified PMP model to take into account the heterogeneity created due to the addition of large diameter particles in the matrix of sintered fibers. It was observed that cellulose

fibers, which are used as temporary binder in the preparation of MFEC, did not change the flow characteristics within the final MFEC structure. This study has resulted in a powerful tool for estimating pressure drop and aerosol filtration efficiency of MFEC media. The developed models can be extended to design practical chemical and aerosol filtration systems with inclusions for MFEC media pleating for additional area of the media and system packaging.

V.6 References

[V.1] R.R. Kalluri, D.R. Cahela, B.J. Tatarchuk, Comparative heterogeneous contacting efficiency in fixed bed reactors: Opportunities for new microstructured systems, Appl. Catal. B: Env. 90 (2009) 507-515.

[V.2] B.J. Tatarchuk, M.F. Rose, A. Krishnagopalan, J.N. Zabasajja, D.A. Kohler, Mixed fiber composite structures high surface area-high conductivity mixtures, US Patent 5080963, 1992.

[V.3] C.J. Marrion, D.R. Cahela, S. Ahn, B.J. Tatarchuk, Composite fiber structures for catalysts and electrodes, J. Power Sources 47 (1994) 297-302.

[V.4] D.K. Harris, D.R. Cahela, B.J. Tatarchuk, Wet layup and sintering of metal-containing microfibrous composites for chemical processing opportunities, Compos. Part A: Appl. Sci. Manuf. 32 (2001) 1117-1126.

[V.5] L.L. Murrell, F.M. Dautzenberg, R.A. Overbeek, B.J. Tatarchuk, Reactor including a mesh structure for supporting catalytic particles, EP Patent 1001844, 2000.

[V.6] R.R. Kalluri, D.R. Cahela, B.J. Tatarchuk, Microfibrous entrapped small particle adsorbents for high efficiency heterogeneous contacting, Sep. Purif. Technol. 62 (2008) 304-316.

[V.7] S.S. Punde, B.J. Tatarchuk, Ambient temperature carbon monoxide oxidation using microfibrous entrapped catalysts, AIChE Annual Meeting, Salt Lake City, UT 2007.

[V.8] D.M. Kennedy, D.R. Cahela, W.H. Zhu, K.C. Westrom, R.M. Nelms, B.J. Tatarchuk, Fuel cell cathode air filters: Methodologies for design and optimization, J. Power Sources 168 (2007) 391-399.

[V.9] ASHRAE 52.2, Method of testing general ventilation air-cleaning devices used for removal efficiency by particle size, American National Standard, Atlanta, GA, U.S.A., 1999.

[V.10] R.B. Bird, W.E. Stewart, E.N. Lightfoot, Transport phenomena, J. Wiley, 2007.

[V.11] P.C. Carman, Flow of gases through porous media, Butterworths Scientific Publications, 1956.

[V.12] C.N. Davies, Air filtration, Academic Press, 1973.

[V.13] R.H. Perry, D.W. Green, Perry's chemical engineers' handbook, McGraw-Hill, 2008.

[V.14] W.L. McCabe, J.C. Smith, P. Harriott, Unit operations of chemical engineering, McGraw-Hill, 2005.

[V.15] S. Payet, D. Boulaud, G. Madelaine, A. Renoux, Penetration and pressure drop of a HEPA filter during loading with submicron liquid particles, J. Aerosol Sci. 23 (1992) 723-735.

[V.16] W.E. Scott, Principles of wet end chemistry, TAPPI Press, 1996.

[V.17] R.C. Brown, Air filtration: an integrated approach to the theory and applications of fibrous filters, Pergamon Press, 1993.

[V.18] P.C. Carman, Fluid flow through granular beds, Trans. Inst. Chem. Eng. 15 (1937) 150.

[V.19] R.A. Sothen, B.J. Tatarchuk, A semi-empirical pressure drop model: Part I--Pleated Filters, HVAC&R Res. 14 (2008) 841-860.

[V.20] R.A. Sothen, B.J. Tatarchuk, A semi-empirical pressure drop model: Part II--Multi-Element Pleated Filter Banks, HVAC&R Res. 15 (2009) 269-286.

Chapter VI Conclusion and Future Work

VI.1 Conclusion

The studies in this dissertation demonstrate, for the first time, the use of nanofibers within nonwovens for depth filtration to enhance the aerosol filtration performance. Two novel nanofiber-micron fiber composite materials were developed with the intended application in aerosol filtration. Uniform 3-dimensional distribution of carbon nanofibers (CNF) within the micron fiber matrices was successfully achieved in order to use the nanofibers for depth filtration rather than surface filtration. The two routes taken for 3-dimensional incorporation CNF within filter media were: (a) growth of CNF within sintered metal fiber filters, and (b) wet-laid entrapment of pre-manufactured CNF within the filter media. Scalability of the wet-laid method of incorporating CNF within the filter media was demonstrated using a continuous Fourdrinier pilot papermaking machine to manufacture more than 700 ft^2 of the composite. The knowledge of wet-lay entrapment of CNF can be extended to entrap any kind of nanofibers that can have a surface charge when dispersed in water. Few examples of such nanofibers are carbon nanotubes, cellulose nanofibers and ceramic nanofibers. The incorporation of CNF within the filter media resulted in a significant enhancement of its aerosol filtration performance.

A class of 3-dimensional molecular filters known as microfibrous entrapped catalysts (MFEC) is made by entrapping sorbent/catalyst particles within the filter media matrices. The sorbent/catalyst particles remove the molecular contaminants and the fibers have the potential to remove aerosol particles. Semi-empirical models were developed for estimating the pressure

drop and aerosol filtration efficiency performance of these materials. This study has resulted in a powerful tool that can be used for predicting the pressure drop and filtration efficiency performance of practical full-scale MFEC systems, after inclusions for media pleating and packaging.

VI.2 Future Work

1. Non-linear pressure drop across filter media at high face velocities

   At low face velocities, the pressure drop across the filter media varies linearly with the face velocity of air. This linear variation is a result of viscous drag losses. However, at high face velocities, the pressure drop across filter media has polynomial or 3^{rd} order dependence with the face velocity. These higher order losses significantly increase the pressure drop (and energy consumption); however, they can be avoided by good filter designs with high area of filter media. At high face velocities, the inertial drag losses and the compression of filter media result in deviation from the linear profile of pressure drop (versus face velocity). A study to decouple the effects of media compression and inertial losses (at high face velocities) can provide a good insight to understand and improve the designing of filters for high face velocity applications. This study can be applied to microfibrous entrapped catalysts (MFEC) materials for applications at high face velocities.

2. Fiber reinforced plastic

   The wet-lay method of incorporating carbon nanofibers (CNF) can produce fibrous matrices which can be used as substrates for fiber reinforced plastic. Polymers can be infused within the wet-laid media to form polymer-carbon nanofiber-glass fiber

composites which can have better mechanical properties because of the high strength of carbon nanofibers.

3. Filter ageing - dirt loading on 3-dimensional filter media

   The three novel filter media described in this dissertation are all depth filter media. Loading these depth filter media with sub-micron aerosol particles at various face velocities and studying their effects on filtration efficiency and pressure drop can help in understanding and optimization of parameters for the optimal design of filters for their entire lifetime. Similar studies can be carried out for full scale filters which will help in understanding the effects of filter loading on media pleating and packaging.